

ABSTRACT

Title of Dissertation: DESIGN OF A DIELECTROPHORETIC CELL
LOADING DEVICE

Mario Gustavo Urdaneta, Doctor of Philosophy,
2007

Directed By: Professor Elisabeth Smela
Mechanical Engineering Department

In recent years there has been an increasing interest in studying individual cells, and structures that physically entrap one or few cells have been developed for this purpose, but the approaches to load cells into these structures leave a lot to be desired. This dissertation discusses the design of a device that loads cells suspended in a solution into microvials using a combination of dielectrophoresis and fluid flow, which offers significant advantages over previous loading approaches. The basic concept is to use fluid flow and dielectrophoretic forces to position a given cell above a given vial, within an array of similar vials, and then bringing the cell into the vial. The loading of several cells flowing in a channel into a vial in a matter of seconds is demonstrated.

The design of the loading device spurred the development of novel topics in the area of dielectrophoresis. The structures into which cells are loaded produce "parasitic cages". The effect of multiple electric fields and at multiple frequencies had to be explored to eliminate the parasitic cages, and new theory was developed to describe the phenomenon in a straight forward and convenient way. The design process of dielectrophoretic structures known as flow-through sorters was simplified significantly using a method that relies on non-dimensional analysis and a figure-of-merit. These topics investigated have broader applications than just loading cells into vials.

The dissertation demonstrates technologies and design and fabrication methods key to the cell loading design. The dissertation ends by describing the design of a device that can be implemented to load cells into vials on integrated circuit chips and outlining this device's expected characteristics and performance based on the theory and methods presented through the dissertation.

DESIGN OF A DIELECTROPHORETIC CELL LOADING DEVICE

By

Mario Gustavo Urdaneta

Dissertation submitted to the Faculty of the Graduate School of the
University of Maryland, College Park, in partial fulfillment
of the requirements for the degree of
Doctor in Philosophy
2007

Advisory Committee:

Professor Elisabeth Smela, Chair
Professor Benjamin Shapiro
Professor Hugh Bruck
Professor Avis Cohen
Professor Donald DeVoe
Professor Bongtae Han

© Copyright by
Mario Gustavo Urdaneta
2007

Dedication

I dedicate this dissertation to my family. To those that are still living, like Gustavo (son and father), to those that are dead, like Hugo, Pedro, and Zaida, to those that are new, like Sarah, and to those that have been around for a while, like Maria Carmen.

Acknowledgements

First I must acknowledge my teachers and mentors. This is truly long list, that begins with Maestra Ana Perez, who taught me how to read and write, and it includes all those people who patiently answered most of my incessant stream of questions. At the University of Maryland my teachers included Professor Elisabeth Smela, who most notably taught me how to write (again), and Tom Laughran who taught me how not to be afraid of breaking equipment while *not* breaking equipment. If I can ever reach high it will be only because I am standing on all of their shoulders, on the shoulders of giants.

I also should acknowledge my peers, who helped me climb on the shoulders of these giants. Recently, they include Dr. Xuezheng Wang, who reviewed my writing mercilessly, Marc Dandin, who reviewed my writing patiently, and Sarah Urdaneta, who reviewed my writing lovingly.

Finally I would like to acknowledge the Laboratory of Physical Sciences for its financial support.

Table of Contents

DESIGN OF A DIELECTROPHORETIC CELL LOADING DEVICE	ii
Dedication	ii
Acknowledgements	iii
Table of Contents	iv
List of Tables	vi
List of Figures	vii
Chapter 1 Introduction	1
1.1 Single Cell Studies	3
1.2 Cell Loading Requirements	5
1.3 Single Cell Manipulation Methods	5
1.3.1 Surface Chemistry	7
1.3.2 Grippers	7
1.3.3 Hydrodynamic Traps	8
1.3.4 Gel Traps	9
1.3.5 Optical Tweezers	9
1.3.6 Acoustic Wave Traps	10
1.3.7 Dielectrophoresis	11
1.4 The Dielectrophoretic Effect	11
1.5 Chronological Overview of Dielectrophoresis	18
1.5.1 The Past	19
1.5.2 The Present	21
1.5.3 The Future	22
1.6 Cell Loading Method Overview	28
1.7 Device Materials and Fabrication Methods	29
1.8 Cell Loading Challenges	33
1.9 Organization of Dissertation	37
Chapter 2 Design of Dielectrophoretic Flow-Through Sorters Using a Figure of Merit..	40
2.1 Abstract	40
2.2 Introduction	40
2.3 Methods	45
2.3.1 DEP vs. Drag Forces	45
2.3.2 Non-Dimensionalization	49
2.3.3 Numerical Solution of Model Configurations	51
2.3.4 Figure of Merit U'_{\max}	55
2.4 Results and Discussion	57
2.4.1 Dependence of Sorter Performance on Configuration and Geometry	57
2.4.2 Model Validation	59
2.4.3 Discussion	62
2.5 Conclusions	64
Chapter 3 Multiple Frequency Dielectrophoresis	66
3.1 Abstract	66
3.2 Introduction	67
3.3 Modeling	71

3.3.1	Dielectrophoretic Force at Multiple Frequencies	72
3.3.2	CM_{eff} for Yeast Cells	74
3.3.3	Particle Separation	79
3.3.4	Predicted Cell Positions	83
3.4	Experimental Work	84
3.4.1	Materials and Methods	84
3.4.2	Results: Single Frequency on One Type of Particle (Control Experiment) 87	
3.4.3	Results: Multiple Frequencies on One Type of Particle	89
3.4.4	Results: Multiple Frequencies on Two Types of Particles	91
3.5	Discussion	93
3.6	Concluding Remarks	98
3.7	Appendix	99
Chapter 4	Dielectrophoretic Vial Traps to Load Cell into Vials	102
4.1	Abstract	102
4.2	Introduction	102
4.3	Background	104
4.3.1	Cell Clinics	104
4.3.2	Cell Loading	105
4.4	Results	108
4.4.1	MFDEP Vial-Loading Design	108
4.4.2	Floor-Ground Configuration	110
4.4.3	Ceiling-Ground Configuration	113
4.4.4	Trap Cancellation + Focusing	116
4.5	Conclusions	117
4.6	Methods	118
4.6.1	Numerical Models	118
4.6.2	Device Fabrication	119
4.6.3	DEP Experimental Procedures	122
Chapter 5	Cell Loading Device	124
5.1	Cell Loading Device Prototype	124
5.2	Design of Cell Loading Device for the Cell Clinics Chip	129
5.2.1	Cell Clinics Chip Components	131
5.2.2	Dielectrophoretic components	138
5.2.3	Summary of the Cell Loading device	153
Chapter 6	Conclusions	155
Appendix A.	Challenges on Patterning Photoresist on and Around the Vials	159
Appendix B.	Cell Clinics Technology Platform for Cell-Based Sensing	165
Appendix C.	Flow-Through Sorter Modeling Consideration	171
References	187

List of Tables

Table 1-1. Comparison of different technologies for cell manipulation.....	6
Table 2-1. Parameters used to non-dimensionalize the variables in Equation (11) (an apostrophe indicates a non-dimensional variable).....	50
Table 3-1. Parameters used to predict the Clausius-Mossotti factors CM of viable and non-viable yeast cells. Parameters taken from [83] or measured (*).....	75
Table 5-1. Physical specifications of the cell loading device design presented	153

List of Figures

Figure 1-1. A) The chip consists of an array of lidded microvials which can be independently controlled by an integrated circuit that serves as its substrate. B) A Picture of a cell clinics microvial (courtesy of M. Christorphersen). C) Cells will be cultivated inside the microvials and monitored through integrated circuit sensors inside the vial. 2

Figure 1-2. The charges of a particle are separated by an electric field. If the electric field is uniform, no net force is exerted because the electrostatic forces on the dipole (charge times electric field) balance. 13

Figure 1-3. If the electric field is not uniform, the forces on the dipole due to the electric field are not balanced, and a net force is exerted. 14

Figure 1-4. Number of dielectrophoresis-related journal publications published per decade (logarithmic scale). The number of publications was obtained from my personal library and from searching the keywords “dielectrophoresis” and “dielectrophoretic” in ISI Web of Knowledge. The dashed line shows the trend that would be expected based on the average journal article publication growth rate observed in the USA [53]. 19

Figure 1-5. Schematic of dreamed nanometer-scale integrated circuit. The substrate and nanoparticles of different properties, sizes, and shapes provide functionality. To make it using dielectrophoresis it would be necessary to distort the electric fields at scales of < 5 nm. 26

Figure 1-6. Schematic of the cell loading method presented..... 29

Figure 1-7. The current configuration of the cell clinics chip uses a DIP40 and a custom polymer package around the wirebonds. 36

Figure 2-1. Illustration of a representative flow-through DEP sorter [48]. The electrode pair consists of one electrode on the floor of the channel and one on the ceiling. A) With the DEP force off, particles flow out of outlet 1, carried by the flow. B) When the electrodes are activated, negative DEP forces change the trajectories of the selected particles, causing them to flow to outlet 2. 42

Figure 2-2. The forces acting on one of the particles in Figure 2-1. The particle moves with the fluid until it approaches the electrodes. Just upstream of the electrode, the DEP force projection on the (x',y') plane is perpendicular to the electrode edges. This causes the particle to slow down in the streamwise direction (x' -direction) and acquire a velocity component perpendicular to the channel walls (y' -direction). 46

Figure 2-3. A-D) Side view illustration showing how w' defines the geometry of configurations A-D ( channel wall,  electrode). The magnitude of U'_x at each point is given by the gray-scale intensity, with lighter shades indicating higher forces. The dashed white lines show the height z' of lowest U'_x , and the arrows point to the location of U'_{max} . E) 3D plot of U'_x for configuration C. F) View looking straight down the channel, as indicated by the cone in E. This view shows, as a function of z' , the highest values of U'_x along the channel, the lowest of which is U'_{max} . The larger this number, the higher the flow speeds that can be handled by the sorter..... 53

Figure 2-4. The non-dimensional figure of merit U'_{max} as a function of w' for electrode

configurations A (■), B (▲), C (●), and D (○)..... 58

Figure 3-1. A) Real part of the Clausius-Mossotti factors for live and dead yeast as a function of frequency, found as described in section 3.3.2. B) Schematic illustration of how the force on a live yeast cell at a given position can change with particle volume (V_1 vs. V_2) electric field strength and gradient (\vec{E}_1 vs. \vec{E}_2)..... 69

Figure 3-2. The CM_{eff} obtained from the two-shell model as a function of frequency for A) live and B) dead yeast that result from superposing onto the x-axis frequency a 5 kHz (solid line) or 5 MHz (dashed line) signal of equal magnitude. The real part of the Clausius-Mossotti factors (thick gray lines) are shown for comparison. The points a , b , and c correspond to areas in Figure 3-5, and the points i and ii are the original and altered cross-over points. 77

Figure 3-3. CM spectra (gray lines) for human T- and B-lymphocytes as a function of frequency, and their CM_{eff} (black lines) when a 10 kHz signal of relative amplitude 0.6 is added to the original frequency. The range for separation is shifted and widened from a to b 81

Figure 3-4. Sign of the product of CM_{eff} s for T- and B- lymphocytes under two frequencies f_1 (x -axis) and f_2 (y -axis) at four amplitudes $|E_2|/|E_1|$. Regions in which the CM_{eff} s are the same are shown in white and regions in which the CM_{eff} s are different (i.e., the frequency ranges in which the particles can be readily separated) are shown in black. 82

Figure 3-5. The effective Clausius-Mossotti factors for live and dead yeast cells between electrodes at 5 kHz, 5 MHz, and ground, obtained by taking into account only the

closest two electrodes.	84
Figure 3-6. Photograph of the 2-frequency device, covered with yeast cells, that was used in the demonstration of simultaneous positive and negative DEP. The area shown in subsequent figures is indicated.....	85
Figure 3-7. A) Killed, methylene blue stained yeast cells under AC fields of 5 MHz (negative DEP). The bottom electrodes were connected together and the top electrode was grounded. This region is a close-up view of Figure 3-6. B) Dead cells under AC fields of 5 kHz (positive DEP). In both A) and B), the voltage was 5.7 V. All images were taken using samples from the same yeast cell solution.	88
Figure 3-8. Dead yeast cells under simultaneous positive and negative DEP caused by exciting one electrode at 5 kHz and another at 5 MHz with the same magnitude of voltage (5.7 V). Compare model predictions in Figure 3-5.....	90
Figure 3-9. Dead yeast cells under simultaneous positive and negative dielectrophoresis caused by electrodes at voltages with different frequency and different amplitude.	91
Figure 3-10. Positive and negative dielectrophoresis acting at the same time on live (clear) and dead (dark) yeast cells.	92
Figure 3-11. Live (clear) and dead (dark) yeast cells selectively patterned in a single step by means of MFDEP. The inner electrode was at 5 kHz, the middle ring electrode was grounded, and the outermost ring electrode was at 5 MHz.	96
Figure 4-1. Side view of numerical simulation results for positive DEP applied inside a vial without parasitic trap cancellation. The ground electrode is on the floor, outside of the vial. A) Particle tracing results. The background gray levels represent velocity contours, with lighter shades showing higher velocities (forces). The flow	

speed above the vial is $60 \mu\text{m/s}$ from right to left. B) Close-up of the region inside the dashed white box in A) showing the electric field contours (logarithmic scale) near the vial walls. The arrows point to regions where the electric fields increase rapidly; these are the regions to which cells are attracted. C) Top view of an SU8 vial with an electrode in the center applying positive DEP in a solution containing non-viable yeast cells. D) Close-up of the vial rim (area shown in the dashed box in C), showing cells in the parasitic trap, instead of inside the vial..... 106

Figure 4-2. Cross-section of vial cage devices with ground electrodes on A) the floor and B) the ceiling..... 109

Figure 4-3. A) Schematic of one of the vial traps in a ceiling-ground configuration. B) Cross-section a-a' of the vial trap showing the positions of the inner, outer, and ground electrodes. C) Working principle of the DEP cell-loading system. The inner electrode attracts cells into the vial, and the outer electrodes actively cancel the parasitic trap at the vial rim. 110

Figure 4-4 . A) Particle tracing simulations of an MFDEP vial trap in a channel $100 \mu\text{m}$ tall with $60 \mu\text{m/s}$ flow speed above the vial, $5 V_{\text{RMS}}$ on the inner electrode, and $3.5 V_{\text{RMS}}$ on the outer electrode. The gray levels represent velocity contours (in log of m/s). B,C) Log scale contours of the electric fields due to the B) pDEP and C) nDEP electrodes, with arrows indicating regions of highest attractive and repulsive force, respectively. D) Experimental results of an MFDEP vial trap in a channel $125 \mu\text{m}$ tall with $50 \mu\text{m/s}$ flow speed above the vial. The inner electrode was held at $5 V_{\text{RMS}}$, and the outer electrode at $3.5 V_{\text{RMS}}$ 112

Figure 4-5. A) Particle tracing simulations of an MFDEP vial trap with the ground electrode on the ceiling in a channel 100 μm tall with 300 $\mu\text{m}/\text{s}$ flow speed above the vial. The inner pDEP electrode was at 7 V_{RMS} , the outer nDEP electrode was at 5 V_{RMS} 115

Figure 4-6. Simulations of vial loading enhanced by nDEP particle focusing. A) Floor-ground vial trap with electrodes excited at 5 (inner), 3.5 (outer), and 9 (focusing) V_{RMS} under 20 $\mu\text{m}/\text{s}$ bulk flow (up to 60 $\mu\text{m}/\text{s}$ above the vial). B) Ceiling-ground vial with electrodes excited at 7 (inner), 5 (outer), and 9 (focusing) V_{RMS} under 100 $\mu\text{m}/\text{s}$ bulk flow (up to 300 $\mu\text{m}/\text{s}$ above the vial)..... 117

Figure 5-1. A) Picture of the prototype of the cell loading device. B) Illustration of its operation. 125

Figure 5-2. Dead yeast cells steered to one of two channels by a pair of sorting electrodes (only one is visible) excited at 5 kHz, 8 V_{RMS} 128

Figure 5-3. Features in the microfluidic network that had the tendency to delaminate. 129

Figure 5-4. Top view A) and side view B) of the recommended cell clinics chip configuration integrated with microfluidics and cell loading capabilities..... 130

Figure 5-5. Illustration of the operation of the cell loading device design to be integrated with the cell clinics. 131

Figure 5-6. Real part of the Clausius-Mossotti versus frequency for PC-12 cells under sinusoidal and square waveforms. Clausius-Mossotti factor calculated using a single-shell model [40] and published cell properties [7]..... 133

Figure 5-7. A)The current configuration of the cell clinics chip uses a DIP40 B) and a

custom polymer package around the wirebonds. C) Cross section schematic of current packaging solution.....	135
Figure 5-8. Packaging scheme under development by M. Dandin. A) Top view, B) partial side view, and C) cross-section detail of pad and back-side connection.....	136
Figure 5-9. Cell clinic vial with its lid closed A) and open B).....	137
Figure 5-10. Real part of the Clausius-Mossotti factor as a function of frequency and solution conductivity for PC-12 cells.	140
Figure 5-11. Particle tracing simulations of a MFDEP vial trap in a channel 250 μm tall (only 200 μm shown) with 100 $\mu\text{m/s}$ bulk flow speed. The inner electrode (at 7 V_{RMS}) is located inside the vial, the outer electrode (at 5 V_{RMS}) on top of the vial and on the outer sidewalls.....	143
Figure 5-12. Dielectrophoretic vial traps fabricated on a bio-amplifier cell clinics chip. A) Overhead view of the unpackaged chip. B) Detail of one of the vial traps.	144
Figure 5-13. A) Experimental set up of the CMOS/MFDEP vial trap chip. B) Yeast cells inside one of the vials.	145
Figure 5-14. U_{max} for the routing section of the loading device as a function of electrode voltage.....	148
Figure 5-15. Particle tracing simulation results of the floor-ground vial trap loading aided by the effect of focusing electrodes.	152
Figure A -1. Side view illustration of the topography on photolithography was done...	159
Figure A -2. A) Illustration and B) photography of 1813 film after spinning at 2000 rpm for 30 seconds.	161

Figure A -3. Photoresist layer after spinning at 5000 rpm for > 1 minute.....	162
Figure A -4. Exposure of 80 mJ/cm ² and 720 mJ/cm ² . The gap between the mask and the substrate, due to the presence of the SU8 structure, and the increased exposure results in degraded pattern transfer from the mask.....	163
Figure A -5. Photoresist near a 50 μm tall SU8 vial after development.....	164
Figure B -1. The cell clinics array microsystem for long term monitoring of cells.	166
Figure B -2. SU8 microvial with a polypyrrole/gold bilayer hinge on a dummy silicon sample. The hinge is shown in the open (V = -1 V vs. Ag/AgCl) and closed (V = 0 V) positions.....	167
Figure B -3. 24-bioamplifier CMOS chip with MEMS structures. The chip has been packaged as described in [162]......	168
Figure B-4. The dielectrophoretic trap used to load individual cells into the microvials.	169
Figure C-1. A) U' as a function of x -position along y' of weakest force. B)Zoom in of the dashed box in (A) (obtained after increased mesh refinement).	174
Figure C-2. Typical mesh used to find U'_{max} (this case is for $w' = 1$). The electrodes, on the floor and ceiling of the channel, are illustrated by the black lines.....	177
Figure C-3. Average difference between U'_{max} obtained from models with i and $(i+1)$ mesh refinements, where i is the number of refinement iterations ($w' = 0.002 - 4$).	178

Chapter 1 Introduction

This dissertation describes a method of loading small numbers of cells into cages using dielectrophoresis and fluid flow. This dissertation focuses on key techniques that need to be developed to be able to load the cells. The aim of this work is to define a method that can eventually be integrated with the cell clinics chip [1-3], and thus certain aspects of the cell clinics chip are considered in the development of the method. The aim of this work excludes integrating the method with the cell clinics chip. The cell clinics chip (Figure 1-1) is a platform for the long term monitoring of groups of 1-10 cells each, which is being developed through a collaboration between the Laboratory of Microtechnologies, headed by Elisabeth Smela, and the Integrated Biomorph Information Systems Laboratory (IBIS), headed by Pamela Abshire, both groups at the University of Maryland at College Park. The cell clinics chip consists of many cell cages, or microvials, fabricated on a complementary metal-oxide-silicon (CMOS) integrated circuit chip that will be used to monitor the activities of cells in the cages. The loading device must be capable of manipulating cells suspended in a solution and loading them inside the cages, without requiring major changes to previously designed aspects of the chip, such as vial and chip geometry and materials. Appendix B presents details on the cell clinics.

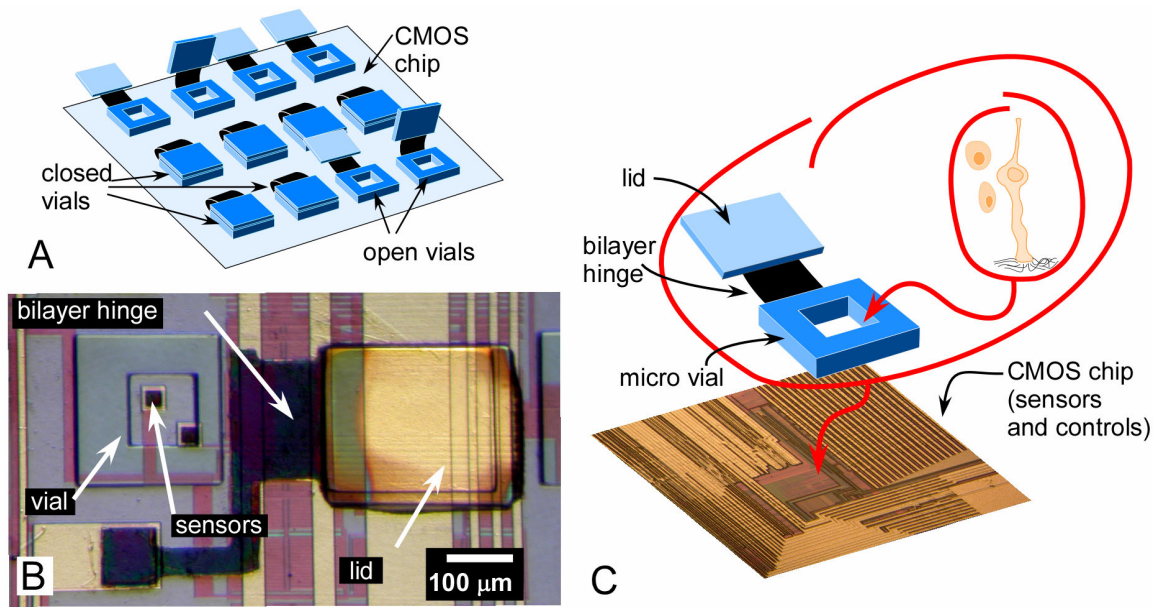


Figure 1-1. A) The chip consists of an array of lidded microvials which can be independently controlled by an integrated circuit that serves as its substrate. B) A Picture of a cell clinics microvial (courtesy of M. Christorphersen). C) Cells will be cultivated inside the microvials and monitored through integrated circuit sensors inside the vial.

Developing a dielectrophoresis-based cell loading device that works in such a complex topography is uncharted territory; it has never been done before. Positioning single cells using dielectrophoresis on substrates without out-of-plane structures (such as the microvials on the cell clinics chip) has been demonstrated [4-8]. However, previous approaches for loading cells into cages do not include dielectrophoresis. Instead, cell loading into cages has been done by hand [9-11], using optical tweezers [12], and suction [13]. Those approaches have integration or loading speed characteristics that make it unfit to be used with the cell clinics chip. In this dissertation I present a novel approach

of cell manipulation using dielectrophoresis that meets all of the requirements of the cell clinics chip.

I will begin by providing the motivation for single cell studies, and reviewing common methods for manipulating cells. I will also discuss the basic principles of dielectrophoresis, and why it is the manipulation method best suited for the cell clinics chip. Finally, I will conclude the introduction by giving a chronological review that includes past, present, and future perspectives on dielectrophoresis and how the work presented in this dissertation fits into that chronology. In this dissertation, each chapter begins with a literature review that frames the work relevant to that chapter; therefore this will not be included in the introduction as it is typically done.

1.1 Single Cell Studies

Lab-on-a-chip devices for long term studies of single cells have been under development for several years [4, 14-17]. This approach has a rising importance in basic biological research and drug development [15, 18, 19]. To understand the relevance of these devices we need to discuss how conventional cell studies are done.

Conventional cell studies measure parameters on a large number of cells or cell extracts, this is called the "blender approach" [14]. Cell activities monitored this way can only reflect average values of their response [20], with the disadvantage of masking cellular heterogeneity [14]. For example, the control of lactose in *e. coli* takes place in an on-off

fashion, but when this activity is measured using the blender approach it appears modulated [14]. Intermediate activity levels that only reflect the relative cell population at either state could be misinterpreted as the activity level of each of the cells [14]. This shortcoming is avoided if cells are studied as individuals, rather than as a colony. Additionally, it is well known that a cell behaves differently depending on whether it is alone or is part of a cell culture [21] because cells signal each other chemically and electrically [21], and so the same conventional study approaches applied to a cell isolated from others give results of limited interest. Therefore, to deepen our understanding of cellular biology we need to monitor many cells within the same culture independently from each other.

One approach taken to monitor many cells independently from each other is to use sensors with similar dimensions as the cells that provide the spatial resolution needed to distinguish between neighboring cells [4, 14-17]. Single cells have been interfaced with such machines for several years [19]. In fact, it was the work of P. Fromherz et al. [10, 11, 22, 23] inspired me to pursue graduate studies on this subject. Machines with cellular-sized sensors arrays have been designed to monitor electrical activity [4, 24], state of substrate adherence [25], and chemical activity [26], to list a few examples. The sensing areas of these machines are bound to specific regions, and so proper cell positioning is important. Ideally, there would be a cell on every sensor and only one cell per sensor. However, researchers commonly seed cells randomly on devices [22-25, 27, 28], with little control on cell number and position with the hope that some cells will fall in the desired location and number. They do this because controlling the position of

individual cells is a difficult task [20].

1.2 Cell Loading Requirements

While random cell seeding is appropriate to show device proof-of-concept, controlled cell positioning is needed to advance single cell sensing work. In the case of the cell clinics chip, the eventual target of the method presented, cells would be loaded into the microvials. For that specific target the requirements on the cell loading method are:

- It must take cells suspended in an aqueous solution and bring them into the microvials.
- It must work with the cell clinics chip, that is, near or around metals, insulators, and semiconductors. This includes metal lines under the CMOS passivation layer, the polypyrrole/gold bilayer hinges, and the SU8 vias.
- It must not harm the cells it manipulates, since they are to be cultured for long term study.
- It must work with anchoring cells (e.g., neurons) and non-anchoring cells (e.g., lymphocytes.)
- It must be able to load 1 to 10 cells into each vial, and hundreds to thousands into the entire vial array, in a controllable fashion.
- It must be able to load cells into different vias simultaneously, and load all vias in a matter of minutes.
- It must be able to last the lifetime of the chip, that is weeks to months.
- It must be CMOS- and MEMS-based and integratable with the cell clinics chip.
- It must be able to be automated and controlled using on-chip integrated circuit logic.

1.3 Single Cell Manipulation Methods

This section discusses various single cell manipulation methods and discusses each in terms of the cell clinics cell loading requirements. Table 1-1 compares different cell manipulation methods in terms of the number of cells they can manipulate, whether they

can manipulate cells in series and in parallel, whether their integration with integrated circuit technology (such as CMOS) is possible, and whether they can be used in the cell clinics chip to load cells into microvials.

Table 1-1. Comparison of different technologies for cell manipulation

Method	Individual cells	Many cells	Parallel manipulation	Many cells independent of each other	Integratable with CMOS/MEMS	Applicable to cell clinics [3]?
Surface chemistry [19, 29]	no	yes	yes	no	yes	Lacks accuracy and vial loading capability. Limited to anchoring cells
Grippers[18, 30, 31]	yes	no	n/a	n/a	no	No parallel manipulation. Not integratable.
Hydrodynamic traps (suction) [13, 32-39]	yes	yes	yes	yes	no	Not integratable.
Hydrodynamic traps (laminar flow) [20]	no	yes	yes	no	yes	Lacks accuracy
Hydrodynamic traps (electroosmotic tweezers) [40]	yes	yes	yes	yes	yes	Cannot bring cells into vial
Gel traps [20]	yes	yes	yes	no	yes	Poor positioning control. One shot loading.
Optical tweezers [20]	yes	< 10	yes	yes	no	Slow. Not integratable.
Acoustic wave traps[20]	no	yes	yes	no	no	No individual cell manipulation. Destroys MEMS
Dielectrophoresis [41]	yes	yes	yes	yes	yes	Meets basic requirements

1.3.1 Surface Chemistry

One method to segregate the positioning of cells is based on substrate surface chemistry. This method works because cell adhesion is mediated by cell membrane receptors that interact with the surface [19, 29]. Researchers have controlled the location of cells by selectively treating surfaces with various materials [29, 42, 43], including metals, polymers, self-assembled monolayers, and proteins [15, 29]. Cell patterning is usually irreversible [20].

In the context of the cell clinics chip, this approach is inappropriate because it cannot be used to control the number of cells adhered (it serves only to allow or deny the presence of cells on defined regions) and it can only be used with anchoring cells [20]. Since cells are not actively placed inside the vials, all the vials may not be loaded with cells after each loading procedure. The surface treatment must be effective for the cells being used, and this treatment may change for different cells [20]. This restricts the combination of cells that can be used in the cell clinics chip. Also, the surface treatment must last anywhere from weeks to months to prevent cell migration, and some surface chemistry treatments do not last that long [20].

1.3.2 Grippers

Another method to position cells is to physically grip and move them with the gripper.

Various actuating technologies have been used in the fabrication of microgrippers that work in water, these include thermal actuation [30], electroactive polymers [18], and shape memory alloys [31]. This method gives control of the position of the cell because the gripper could be moved arbitrarily while holding the cell.

In the context of the cell clinics chip, the disadvantages of this method are that only one cell can be manipulated at the time therefore loading many cells would take a long time, and that it would be difficult to integrate with the CMOS chip.

1.3.3 Hydrodynamic Traps

In 1945, Hodgkin and Huxley used hydrodynamic trapping in their Nobel Prize winning work [44]. They used suction to keep a cell trapped on the tip of a conduit in their patch clamp setup [44], and similar setups using modern microfabrication techniques are still being explored [45]. More recently a similar method, using conduit tips microfabricated on active substrates (i.e., with sensors), has been used to trap and monitor single cell activity [13, 32-39].

This technique is advantageous because it is precise and because attracting cells by fluid drag places minimum requirements on the cell. However, these devices use passive substrates, devoid of most electrical elements, because integrating high density integrated circuits such as the CMOS chips used in the cell clinics project is difficult and it requires a lot of chip area. Therefore, this method is inadequate for the cell clinics chip.

Other versions of hydrodynamic manipulations are to sieve cells from the flow using mechanical barriers [20], and retaining cells in regions of low shear stress [20]. These methods, however, have low patterning precision and array sites often remain empty or with cell aggregates instead of single cells [20], which also makes them inadequate.

1.3.4 Gel Traps

Cells can be encapsulated in hydrogels such as agarose [20] in a matter of seconds using UV radiation, and cell structures can be created using this approach [20]. The gel serves as mechanical support to the cell and once trapped the cell will remain in place indefinitely, until the gel is dissolved.

Gel trapping cannot be used to move cells to a desired location, it is difficult to define the number of cells trapped, and once the gel is crosslinked no more cells can be placed at that location. These aspects make gel trapping incompatible with the needs of the cell clinics project.

1.3.5 Optical Tweezers

Optical tweezers use laser light to exert forces on bodies, such as a cell. The force occurs because of the transfer of photon momentum when the cell, which must have a different index of refraction as the medium, bends the laser light [46]. Cells can be positioned and

moved in arbitrary ways, including in 3D. Optical tweezers typically operate on one cell at the time. Holographic laser arrays can be used to control multiple cells at the same time [47], but the number of traps is limited because the power of the main laser beam is shared by all the traps [20].

Since in the cell clinics project we need to load a larger number of cells (hundreds to thousands), then loading cells using this method would take a long time. Laser tweezers are not integratable with integrated circuits, and thus would condemn the cell clinics chip to the laboratory where the laser tweezers are located. Otherwise, this method could be used to load cells into microvials, and in fact I collaborated Dr. W. Losert (Department of Physics, University of Maryland at College Park) and his group in pursuing cell loading into vials using a holographic laser tweezers array; key experimental demonstrations are still underway.

1.3.6 Acoustic Wave Traps

Acoustic wave trapping is the least developed manipulation method of those discussed thus far. Ultrasonic standing waves, produced by piezoelectric transducers, exert forces on cells based on the density difference of the particle and the medium [20], causing cells to accumulate at the nodes of the standing waves [20]. All cells present are affected equally and therefore it is difficult to control one cell independently of others. This makes acoustic wave traps inadequate for the cell clinics chip. Another disadvantage is that ultrasound waves are capable of destroying MEMS device features (as I observed in

the laboratory), so successful integration in lab-on-a-chip is yet to be demonstrated.

1.3.7 Dielectrophoresis

Finally, we come to dielectrophoresis, the preferred method and focus of this dissertation. Dielectrophoresis uses electric fields to manipulate cells and other uncharged particles. It can be used to manipulate single [48] or many cells [49] in parallel. It uses DC as well as AC fields, and the forces can be attractive or repulsive based on the electric field frequency. The force distribution is determined by the shape of electrodes producing the electric fields. Since this method only requires electrodes and an electric signal, it can be fully integrated with integrated circuit chips. In addition dielectrophoresis meets all the other requirements mentioned in Section 1.2.

However, electrode design is difficult because the forces depend on the electric field gradient. In addition, dielectrophoresis is affected by the presence of conductors and insulators because electric fields are disturbed by them. These two issues must be addressed before dielectrophoresis can be implemented in the cell clinics chip, and this is done in this dissertation.

1.4 The Dielectrophoretic Effect

The devices and the final design presented in this dissertation rely on dielectrophoresis to manipulate cells. Therefore it is crucial for the reader to understand this phenomenon. In

this section dielectrophoresis will be explained in detail.

When a small neutral particle is in an electric field, an electric dipole is created within the particle due to the separation of positive and negative charges [50]. The charges are attracted to the electrode of opposite sign and also repelled by the electrode of the same sign. The forces on the dipole charges, both positive and negative, are proportional to the product of the electric field strength and the electric charge. If the particle is in a uniform electric field, like that illustrated in Figure 1-2, then the particle will experience no net force because the attractive and repulsive forces are equal, in other words the magnitude of the attraction of the (+) electrode on the (-) charges of the dipole is equal to the repulsion of the (+) electrode on the (+) charge in the dipole, and like wise with the (-) electrode. (Note that if a particle has a net charge, then it would undergo a net force in the presence of a uniform electric field, and this is called *electrophoresis*. This phenomenon is not the same as *dielectrophoresis*.)

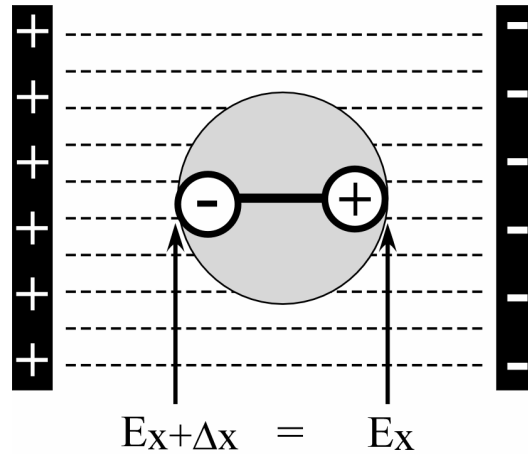


Figure 1-2. The charges of a particle are separated by an electric field. If the electric field is uniform, no net force is exerted because the electrostatic forces on the dipole (charge times electric field) balance.

However, if there are gradients in the electric field (if the field is uneven) then the field strength is greater on one side of the dipole than the other, as illustrated in Figure 1-3, and then the attractive and repulsive forces from the electrodes on the dipole are not balanced, i.e., the attraction of the (+) electrode on the (-) of the dipole is *greater* than the repulsion of the (+) electrode on the (+) charge in the dipole. Thus, the particle experiences a net force. This phenomenon is known as dielectrophoresis [51].

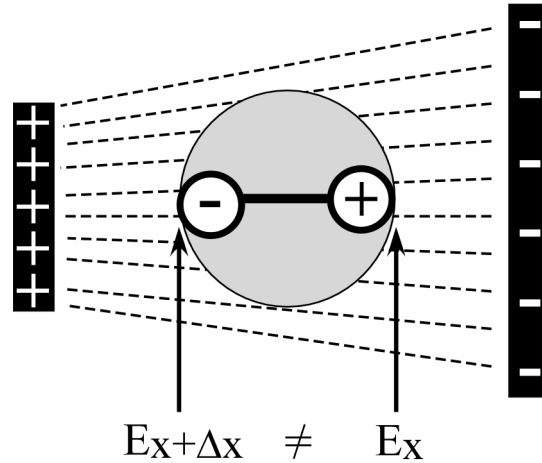


Figure 1-3. If the electric field is not uniform, the forces on the dipole due to the electric field are not balanced, and a net force is exerted.

In quantitative terms, the net force F upon the particle is the dipole moment p (vector) times the gradient of the electric field E [52]

$$(1) \quad \vec{F} = (\vec{p} \cdot \nabla) E$$

This equation is in the time domain, meaning that they apply at any instant in time. The electric field is the spatial gradient of the electric potential, which can be found solving Laplace's equation [50]. The dipole moment, for an isotropically, linearly, and homogeneously polarizable particle, is

$$(2) \quad \vec{p} = \alpha V E$$

where α is the polarizability tensor (or dipole moment per unit volume) and V is the volume of the particle. The polarizability is positive if the particle is more polarizable

than the medium, and this causes the particle to be attracted to the high field gradients. If the medium is more polarizable than the particle then the polarizability is negative and this causes the particle to be repelled from high electric field gradients. This is analogous to Buoyancy forces that push bubbles down if they are heavier than the surrounding fluid (water drops in air) and up if they are lighter than the surrounding fluid (air bubbles in water). The force on the particle then becomes

$$(3) \quad \vec{F} = \alpha V (E \cdot \nabla) E$$

However, the reader may be more familiar with the equation

$$(4) \quad \vec{F} = \frac{1}{2} \alpha V \nabla |E|^2$$

which is more commonly given in dielectrophoresis discussions, and that is obtained after we apply the identity $(E \cdot \nabla) E = \frac{1}{2} \alpha V \nabla |E|^2$ to Equation (3).

I find Equation (4) to be unsuitable to explain dielectrophoresis, because the physical meaning of each term is masked by mathematical manipulations. However, this expression is more convenient than Equation (3) when evaluating the dielectrophoretic force because it simplifies the problem: vector calculus is circumvented and the force direction is found instead by taking the gradient of a scalar (the magnitude of the electric field squared).

In dielectrophoresis the sign of the charges or direction of the electric field does not

determine the dielectrophoretic force direction. The direction of the force is determined by the direction of the field gradient and by the polarizability of the particle. Therefore a direct current (DC) signal is not necessary (in contrast to *electrophoresis*), and time varying, alternating current (AC), electric fields can also be used to exert dielectrophoretic forces. In an AC field, the dipole orientation changes as the electric field changes resulting on a force, just as if the field was not changing in time. Using AC fields has the great advantage of avoiding electrochemical reactions at the electrodes. This is one of the reasons why the vast majority of dielectrophoresis work is done using sinusoidal AC electric fields. If using an AC electric field, we are more concerned on the resulting time-average dielectrophoretic force than in the instantaneous force because typically the signal period is small compared with the time it takes to move the particle a noticeable distance.

Through quasi-static analysis, given a sinusoidal field, Equation (4) becomes [41]

$$(5) \quad \vec{F} = CV\epsilon_m \operatorname{Re}(CM) \frac{\nabla |E|^2}{2}$$

where ϵ_m is the permittivity constant of the medium, C is a geometric constant¹, and $\operatorname{Re}(CM)$ is the real part of the Clausius-Mossotti factor. CM is the relative polarizability of the particle with respect to the medium, and it is a function of field frequency. The Clausius-Mossotti factor is

¹ For a sphere, $C = 3$, resulting in Equation (5) to become $\vec{F} = 2\pi\epsilon_m R^3 \operatorname{Re}(CM) \nabla |E|^2$,

where R is the particle radius.

$$(6) \quad CM = \frac{\overline{\varepsilon_p} - \overline{\varepsilon_m}}{\overline{\varepsilon_p} + 2\overline{\varepsilon_m}}$$

where the subscript m corresponds to the medium and p to the particle. The parameter $\overline{\varepsilon}$ is the complex permittivity. Assuming a sinusoidal electrical field, this term is

$$(7) \quad \overline{\varepsilon} = \varepsilon + \sigma/(\omega \cdot i)$$

where ε is the permittivity, σ is the conductivity of the substance, and ω is the field frequency. If the particle is inhomogeneous, then the effective permittivity and conductivity are used instead. These parameters are a function of frequency and the material properties and geometries of all the structures inside the particle. A common way to find the effective conductivity and permittivity of cells is using a multiple-shell model [53].

Equations (5) - (7) are widely reported in the literature as the dielectrophoretic force, but as just explained they are simply a subset of Equation (1), applicable only to a single-frequency sinusoidal electric field between two electrodes. Equations (5) - (7) alone cannot be used to find the effect of electric fields neither when produced by multiple electrodes nor when the periodic signal is not sinusoidal. Chapter 3 presents for the first time how can the dielectrophoretic force be calculated when either or both of these situations arise.

1.5 Chronological Overview of Dielectrophoresis

Since each chapter of this dissertation starts with a literature review relevant to the work in that chapter in particular, in this section I provide an overview of the work done by the dielectrophoresis community through the years. Based on current trends, I extrapolate into the future of the field.

This overview is important because it provides the historical context within which this dissertation appears. This dissertation takes dielectrophoresis a step forward in the transition from scientific novelty to engineering applications, and the overview shows that this is needed by the field of dielectrophoresis. Discussions on the future of dielectrophoresis are important because they project the relevance of the work presented and highlights opportunities in the field not covered by this work.

The interest on dielectrophoresis is illustrated by the rate at which publications related to dielectrophoresis have grown through the years. Figure 1-4 shows the number of journal article publications related to dielectrophoresis since it was first explored in 1958, in logarithmic scale. It shows that the number of publications related to dielectrophoresis is growing at a faster rate (10%/yr.) than the average number of scientific journal articles published in the USA (3.9%/yr.) [54], shown by the dashed line (taking the number of dielectrophoresis publications in 1965 as the baseline). In this chronological overview I show the major reasons for such growth and highlight important milestones.

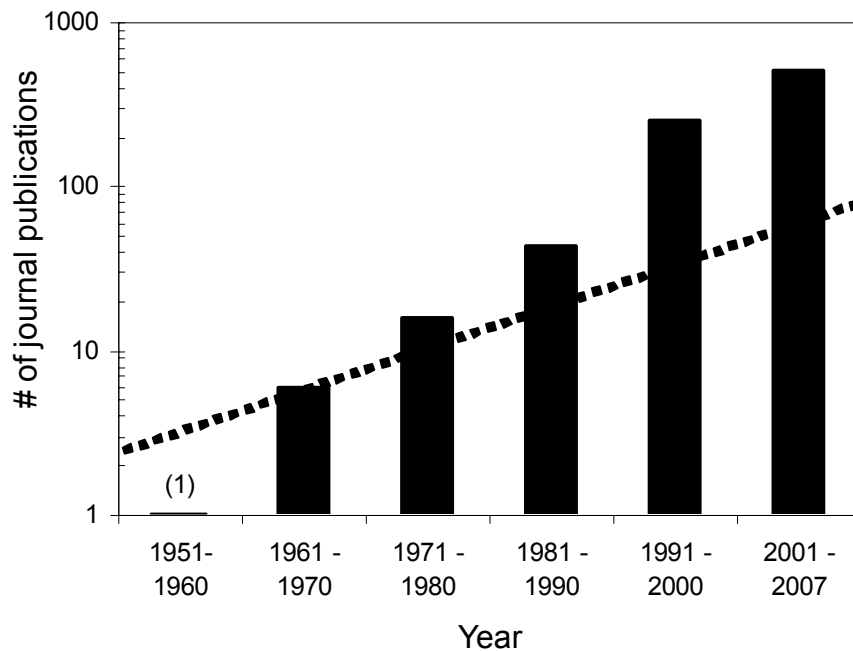


Figure 1-4. Number of dielectrophoresis-related journal publications published per decade (logarithmic scale). The number of publications was obtained from my personal library and from searching the keywords “dielectrophoresis” and “dielectrophoretic” in ISI Web of Knowledge. The dashed line shows the trend that would be expected based on the average journal article publication growth rate observed in the USA [54].

1.5.1 The Past

H. A. Pohl was the first to study dielectrophoresis [51, 52, 55-57]. He and his collaborators laid the theoretical foundations for the dielectrophoretic phenomenon from the late 1950s through the early 1970s. Pohl presented the governing equations for

dielectrophoresis in a homogeneous particle as early as 1958 [51]. In 1966, Pohl and Hawk [55] described the separation of live and dead yeast cells in an uneven AC electric field. This was perhaps the first biological application of dielectrophoresis. Pohl mentioned that this phenomenon is not electrophoresis (which was widely known at the time) but was instead due to the alignment of dipoles within the particle and the electric field gradient. Yeast cells were not damaged by dielectrophoresis, as demonstrated by culturing them in agar medium after the experiment [55]. In 1968, Crane and Pohl [58] expanded the work on yeast cells and found that the electrical field frequency response of live and dead cells is different [58], thus providing the basis for many applications for which dielectrophoresis is used today. Four years later, another paper by Crane and Pohl [59] presented a model to predict the relative polarization of inhomogeneous particles as a function of frequency, which allowed the behavior of real particles, such as cells, to be predicted. Using this model, Crane and Pohl successfully predicted experimental observations on the dielectrophoresis behavior of live and dead yeast cells.

During the 1970s and 1980s, published work using dielectrophoresis became more frequent [53, 60-70]. The seed planted decades beforehand started to germinate. Experimental work mainly aimed at corroborating early observations [60, 61, 63, 64], while the theoretical work aimed at ways of modeling more complex situations [53, 62, 63, 65, 68].

In the late 1980s the dielectrophoresis community started adopting microfabrication

technologies [71]. The capability of fabricating electrodes and chambers with accuracy, combined with powerful modeling capabilities (enabled by numerical models and modern computers), gave rise to an explosion of work during the 1990s [72-101]. Researchers working on dielectrophoresis pursued theoretical work [73, 82, 88, 93, 96, 100, 102, 103], carried basic experiments [72, 81, 84-87, 91, 96, 97, 101, 104], and started to produce microsystems aimed at specific applications, such as particle separation [72, 74] [78], single cell manipulation [73, 75, 79], disease detection [76, 80, 83, 92, 94, 95], and microparticle characterization [89, 90], among other. In addition, traveling wave dielectrophoresis (TWDEP) first appeared as a new approach for manipulation of particles [81, 85, 96-98, 102].

During the 1990s dielectrophoresis reached important milestones. Researchers began manipulating sub-micrometer particles and single molecules [87, 105], and literature reviews on the subject started to appear [105-108].

1.5.2 The Present

With the turn of the century the amount of work published using dielectrophoresis continued to increase. Nearly 480 journal articles were published between 2000 and 2006, more than the total number of journal articles published prior to 2000. The birth of the concept of a lab-on-a-chip [16] gave dielectrophoresis a new *raison d'être* as a manipulation technology [5, 48, 109-118]. Dielectrophoresis applications became more intricate [6, 7, 49, 75, 109, 113, 119-126], of which molecular transistors [119],

manipulation of DNA [120, 127, 128] and proteins [123, 129], single cell manipulation [48, 75, 110, 113, 130], and assembly of 2- and 3D microstructures (inert and living) [5-7, 125, 126, 131, 132] are notable examples. At this point the basic dielectrophoresis phenomenon, and variations such TWDEP became established. Theoretical work and basic experimental work in this period mainly focused on tools that could be used to design dielectrophoretic devices [100, 133-143], though new techniques, such as electroless dielectrophoresis [138, 144] and multiple frequency dielectrophoresis [143, 145, 146] also appeared. Despite the advances that dielectrophoresis work has made, expressed in terms of the number of journal-published applications, it still needs to fully transition from science to engineering, indicated in part by the lack of commercial products. The historical importance of this dissertation is that it takes dielectrophoresis a step forward in the transition towards engineering and practical applications.

1.5.3 The Future

In my opinion, the most interesting application of *history* is to use it to try to predict the *future*. A goal of this chronological overview, other than to provide a context to this dissertation, is to serve as a launching pad to predict future trends in dielectrophoresis. These trends encompass more than the scope of this dissertation, and thus do not quite belong to the conclusion of this dissertation. I will undertake this exciting and speculative task in the next few paragraphs.

Basic understanding of dielectrophoresis has been established and knowledge of its

existence is disseminating rapidly. Dielectrophoresis is transitioning from being a curiosity and a matter of research to a well understood phenomenon and a tool that can be used in system applications. This transition started to occur early in the century, along with the blooming of lab-on-a-chip research.

I believe that in the foreseeable future a lot of dielectrophoresis work will be related to biological studies and applications, mainly in the form of lab-on-a-chip applications, because these topics are of public interest due to the aging of the baby boomer generation and the threat of bio-terrorism. Dielectrophoresis can be used in lab-on-a-chip sample preparation and manipulation [147-149]. Since sample preparation appears to be the missing factor for lab-on-a-chip devices to claim full independence from the laboratories, we can expect to find dielectrophoresis to be increasingly a part of lab-on-a-chip systems. In some niche applications dielectrophoresis may take over as the main technology used, some existing examples of this are DEP-based devices for the detection of malaria [76] and cancer [95, 150].

In a related field, I predict that the concept of lab-on-a-chip will be expanded to factories-on-a-chip. Some steps have begun in this direction. For example, three-dimensional microscopic structures [131], heterogeneous cell consortia [6], neurological networks [7], and multicellular, heterogeneous, liver assemblies [5] have already been demonstrated, all of them taking place in microfluidic chips. Though the authors of these demonstrations have not expressed it, their work is fundamentally different to lab-on-a-chip work because it pursues the fabrication of products, not the analysis of substances.

The authors presented early factories-on-a-chip, even if they do not realize it. Recently I proposed and demonstrated the proof of concept for fabricating arteries out of disassociated tissue in a single step [146], which opens the door to novel medical treatments. With similar techniques I would like to assemble organs and machines from the bottom up. The main limitations in the progress of factories-on-a-chip are our imagination and electrode design techniques, because the electrodes (and other topographies such as insulators and conductors present in the area of dielectrophoretic manipulation) determine the shape of what can be assembled.

Another field in which dielectrophoresis has potential is in the industrial production of nanoelectronics. Nanomaterials are assembled on integrated circuits by fabricating and then exciting electrodes that attract nanoparticles suspended in a solution, these same electrodes then serve to connect the nanoparticle to other components [119, 126, 151]. Examples of nanoelectronics assembled in the laboratory include gold nanoparticle transistors [119] and UV detectors [151]. Though a step forward, the fabrication of nanoelectronics needs to go great lengths because currently the electrodes are large in comparison with the nanoparticle. Though there may be inherent advantages in employing nanoparticles, the high density integrated circuits that one imagines when discussing nanotechnology are not possible until discrete nanocomponents are connected together through nanometer-scale electrodes to make up whole circuits. For dielectrophoresis-based nanoelectronics to take root, the distribution of electric fields, which gives rise to the force distribution, needs to be at the nanometer scale so that multiple nanometer-scale components can be assembled together to create functional

circuits, without having to interface each component using large electrodes. That way, nanometer-scale functional circuits can be assembled, and extremely high density of electrical components can be achieved.

Let us consider the integrated circuit of nanometer feature dimensions illustrated in Figure 1-5. Different nanoparticles (type 1-4), each having with different properties, are to be assembled on a substrate (Figure 1-5A). The discrete components are assembled to perform complex operations, and thus the only large electrode needed are for input/output interfacing (Figure 1-5B). I suggest that the assembly of such integrated circuit should take place by creating a dielectrophoretic force field like that illustrated in Figure 1-5C, in which each color represents dielectrophoretic forces attractive to that particle type and repulsive to all others. From the dielectrophoretic assembly point of view, this approach requires two things for it to become a reality: 1) the generation of multiple electric fields selective to each particle type and 2) the generation nanometer-sized electric field gradients. The first requirement can be pursued by means of multiple frequency dielectrophoresis [146], however, the generation of such small field gradients is a challenge that it is not clear to me at this point how it can be addressed.

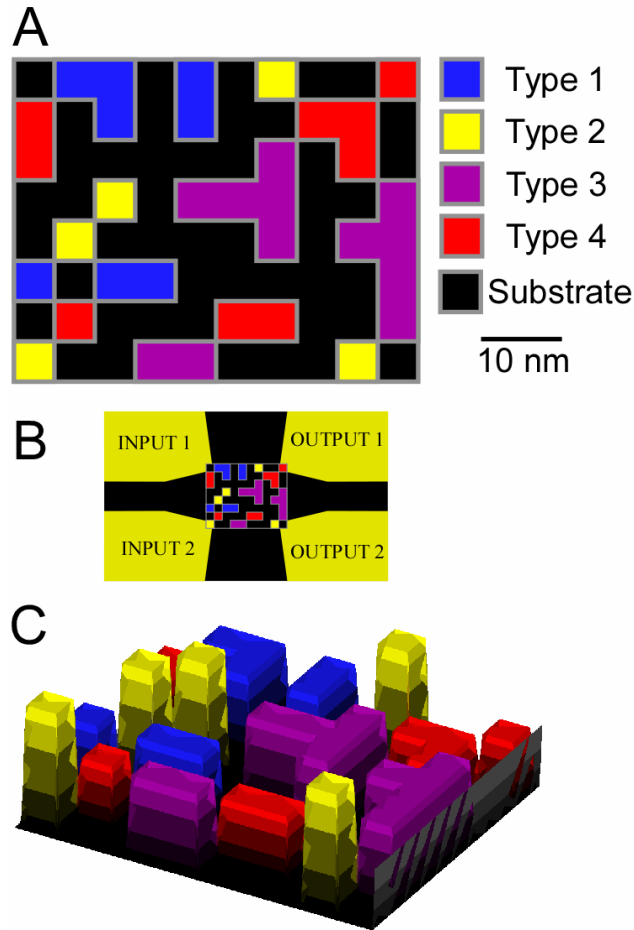


Figure 1-5. Schematic of dreamed nanometer-scale integrated circuit. The substrate and nanoparticles of different properties, sizes, and shapes provide functionality. To make it using dielectrophoresis it would be necessary to distort the electric fields at scales of < 5 nm.

Given that two of the application branches (factories-on-a-chip and nanoelectronics) that I just described will be limited by the way we design the electrodes, a paradigm shift in electrode design is, in my opinion, necessary. Currently we design electrodes based on what I call “intellectual momentum” (which means doing things the same way they have

been done, even though it may not be the best way. Intellectual momentum is well illustrated by the barrage of work done using interdigitated electrodes [77, 83, 94, 95, 112, 120, 121, 137, 139, 141, 142, 145, 152-155], which is a geometry that served its purpose in the demonstration of dielectrophoresis long ago), as well as convenience of fabrication methods (only using electrode geometries that are easy to make, such as planar electrodes), and instincts. There are limited publications that help design electrodes given a desired force distribution [100, 134-137, 141-143]. This effort must continue because for dielectrophoretic devices to bloom as a serious tool in high complexity machine fabrication, we need to design electrodes based on the force distribution desired, not on what can be done with the knowledge we have. Finding the electrodes that would result in the desired force distribution will likely be difficult, it may involve multiple non-symmetrical electrodes, insulating and conducting structures that distort the fields, and 3-D electrode geometries which may be difficult to fabricate. I believe that finding the topography needed to obtain a certain dielectrophoresis force distribution will be an area of fundamental development in the subject of dielectrophoresis. Based on publication trends, it appears as if theoretical work is waning in favor of work on applications. However we need great progress on the theoretical and modeling aspects of dielectrophoresis to be able go beyond the applications enabled by existing theory.

Possible approaches towards desiring a force distribution and then making it happen are either configurable electrode arrays, analogous to pixels in a screen (steps in this direction have been taken by [75, 113, 115, 156]), or freeform patterns produced by

optoelectronic dielectrophoretic tweezers [122, 157]. The force distribution desired could be formulated mathematically, and used as the inverse solution of the electric field gradient problem. This is the approach that Dr. Shapiro has taken to steer particles using electroosmotic flow [40] (Dr. Shapiro's work seems to be in line with my vision of making machines that do what we need them to do, not whatever is easier to make them do.) Solving this mathematical problem is not a trivial one because the problem is non-linear (the dielectrophoretic force depends on the *gradient* of the *square* of the electric field, whereas voltage is what is controlled), and because multiple solutions are likely to exist. Multiple frequency dielectrophoresis [146] can be used to increase the control and selectivity of the particles, but it is likely to make the mathematical problem even harder by providing even more simultaneous solutions. However, given the constant increase in computational power, and its constant drop in price, these are surmountable obstacles.

1.6 Cell Loading Method Overview

The method described in this dissertation to load cells is schematically illustrated in Figure 1-6. The loading method consists of microfluidic channels, cell cages, and various electrodes. The electrodes are used to create electric fields that exert dielectrophoretic forces on the particle, and these forces can be controlled by controlling electrode voltage.

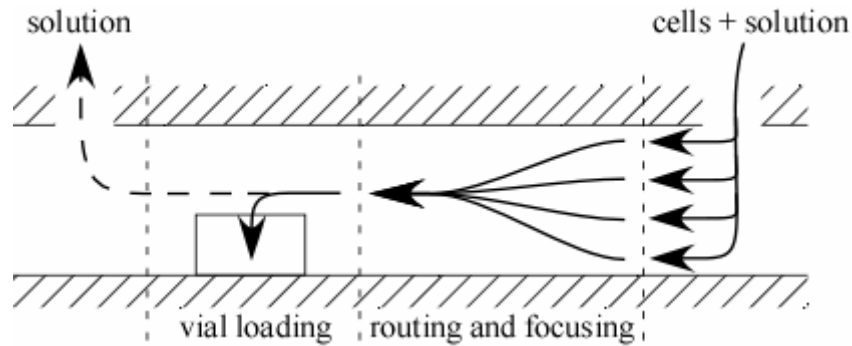


Figure 1-6. Schematic of the cell loading method presented.

A solution with cells suspended in it is pumped by a syringe pump through a microchannel. In this microchannel, cells go through a section in which they are routed, using dielectrophoresis, to different branches of a microchannel network and focused to a given channel height, also using dielectrophoresis. The microchannels lead to a chamber with many cell cages. When the microchannels reach the chamber, each branch outputs cells so they flow above different rows of cell cages. Cell cages attract cells into them by means of dielectrophoresis, thus loading the cells. If the cages are not activated, cells continue moving with the solution and out of the microchannel. The solution, with cells that were not loaded, can be discarded or recirculated

1.7 Device Materials and Fabrication Methods

Devices were fabricated to demonstrate aspects of the manipulation and loading method. The devices are described in each section that discusses them, but they all were fabricated using similar materials and fabrication methods. This section describes these materials and methods, all of which are commonly found in the fabrication of

microelectromechanical systems.

Devices were fabricated on a flat substrate. Though various materials would have been appropriate as a substrate, the main substrate material used in this work was single crystal (100) silicon (500 μm thick wafers) with 1 μm of silicon dioxide on the surface. This material was chosen because it is flat, because its surface is cleaned extremely well by the manufacturer and because its properties are well understood. Also, it is the same material as the cell clinics chip, so it shows that this substrate is appropriate for cell loading (i.e., does not interfere with dielectrophoresis).

The material used to fabricate the microchannels and the cell cages is SU8, which is a photopatternable epoxy polymer [158]. SU8 is provided by the manufacturer as a liquid. An SU8 film is deposited on a substrate using a process called *spinning*. In this process, an amount of the substance is placed on top of the substrate, the substrate is placed on a vacuum chuck, and the substrate is spun. Spinning speeds range from 100 to 5000 rpm. Charts specific to the type of SU8 being spun relate the spinning speed and time with final film thickness, and SU8 formulations of different viscosities are used to obtain different range of film thicknesses. Once the SU8 is spun the substrate is baked on a hot plate to remove solvents in the SU8 film.

Once solvents are removed, the SU8 film is patterned using a process called *photolithography* [159], and this process is enabled by the fact that SU8 is crosslinked by ultraviolet (UV) light radiation. During photolithography, different SU8 regions are

selectively crosslinked by placing a mask with a given pattern between a UV light source and the SU8. SU8 under transparent mask regions, through which light can pass, will be crosslinked and SU8 under opaque mask regions will not be crosslinked. Typical 365 nm wavelength (UV) light exposure doses range from 50 to 700 mJ/cm², depending on film thickness. After exposure and further baking, SU8 is developed with a solvent provided by the manufacturer that dissolves uncrosslinked SU8.

The electrodes on the substrate floor and on top of the cell cages are made of chromium/gold (Cr/Au). These metals are deposited using a process called *thermal evaporation* [159]. During thermal evaporation, the substrate is placed in a vacuum chamber. Small amounts of Cr and Au are heated to the point of evaporation (sublimation, in the case of Cr) on a tungsten boat that is heated by running an electric current through it. The metal vapor condenses on the substrate and chamber walls, creating a uniform film on areas within line-of-sight from the metal source; surfaces outside line-of-sight are coated unevenly, if at all. Typical film thickness range from 100s to 1000s of Å. Cr is deposited because it enables adherence of the Au to the substrate which would otherwise not adhere to silicon or silicon dioxide. Au is deposited on top of the Cr during the same evaporation session (while keeping the substrate under vacuum) because otherwise there is poor adhesion between the Cr and the Au films. Au was chosen because it is chemically more stable than other available metal choices (such as Al or Cr), and chemical stability is desirable because the electrodes will be excited at voltages as high as 20 V in aqueous media and electrochemical reactions would degrade most other metals (under certain conditions the Au on the electrodes was still visibly

degraded during experiments.)

Cr/Au needs to be patterned with the shape of the electrodes and electric contacts. Two methods were used to pattern the Cr/Au: *wet etch* and *lift-off*.

Wet etch [159] consists on exposing a material, in this case Cr and Au, to liquid (wet) chemicals that react with (or etch) the metal, thus removing it. To etch the material selectively, a mask material is patterned using photolithography on top. The mask is typically photoresist. After the metal is etched, the photoresist is removed using acetone. At the end of this process metal will remain only on the regions on which photoresist was present.

Lift-off [159] consists on depositing and patterning a sacrificial layer before the metal is deposited. The sacrificial layer used is typically photoresist. After metal deposition the sacrificial layer is removed using acetone, lifting away the metal that was laid on top of it. At the end of this process will remain only on the regions on which the mask was not present.

Fabricating electrodes on top of the vials is challenging, because the cell cages are relatively tall (50 μm). Spinning the photoresist near such structures will cause the photoresist to be uneven. In addition, the mask cannot be brought in direct contact with the substrate, as typically done, because the presence of the vial. Lastly, the film is exposed to higher UV doses than usual in order to pattern the photoresist on the cage side

wall, which is parallel to the light rays. I found, as would be expected, that all these issues result in poor patterning of the photoresist. To pattern the metal, I chose between lift-off and wet etching based on which method resulted in appropriate patterns despite these problems. I chose the lift-off method to pattern the metal on top of the vials. Details on the way photoresist is affected by the presence of the vials are given in Appendix A.

The electrodes on the ceiling, present only in some of the devices, are made of indium tin oxide (ITO), a transparent conductor. This material was chosen because the cell loading can be monitored despite its presence. Glass slides (1" x 3") covered in ITO were purchased (Structure Probe Inc.), and patterned using standard photolithography and wet etching.

I used yeast cells to demonstrate the devices fabricated. Yeast is a well studied organism in the context of dielectrophoresis [51], it is easy to prepare for experiments, inexpensive, and readily available at grocery stores. Live and dead yeast cells have different dielectrophoretic responses [55], and methylene blue readily stains dead yeast cells [104, 160], making live and dead cells distinguishable. These characteristics make live and dead yeast convenient to use when illustrating the operation on different particle types.

1.8 Cell Loading Challenges

The cell loading method presented will eventually be integrated with the cell clinics chip.

This means that the devices used to demonstrate cell loading have to be able to be implemented on the cell clinics chip and the fabrication methods to make these devices have to be compatible with CMOS technology. CMOS chips can not be exposed to temperatures higher than 350° C (as determined experimentally by M. Dandin, IBIS/Laboratory for Microtechnologies, by monitoring the performance of CMOS transistors as a function of temperature.) The fabrication process must not harm the materials exposed on the cell clinics chip, which include aluminum, silicon dioxide, silicon nitride, silicon, gold, and polypyrrole. Each vial has a lid that opens and closes thanks to a polypyrrole/gold bi-layer hinge [161]. The lid and the hinge can be damaged by ultrasonic waves, which are sometimes used to clean devices or to promote the wetting of crevices, and thus must be avoided.

As mentioned before, the presence of the cell cages makes photolithography, necessary to pattern electrode on top of the cage, difficult. Any photolithographic step done over the cell cages has to take this in consideration.

Since central aspects of the cell clinics chip (e.g., circuits, bilayer-actuated lids, vials) have already been developed over more than 5 years of research, it is important to design a cell loading method that does not require significant changes to this system. This means that the loading method has to work near conductors, semi-conductors, and insulators, and in and around the vials. In the context of dielectrophoresis, these electrical and geometric inhomogeneities produce electric field distortions that cause what are known as parasitic traps [115] (regions where dielectrophoretic forces are

undesirably attractive or repulsive). Parasitic traps present a significant challenge to load cells into the cages.

The loading method should work with the current and future versions of the cell clinics chip. The current configuration of the cell clinics chip is shown in Figure 1-7. In the current configuration the chip is packaged in a 40-pin dual in-line package (DIP40) and custom packaged with a photopatternable polymer [162] (invented by Sam Moseley and I, and developed by me) that covers the electric wirebonds that otherwise would be exposed to the cell solution. A plastic tube segment is glued on top of the DIP40 chip chamber to create a well that holds enough cell culture solution to sustain the cells for about two days (the well solution was developed by N. Nelson and S. Prakash). The chamber is ~5 mm tall and it has no cover. In the current configuration, cells suspended in a solution are placed on the chip and then they settle on the surface. There is no forced fluid flow. The cell loading device must be take cells settling above the chip surface and bring them close to the sensors. By working with the current cell clinics configuration, the loading cell device helps the development of this cell clinics system. The future version of the cell clinics chip will be integrated with microfluidics that will be used to supply cells, nutrients, and samples to the chip.

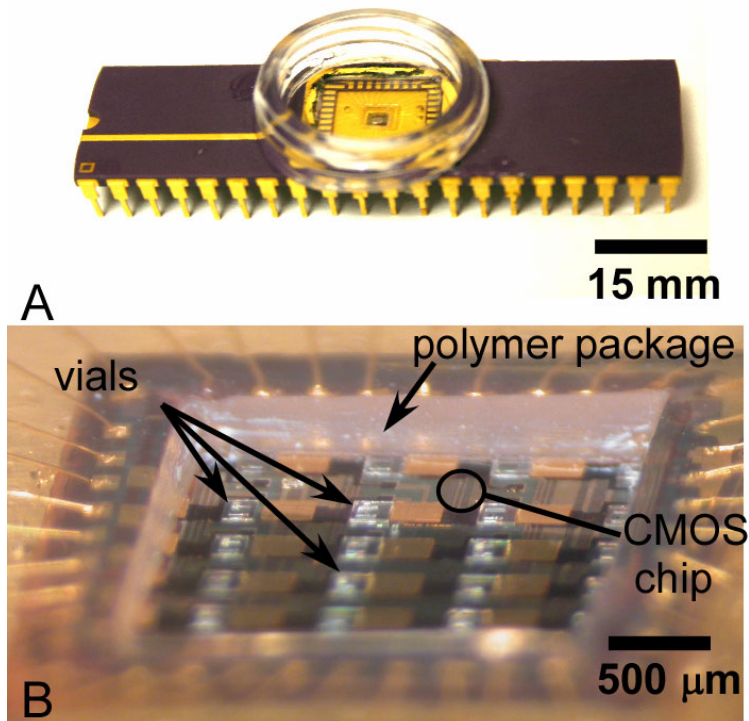


Figure 1-7. The current configuration of the cell clinics chip uses a DIP40 and a custom polymer package around the wirebonds.

The main challenge in the cell loading method is designing it. There are few guidelines in the literature that help in the design of dielectrophoretic devices [100, 133-143] and none of which applies to loading cells into cages. The heterogeneity of materials and geometries in the regions of dielectrophoretic manipulation is something that the dielectrophoresis community appears to be avoiding. The trade-off between the different parameters involved is not known. All this makes the design of a cell loading device challenging and worthy of a Ph. D.

1.9 Organization of Dissertation

The first chapter of this dissertation serves as an introduction to cell manipulation methods and to dielectrophoresis. It provides an overview of the cell loading device presented and outlines the main challenges associated with designing this device.

Chapter 2 discusses the design of flow-through sorters and introduces a design method that makes the design of flow-through sorters considerably easier than previous methods. Flow-through sorters are relevant to the cell loading device because it relies on them to steer and focus cells in the channel, so that cells approach the vials in a trajectory that allows the vial trap to load them properly. This chapter has been to be published as a research article in the *Journal of Micromechanics and Microengineering*.

Chapter 3 and Chapter 4 discuss the loading of cells into the vials. Chapter 3 presents the theory to treat multiple frequency dielectrophoresis. Multiple frequency dielectrophoresis is a novel way of using dielectrophoresis that has many potential applications, some of which are discussed in Chapter 3. One of the applications of multiple frequency dielectrophoresis enables cell loading, and thus multiple frequency dielectrophoresis theory has to be discussed before the vial trap is described. This section in its entirety is in the presses of the journal *Electrophoresis* to be published as a research journal article.

The description of the vial trap occurs in Chapter 4. The vial trap is the device

responsible for bringing cells flowing above the vials into them using dielectrophoresis. In this chapter I explain why multiple frequency dielectrophoresis is needed and I demonstrate cell loading through modeling and experiments. The vial traps load cells as long as their trajectory is as required by the trap, and in this chapter I show the trajectories that can be loaded by the vial trap. This chapter in its entirety will be submitted for acceptance as a research article in the journal *Lab on a Chip*.

Chapter 5 presents the design of a cell loading device. The loading device design relies on the information presented in the previous chapters. The design relies on the flow-through sorter structures described in Chapter 2 to align cells with a vial of interest and on the vial trap to bring the cell into the vial. In this chapter I discuss the characteristics of the cell loading device, its requirements, and its expected performance.

The dissertation conclusions are presented in Chapter 6. Since Chapter 2, Chapter 3, and Chapter 4 include conclusions on their own, specific to the material they cover, then it is not necessary to include conclusions on the information discussed in these chapters in Chapter 6. Instead, in Chapter 6 I present conclusions about the dissertation as a whole and about the design of the cell loading device. Finally, I summarize the scientific contributions by this dissertation.

At the end of the dissertation there are two appendices. The first one describes in detail the challenges related to patterning electrodes on top of the vial, which was necessary in the vial trap fabrication. The second is a paper that was presented at the *Life Science*

Systems and Applications Workshop that describes the cell clinics chip. This description is relevant because the cell clinics chip is mentioned throughout this dissertation, and thus this appendix can serve as a useful reference to the reader.

Chapter 2 Design of Dielectrophoretic Flow-Through Sorters Using a Figure of Merit²

2.1 Abstract

Dielectrophoretic (DEP) forces produced by a pair of electrodes are used for such applications as particle sorting in microfluidic systems. In order to allow quantitative comparison of different DEP systems, we introduce a new figure of merit: dimensionless characteristic velocity corresponding to the maximum flow that can be used while still successfully deflecting the desired particles. This avoids the necessity of performing numerical simulations in order to compare designs and allows one to focus on general system design questions. The maximum deflection velocity is evaluated versus a characteristic length for four different sorter configurations, yielding curves that can be used as tools to design DEP sorters. Maximum flow predictions are compared with previously published theoretical and experimental results.

2.2 Introduction

Advances in micro-total analysis systems (μ TASs) promise to transform the examination of biological samples. However, these lab-on-a-chip systems typically operate on

² This chapter has been submitted for review to the *Journal of Micromechanics and Microengineering* under the title “Design of dielectrophoretic flow-through sorters using a figure of merit”, by M. Urdaneta and E. Smela.

samples that have been prepared off-chip using other equipment [15]. Thus, while the μ TAS component may be portable and compact, the larger system is still tied to a laboratory. Advances in on-chip whole-sample preparation, such as separation, sorting, pre-fractionation, filtering, and concentration, are needed to integrate the entire analysis process and thereby reap the full benefits that miniaturization can offer.

Dielectrophoresis [52] (DEP) based micromanipulation technologies, such as flow-through particle sorters [49, 72, 121, 124, 134, 135, 163], particle focusers [74], particle filters [164], and other devices that trap particles against exterior forces [63, 104, 136, 143, 152], are appropriate for on-chip sample preparation for various reasons. Firstly, DEP forces are non-injurious to biological samples [108]. Furthermore, since DEP forces depend on particle volume and electrical properties, these parameters can be used as the basis for sorting [55, 72]. In addition, all the necessary hardware (waveform generator and electrodes) can be realized with integrated circuitry and combined on chip with microfluidics.

DEP flow-through sorters deflect particles in a moving fluid. They do this with a pair of electrodes at an AC frequency that exert negative DEP force, pushing on the particles to deflect them. Figure 2-1 shows an archetypal flow-through sorter geometry [49], in which one of the electrodes is on the channel ceiling (not shown) and the other is on the floor. The DEP force deflects particles from outlet 1, to which they flow by hydrodynamic drag in the absence of DEP (Figure 2-1a), to outlet 2 (Figure 2-1b). In this geometry, a successfully sorted particle does not flow over any part of the electrodes.

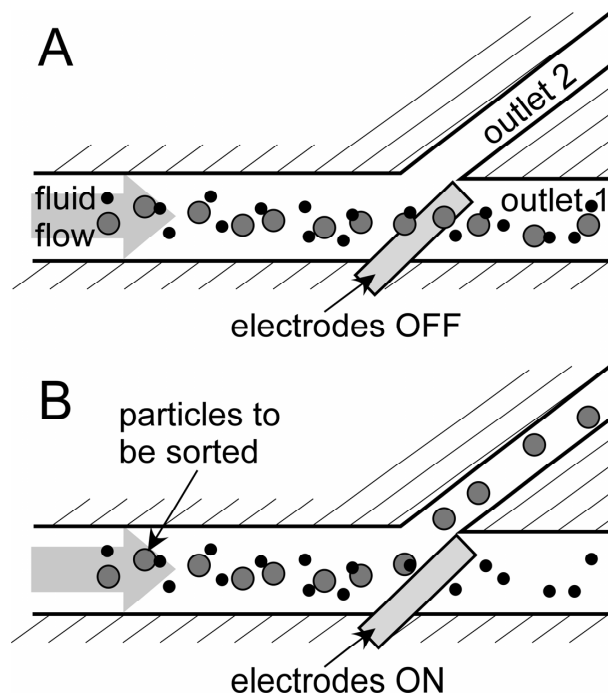


Figure 2-1. Illustration of a representative flow-through DEP sorter [49]. The electrode pair consists of one electrode on the floor of the channel and one on the ceiling. A) With the DEP force off, particles flow out of outlet 1, carried by the flow. B) When the electrodes are activated, negative DEP forces change the trajectories of the selected particles, causing them to flow to outlet 2.

In flow-through sorters, the flow velocity is the most important parameter because it determines the speed with which the device operates. This is because they sort particles serially, one particle at the time, making the sorting time per particle proportional to the flow speed. The sorting time is a critical specification when processing a large number of particles.

However, increasing flow velocities must be balanced by commensurately higher DEP forces, which are proportional to the gradient of the electric field [41, 52]. The electric field gradient distribution produced by a pair of electrodes is a function of (x,y,z) and depends sensitively on the dimensions (electrode and channel dimensions) and the electrode configuration (position and separation of the electrodes). Since it is difficult to use analytical methods to find the field gradient distribution (an example of such an analysis is presented in [165]), numerical models have been widely employed [72, 125, 166]. These models take time to prepare and require code that can couple mechanical and electrical forces. A simple method for predicting sorter operation would therefore be advantageous.

DEP flow-through sorter case studies [72, 121, 163] and papers dedicated to sorter design [49, 124, 134, 135] show that the electrode and channel geometry are two critical parameters that affect the electric field gradients. Thus, quantitative comparisons of DEP forces for particular geometries, for example as in [135], cannot be used to draw general conclusions about electrode configurations since the force values are so strongly geometry-specific. In addition, since the DEP force varies as a function of position, Nieuwenhuis and Vellekoop [135] needed to perform full 3-D particle-tracing simulations to predict device performance. One would instead like to have a simple-to-obtain figure of merit that can be used to compare designs. (Unfortunately, the peak force is not appropriate for making comparisons since it does not determine the maximum velocity, as we show below.)

In this paper, we define such a figure of merit based on the dimensionless fluid velocity. Because of its generality, the figure of merit can be used not only to compare different configurations, but also to compare DEP-based devices with other technologies, such as laser tweezers. The approach can also be applied to other devices in which a pair of electrodes manipulates particles in a fluid by means of repulsive DEP, including particle focusing and filtering. Electrode arrays, however, do not fall within the scope of this work.

The figure of merit captures all the geometric variables, and to find it we solve the dimensionless form of the governing equations. The figure of merit can be plotted against a geometric variable, generating curves that can be used as tools to design devices, regardless of their dimensions, and to estimate the maximum flow velocity they can handle. We do this with four different electrode configurations, allowing us to quantitatively compare their performance.

The figure of merit is a value found in the solution of a full numerical simulation at a specific location in the channel, and thus is as accurate at that location as any other numerical simulation. Once the figure of merit is extracted from a numerical model in the way we present, there is no need for further modeling because the figure of merit replaces the numerical solution at the given location. Further modeling is still necessary, however, if we want to find the motion of the particle elsewhere in the channel. Simulations of additional geometries would also expand the collection of figure of merit

curves presented in this paper.

2.3 Methods

2.3.1 DEP vs. Drag Forces

The particles in a sorter experience both fluid drag and DEP forces (Figure 2-2). The DEP force produced by a pair of electrodes at a voltage V on a spherical particle of radius R is [41, 52]

$$(8) \quad \vec{F}_{DEP}(x, y, z) = 2\pi CM \varepsilon (R^3) \vec{\nabla} (|\nabla V(x, y, z)|^2)$$

where CM is the real part of the Clausius-Mossotti factor [41] and ε is the fluid permittivity. This equation is valid for particles whose radius is small compared to the channel and to the electrode dimensions ($1 \mu\text{m} < R < 1000 \mu\text{m}$ [41]).

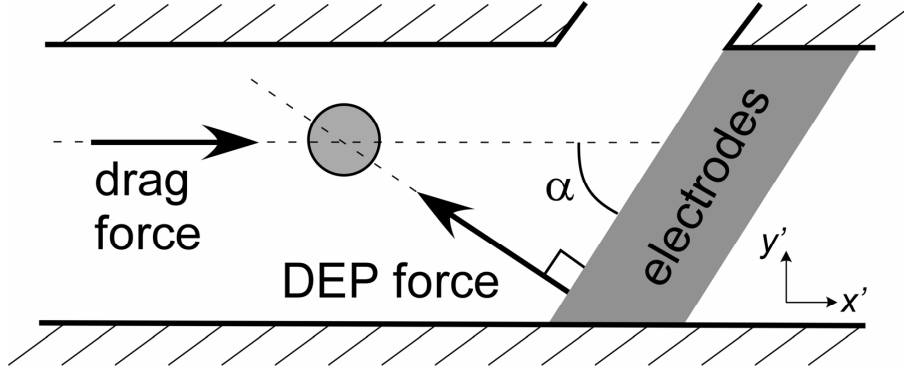


Figure 2-2. The forces acting on one of the particles in Figure 2-1. The particle moves with the fluid until it approaches the electrodes. Just upstream of the electrode, the DEP force projection on the (x',y') plane is perpendicular to the electrode edges. This causes the particle to slow down in the streamwise direction (x' -direction) and acquire a velocity component perpendicular to the channel walls (y' -direction).

The motion of the particle under the DEP force is opposed by fluid drag. The drag force, assuming laminar flow around the particle, is [167]

$$(9) \quad \vec{F}_{drag}(x, y, z) = 6\pi\eta R\vec{U}(x, y, z)$$

where η is the fluid viscosity and \vec{U} is the velocity of the particle relative to the fluid,

$$(10) \quad \vec{U} = \vec{U}_{particle} - \vec{U}_{fluid}.$$

\vec{U} is zero if the particle is moving with the flow, and equal to the fluid velocity if the particle is held completely stationary by the DEP force. When the Reynolds number is small, particle motion is dominated by viscous drag and the particle will move at the same velocity as the flow (i.e., $U_{fluid} = 0$) unless an external force (such as DEP) is

present. In general, the Reynolds number of liquids around particles small enough to be influenced by DEP is small, and therefore the particle velocity will be independent of particle size.

Notice that the fluid velocity is a local value. Using a local value in our analysis has the advantage that the results are applicable to any flow velocity profile. We do not account for velocity variations across the channel in our analysis because these variations change significantly from case to case. For example, if the fluid is produced by electroosmotic flow the velocity profile will be flat, i.e., the velocity is constant across the entire channel cross-section. On the other hand, if the flow is produced by an external pump, viscous drag will cause the velocity to drop near the walls and accelerate in the center as a well known function of channel geometry [167]. The method presented in this paper can be employed once the velocity distribution in a particular device is known, giving the local velocity that the particles experience depending on where they are in the channel cross-section.

Equating the forces,

$$(11) \quad 2\pi CM \varepsilon (R^3) \vec{\nabla} (|\nabla V|^2) = 6\pi\eta R \vec{U}$$

Equation (11) gives the velocity \vec{U} with which a particle would move under the DEP force in a stationary fluid. It can alternatively be interpreted as defining the electric field gradient required to oppose a drag force produced by a fluid of velocity \vec{U} . We will use

Equation (11) to find the maximum fluid velocity, U_{max} , that can be used in a flow-through sorter.

To make it to outlet 2 in Figure 2-1, the particles being sorted need to be prevented from flowing over the electrode. Therefore, the component of the DEP velocity \vec{U} in the x -direction, U_x , must be equal to or greater than the fluid velocity; that is, $|U_x| \geq |U_{max}|$. (Since the flow in a microchannel is laminar, the drag force produced by the incoming flow only has an x -component.) Section 2.3.4 discusses how to find the tipping point $|U_x| = |U_{max}|$.

Equation (11) shows that in some sense *one can think interchangeably in terms of force or velocity*. Since velocity is directly related to critical device specifications like sorting time, velocity is actually more appropriate than force for evaluating flow-through sorters. (Force-related parameters, such as holding force and pressure drop, may be more relevant in other applications.)

The assumptions made to reach equation (11) must be respected for the analysis that follows to be valid. Only hydraulic drag and negative dielectrophoretic forces ($CM < 0$) are considered, and fluid properties and velocity are treated as constant across the particle. The standard assumptions in the expressions for laminar flow drag (Equation (9)) [167] and dielectrophoretic forces (Equation (8)) [41, 52] also apply. Scenarios in which real devices might deviate from these assumptions include particles moving close

to the electrodes (in such cases second order terms, neglected in Equation (8), are important and result in higher DEP forces), significant Joule heating of the solution (which makes the fluid properties vary along the channel), and particles moving close to a wall in pressure-driven flow³ (because the flow velocity is not constant across the particle, creating lift and decreasing drag forces).

2.3.2 Non-Dimensionalization

The solution of equation (11) has a limitation: it only applies to devices operating under exactly the same set of conditions (same-sized particles, electrodes, and channel; same fluid viscosity; same voltage). To overcome this limitation, equation (11) needs to be non-dimensionalized [167]. The nondimensional solutions are not tied to specific channel and electrode sizes because geometries with the same *relative* dimensions will have the same *relative* solutions [167]. Non-dimensional approaches have been used before to study DEP; for example, the trapping efficiency of DEP filters was studied in terms of dimensionless time [141]. Here, we perform the non-dimensionalization in terms of velocity.

Using the parameters given in Table 2-1, equation (11) becomes

$$(12) \quad \nabla \left(\left| \nabla \vec{V}' \right|^2 \right) = \vec{U}' .$$

³ Different types of flow (e.g., electroosmotic vs. pressure-driven) have different velocity profiles across the channel.

The parameters used to non-dimensionalize each variable must be relevant to the problem. Spatial variables (x, y, z) were thus non-dimensionalized using the channel height h ⁴. The non-dimensional flow velocity U' was normalized using the characteristic dielectrophoretic velocity U_{DEP} , which is defined in Table 2-1 and was obtained by forcing it to render Equation (11) to be dimensionless after the voltage and spatial variables were non-dimensionalized.

Table 2-1. Parameters used to non-dimensionalize the variables in Equation (11) (an apostrophe indicates a non-dimensional variable).

Variable	Non-Dimensionalization Parameter		New Variable
V	V_{RMS}	root-mean-squared voltage applied	$V' = V/V_{RMS}$
w, x, y, z, h	h	channel height	$w' = w/h, x' = x/h, y' = y/h,$ $z' = z/h, h' = h/h = 1$
\vec{U}	$U_{DEP} = \frac{CM \cdot \epsilon \cdot R^2 \cdot V_{RMS}^2}{3\eta \cdot h^3}$	characteristic dielectrophoretic velocity	$\vec{U}' = \vec{U}/U_{DEP}$

⁴ When more than one parameter can be used, the choice among them is arbitrary as long as the solution correlates with variables non-dimensionalized using that parameter.

Spatial variables (x, y, z) were non-dimensionalized with both geometric parameter w (Figure 2-3) and channel height h , but the figure of merit only correlated with the spatial variables that were non-dimensionalized using h .

The dielectrophoretic velocity U_{DEP} combines all the experimental parameters (electrode voltage, Clausius-Mossotti factor, particle radius, and fluid viscosity and permittivity) into a single variable. Using larger particles, higher voltages, lower fluid viscosities, and smaller channels results in a larger U_{DEP} , which translates into higher flow velocities that can be opposed by a given geometry and configuration. All the sorter geometric dependences are combined in the dimensionless \bar{U}' . As will be shown below, this separation of experiment-specific and sorter-specific variables is expedient for designing and comparing sorter designs.

2.3.3 Numerical Solution of Model Configurations

Equation (12) was solved numerically for four different electrode configurations, illustrated in Figure 2-3. To simplify the analysis, an electrode angle of $\alpha = 90^\circ$ and symmetry along the y' axis were used to reduce the models to 2D. Changing α simply scales the magnitude of the figure of merit by $1/\sin(\alpha)$. (At 90° , particles will be trapped, suspended against the flow, and it should be noted that this is not the normal operation of flow-through sorters.)

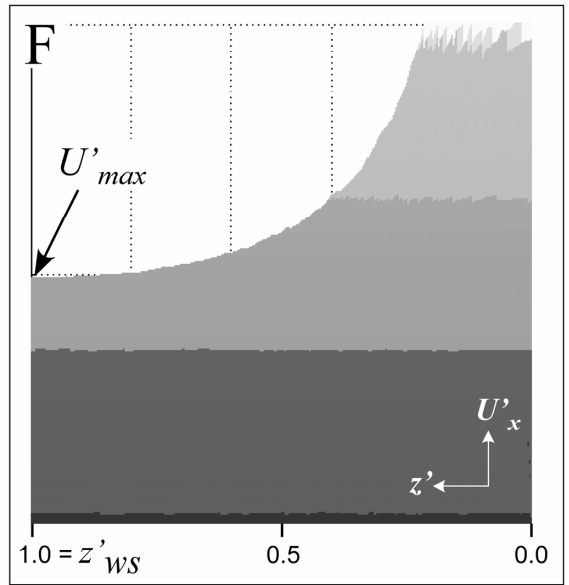
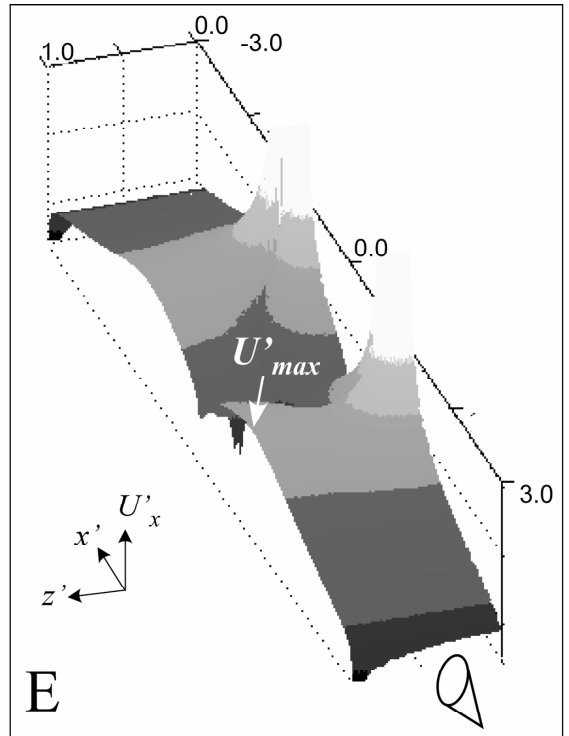
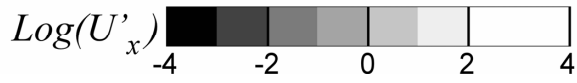
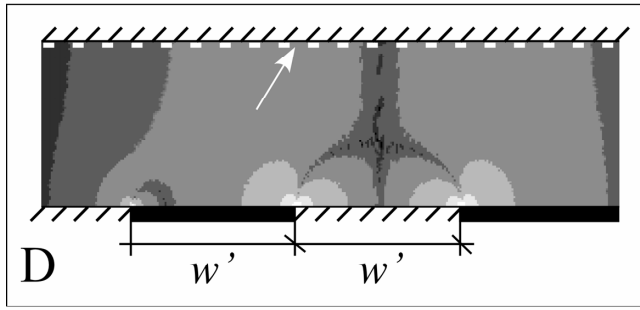
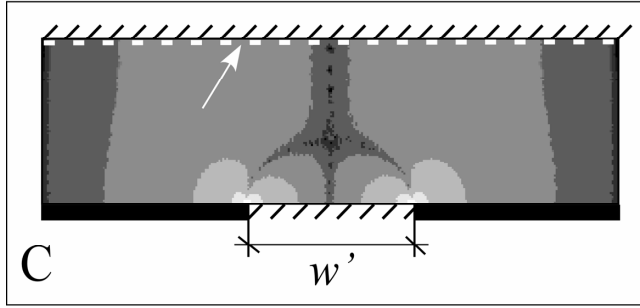
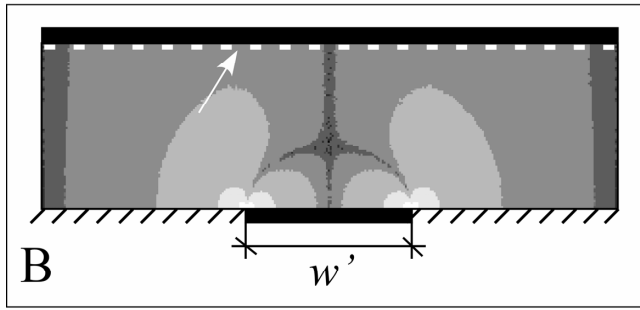
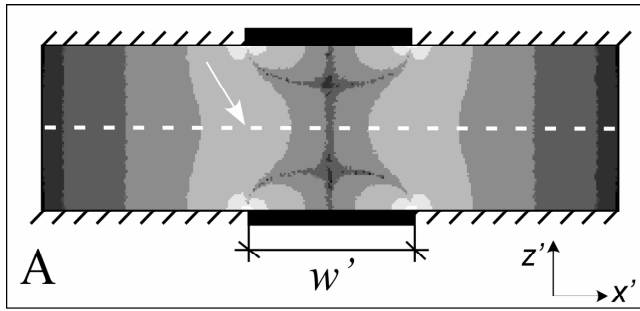


Figure 2-3. A-D) Side view illustration showing how w' defines the geometry of configurations A-D ( channel wall,  electrode). The magnitude of U'_x at each point is given by the gray-scale intensity, with lighter shades indicating higher forces. The dashed white lines show the height z' of lowest U'_x , and the arrows point to the location of U'_{max} . E) 3D plot of U'_x for configuration C. F) View looking straight down the channel, as indicated by the cone in E. This view shows, as a function of z' , the highest values of U'_x along the channel, the lowest of which is U'_{max} . The larger this number, the higher the flow speeds that can be handled by the sorter.

Configurations A [49, 72, 135], C [135], and D [135] have been presented in the literature, while configuration B is a modification of A that is easier to fabricate because it only requires patterning electrodes on one side of the channel. By definition all configurations have channel height $h'=1$ and are characterized by a single length scale, w' ; in other words, w' is the only parameter needed to describe them.

$\vec{U}'(x',z')$ was found by solving equation (12) using numerical models in Femlab 3.1 (Comsol; electromagnetics module, quasi-static, small in-plane currents). Each model was one unit tall (since $h' = h/h$). Configurations A, B, and C were $(5w' + 1)$ units wide, whereas configuration D was $(10w' + 1)$ units wide because in this configuration the location and size of the electrodes demanded a wider domain (the solution presented in Figure 2-3C was cropped to fit the figure space). One of the two regions designated as an

electrode was at electrical ground while the other was at $V'_{RMS} = 1$, and all other boundaries were electrically insulating. The meshing was automatically generated by Femlab starting with a coarse mesh and improving it through 7 adaptive meshing refinements⁵. Variations in the solution due to meshing after 7 refinements was small compared to the variations that can be expected in the experimental parameters, and thus further refinement was not warranted. (The difference in U'_{max} obtained after 6 and 7 mesh refinements was $< 2\%$.) Since the goal of this approach was to be able to characterize electrode pairs as a function of geometry, a series of models with different w' were solved for each configuration. A Matlab (MathWorks) script prepared the models, with w' varying from 0.04 to 8.0 in steps of 0.04 units, which were then solved by Femlab.

Since the fluid flow in the channel only has an x' -component, only U'_x needs to be considered. Figure 2-3 shows $U'_x(x',z')$ for configurations A - D with $w' = 1$. Values of U'_x are highest at the electrode edges, and they drop as a function of x' , z' differently in each configuration. (The dashed lines and arrows will be used in section 2.3.4 in obtaining the figure of merit.)

⁵ Adaptive meshing is a Femlab feature that automatically refines the mesh close to the electrodes, where the solution changes rapidly.

2.3.4 Figure of Merit U'_{max}

Given the different distributions of $U'_x(x',z')$ in Figure 2-3, the question arises, how can different configurations be compared? The force should not be evaluated at a fixed point relative to the electrodes because of the changes in force distribution with configuration and geometry. We therefore use the flow velocity above which particles start to pass over the electrodes, which has been used previously to describe sorter performance [49, 134, 135], though not in its dimensionless form. This figure of merit will be called the *maximum deflection velocity* U'_{max} . At flow velocities higher than U'_{max} , some of the particles will find their way past the electrodes and will not be sorted. This bottom-line descriptor can be used to directly compare different configurations because it is not anchored to a particular location in the channel. While the position of U'_{max} depends on the system geometry, there will always be a flow speed at which the drag force first overwhelms the DEP force somewhere in the channel, and this is the flow speed of most interest. This definition of U'_{max} is sufficiently general to allow comparison with configurations not considered in this article, as well as devices based on other physical phenomena.

U'_{max} will be value of U'_x at the "weak spot" of the sorter, located at (x'_{ws}, z'_{ws}) . As a rule of thumb, this point is at the height z'_{ws} in the channel that is furthest from any electrode edges since the DEP force is smallest there. This height is therefore at the center of the channel in configuration A and at the top of the channel in configurations B-D, shown by the dashed white lines in Figure 2-3. (This was confirmed by simulation results for

values of w' between 0.04 and 8.)

The position of the weak spot along x' also needs to be determined. The position x'_{ws} is where U'_x is a maximum along z'_{ws} . To understand this, consider Figure 2-3E, which shows a surface plot of U'_x for configuration C. Figure 2-3F shows the same plot from the point of view indicated by the cone in Figure 2-3E; from this perspective one sees, as a function of z' , only the maximum values of U'_x along the channel. Any particle with a velocity greater than the highest U'_x along its trajectory will go past the electrodes, and the sorter will fail: U'_{max} is the lowest hurdle that needs to be overcome for any particles to pass the electrodes.

When the flow velocity matches the dielectrophoretic velocity, if $\alpha = 90^\circ$ the particle will be suspended, trapped against the flow. If $\alpha \neq 90^\circ$, the particle will be deflected for all $|U'_x| \leq |U'_{max}|$ to outlet 2 in Figure 2-1. If the flow velocity exceeds U'_{max} , the sorter will fail, which is why (x'_{ws}, z'_{ws}) is called the weak spot. (Since the DEP force pushes particles flowing down the channel towards the dashed white line, there will actually be a high concentration of particles there.)

The position of x'_{ws} depends on the electrode configuration. These points were determined by solving for the field gradients and using a Matlab routine to find the maximum value of $U'_x(x')$ at z'_{ws} for each value of w' .

2.4 Results and Discussion

2.4.1 Dependence of Sorter Performance on Configuration and Geometry

Turning now to using this metric for device design, one can determine how sorter performance depends on electrode size/spacing. Figure 2-4 shows U'_{max} as a function of w' for configurations A-D⁶. The highest value of U'_{max} ($U'_{max} = 1.6$) is found for configuration A, showing that the fabrication effort involved in patterning electrodes on two substrates and aligning them across the channel is rewarded. This is not unexpected, since z_{ws}' is closer to the electrode edges in A than in B-D, so the DEP force, which scales as $1/\text{distance}^3$, is stronger. The dependence of U'_{max} of configuration A on w' agrees with published numerical models [124]. This is followed by configuration B ($U'_{max} = 0.8$), which has a maximum U'_{max} that is half that of configuration A, but outperforms configurations C and D, which have peak U'_{max} values that are comparable to each other ($U'_{max} = 0.25$ and 0.26). Placing the electrodes across from each other extends the force further across the channel (compare regions with $U'_x \sim 10^0$ for configurations B and D in Figure 2-3). The same behavior was also predicted by the models presented in [135].

⁶ Numerical models were solved for w' up to 8, but we only show results for $w' < 4$ to highlight the regions in which U'_{max} varies significantly.

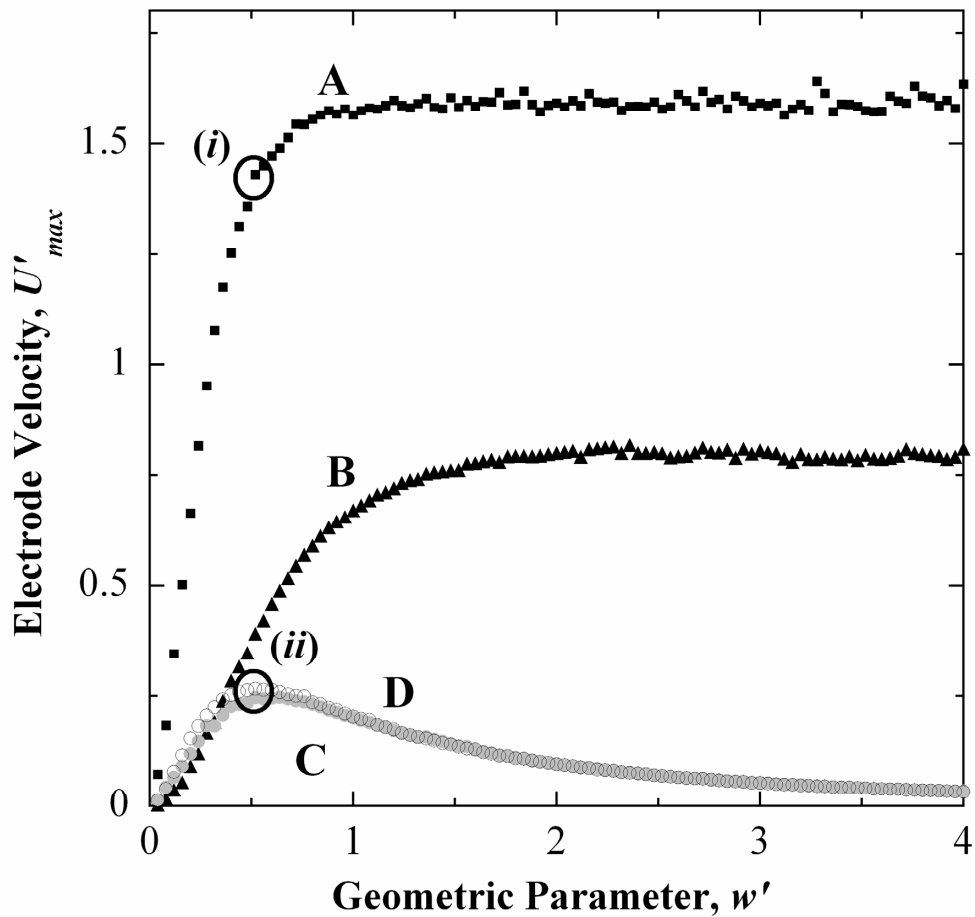


Figure 2-4. The non-dimensional figure of merit U'_{max} as a function of w' for electrode configurations A (■), B (▲), C (●), and D (○).

Configurations C and D have peaks in U'_{max} (at $w' = 0.6$ and 0.5 , respectively), unlike A and B. The latter two have a constant electrode separation h' , and increasing the electrode width increases the DEP force up to a certain point ($w' = 1$ in A and $w' = 2$ in B), after which further increases have no effect, since it is the electrode edges that are of most significance. However, in C and D, increases in w' also increase the electrode separation, which reduces the DEP force.

Curves such as those in Figure 2-4 are tools that can be used to examine design tradeoffs. While we only illustrate the results for cases A-D, such curves could be used, for example, to investigate the effect of increasing the electrode width in geometries C and D while holding electrode separation constant.

These curves can also be used to find the maximum flow velocity U_{max} by multiplying the dimensionless U'_{max} by U_{DEP} . To illustrate how this is done we consider design *i* of configuration A and design *ii* of configuration D acting on particles of $R = 1.3 \mu\text{m}$ and $CM = -0.5$ in water ($\epsilon = 80 * \epsilon_o$, $\eta = 0.001 \text{ N-s/m}^2$) with $\alpha = 90^\circ$ and $h = 25 \mu\text{m}$. Design *i* has the U'_{max} labeled point (*i*) in Figure 2-4, and for an applied voltage $V_{RMS} = 7.5 \text{ V}$ it has a $U_{DEP} = 718 \mu\text{m/s}$, and thus an $U_{max} \sim 1000 \mu\text{m/s}$. Design *ii* has a lower U'_{max} , point (*ii*) in Figure 2-4, and thus this design requires a $V_{RMS} = 17.5 \text{ V}$ for it function at the same flow velocity.

2.4.2 Model Validation

To validate this method, we started by comparing its predictions with results from two particle-tracing numerical simulations by Nieuwenhuis et al. [134, 135] (These were the only reports that had included sufficient detail to allow comparison.) The model parameters were taken from the values given in the papers (voltage, particle size, fluid, channel height), extracted from images in the papers (electrode angle, electrode width), and assumed (temperature 25°C , Clausius-Mossotti factor -0.5). The flow in those

simulations was pressure driven, and the reported velocity was the highest bulk velocity before the particles started to cross over the electrodes. It is well known that fully-developed pressure driven flow has a parabolic velocity profile across the channel [167], and that the peak velocity in the middle of the channel is 1.7 times the average channel velocity. To compare the experiments with our predictions we multiplied the reported bulk velocity by 1.7 to obtain the local velocity in the middle of the channel⁷ [134, 167], since the electrodes in all three simulations were of configuration A. In the first simulation [134], $w' = 0.28$, and the maximum flow velocity we predicted agreed of that obtained using their published 3D particle tracing results. In the second case w' was infinitely long [135] (there is little change in U'_{max} for $w' > 1$, so we used the asymptotic value of U'_{max}), and we found agreement in this case as well. Agreement with published numerical models is not surprising, since U'_{max} is also the solution of numerical models.

In terms of experimental validation, there were two studies that provided sufficient information to allow comparison, both with configuration A. Durr et al. [49] measured the velocity at which particles began to flow past the electrodes using particle imaging velocimetry; since this represented the local velocity, no correction was needed for comparison. We compared our predictions to those experiments in which the particles were small compared to the channel height ($R = 21 \mu\text{m}$ and $h = 50 \mu\text{m}$). Our predictions were between 90% and 150% of the experimental values given in ref. [49], and when

⁷ The advantage of using the local fluid velocity in our analysis is that different types of flow and particle locations can be addressed simply by using different correction factors.

compared to the experimental flow velocity at which the particles “penetrate the dielectrophoretic barrier” in ref. [134], our prediction was only 18% higher. Note that full 3D particle-tracing simulation results given in the same paper, which were discussed in the previous paragraph, also overestimated the flow velocity by *the same amount* [134].

The maximum flow velocity that can be used in a channel is highly sensitive to variables such as voltage, viscosity, and particle radius, all of which are known within a given uncertainty (and some of which are difficult to measure experimentally). We believe that the experimental uncertainties are responsible for the discrepancies between modeling and experimental results, discrepancies that are also present in the literature on the subject [49, 134]. Therefore, we must understand that the values predicted using the method presented are as good as can be predicted using elaborate modeling methods, and this solution that can be found with astonishing ease compared to detailed models, but they may show discrepancies with experimental results. Despite these uncertainties, the figure of merit is a valuable design tool since it correctly predicts the relative performance of each design and the dependence of the performance on different design and experimental parameters.

As mentioned previously, the usefulness of a figure of merit is that it gives one the capability of comparing devices that work differently, thus allowing comparisons with other technologies. For instance, $U_{max} = 1000 \mu\text{m/s}$ for design (*i*) is the same as the flow speed against which laser tweezers with 15 W of power can hold a particle [168].

2.4.3 Discussion

The use of velocity to characterize the performance of flow-through sorters is advantageous in part because it can be easily converted into other parameters. For example, since the volumetric flow rate is proportional to the flow velocity and channel cross-sectional area, volumetric throughput can be optimized using the presented method. The effect of channel height can be obtained using U_{DEP} and Figure 2-4, and the effect of channel width can be obtained through channel cross-sectional area, thus enabling volumetric throughput analysis. The workload is eased through this method because a designer would be able to compare the effects of channel height and width separately without having to model various channel dimensions. Likewise, if the designer is interested in force values, then they can be found from velocity values through Equation (9).

Including all geometric dependences in the figure of merit U'_{max} blurs details for the sake of convenience, rendering DEP electrode pairs as off-the-shelf parts that can be used with little knowledge of how they work. It is true, however, that reducing such a complex problem to a single number comes at the expense of oversimplification. In calculating U'_{max} we conservatively considered the worst-case scenario of particles moving at the height of lowest streamwise force. Particles flowing closer to the electrodes experience larger forces and could therefore be sorted at higher flow speeds.

The dielectrophoretic velocity U_{DEP} includes the effect of all the experimental parameters on the performance. For example, since $U_{DEP} \sim R^2$, a lower flow velocity must be used with smaller particles; this is a fact that Schnelle et al. [72] used to separate particles of different size. Joule heating affects U_{DEP} by decreasing the viscosity, $U_{DEP} \sim \eta^{-1}$, which increases the allowed flow velocity. U_{DEP} can also be examined to trade off costs and benefits. Integrated circuits operate at relatively low voltages (3 – 5 V), imposing a limit for systems integrated with such circuits. Since $U_{max} \sim V^2$, this loss in DEP force could be compensated by decreasing the channel height, which increases U_{max} as h^{-3} .

It is important to note that the parameters that determine U_{DEP} are subject to uncertainty and variations. Particle radius may vary, especially in cells. The fluid viscosity is exponentially dependent on the fluid temperature [167], which in turn varies with flow rate, fluid conductivity, electrode voltage, and electrode and channel geometry. These variations may lead to significant performance uncertainty: given uncertainties of 5% each in the voltage, particle radius, fluid viscosity, channel height, and Clausius-Mossotti factor, the uncertainty for the characteristic dielectrophoretic velocity is 20%⁸.

⁸ If the variations are truly random, the total uncertainty is obtained by taking the derivative of each variable, multiplying it by the uncertainty, dividing it by the original function (for normalization), and then taking the square root of the sum of the squares of that number for each variable [169] Figliola, R.S., and D.E. Beasley, Theory and Design for Mechanical Measurements. 3rd ed. 2000, New York: John Wiley & Sons, Inc..

2.5 Conclusions

Combining figure of merit curves with U_{DEP} offers a quick estimate of the performance of DEP-based devices, providing a way to balance the benefits and costs of different electrode configurations and to compare different devices with each other or with other technologies. Once a curve of U'_{max} such as in Figure 2-4 has been generated for a given design (which does require simulations to create), it is thereafter unnecessary to run detailed numerical models of multiple design options. The designer can then focus on more complex issues: does the lower voltage enabled by using design i outweigh the relative ease of fabricating ii ? To what extent will variations in particle size limit the allowable flow velocity? What dimensional tolerances can be accepted, and how will this affect fabrication costs? This method should be particularly useful when designing a complex microsystem, when compact models are required to estimate the cost and benefits of changing variables that have broad effects throughout the system (e.g., fabrication method, channel height).

Based on the four electrode configurations that were quantitatively compared, we can conclude that, all other variables remaining equal, configurations in which the electrodes are across the channel from each other produce higher DEP forces than configurations in which the electrodes are in the same plane. While configurations with constant electrode spacing (A and B) produce forces that increase with geometric parameter w' before reaching a constant value, the forces in configurations with varying electrode spacing (C and D) reach a peak value before decreasing with w' . This information can be used to

optimize and minimize device size.

We only obtained U'_{max} for four electrode configurations in this work, but we envision a library of electrode configuration performance curves that can be used to estimate device performance. This library would be analogous to curves of drag coefficients for different bodies such as are used in fluid mechanics [170].

Chapter 3 Multiple Frequency Dielectrophoresis⁹

3.1 Abstract

A novel method of modeling multiple frequency dielectrophoresis (MFDEP) is introduced based on the concept of an effective Clausius-Mossotti factor, CM_{eff} , for a particle that is exposed to electrical fields of different frequencies, coming either from one or multiple pairs of electrodes. This analysis clearly illustrates how adding frequencies adds control parameters, up to two additional parameters per frequency. As a result, MFDEP can be used for a wide variety of applications, including separating particles with very similar Clausius-Mossotti spectra, trapping multiple groups of cells simultaneously, and cancelling unwanted dielectrophoretic traps. Illustrating the modeling approach, we determine the CM_{eff} s for live and dead yeast cells, and then predict their equilibrium distribution on a 3-electrode configuration, with two electrodes at different frequencies and the third electrode at ground. This prediction is validated experimentally, using MFDEP to selectively attract live cells to one location and dead cells to another, trapping both. These results demonstrate that the use of multiple frequencies for the manipulation of particles can enhance the performance of dielectrophoretic devices, not only for sorting, but also for such applications as patterning cells in close proximity for the formation of cell consortia.

⁹ This chapter will be published in the issue 18 (2007), of the journal *Electrophoresis*, under the title “Multiple frequency dielectrophoresis”, by M. Urdaneta and E. Smela.

3.2 Introduction

The manipulation of particles, from nanoparticles to cells, using electric fields has gained increasing importance with the development of miniaturized, lab-on-a-chip type devices. Dielectrophoresis (DEP) is one such method, exerting forces on particles via dipoles that are induced by electric field gradients [41, 51, 55, 171-173]. One attractive feature of DEP is that it allows particle sorting, isolation, and other manipulations without the need for tagging the particles (e.g. with fluorescent markers); rather, the electrical characteristics of the particle itself are used for the separations. Not only can cells be sorted by type, but also by size and even by stage in the cell cycle [55, 72].

DEP forces can be either attractive (positive DEP, pDEP) or repulsive (negative DEP, nDEP). The sign of the force is given by the real part of the frequency-dependent Clausius-Mossotti factor, $\text{Re}(f_{CM}) = CM$. The Clausius-Mossotti factor reflects the relative polarizability of the particle and the medium and is given by a normalized difference in their complex permittivities:

$$(13) \quad f_{CM} = \frac{\epsilon_p^* - \epsilon_m^*}{\epsilon_p^* + 2\epsilon_m^*},$$

where the subscripts refer to the particle and the medium and ϵ^* is the complex permittivity. Because they depend on field gradients, DEP forces decrease with the cube of the distance from the electrodes.

In a mixture of different types of particles, if one type experiences positive DEP and the

others negative DEP at a particular frequency [55, 94, 95, 112], the particles can be separated into two groups. The first is attracted to the electrodes (specifically, to their edges, where the electric field has maximum intensity) and trapped there, while the others are repelled and can be removed by subjecting them to fluid flow or other forces.

The dielectrophoretic force \vec{F} that an electric field \vec{E} at a single frequency exerts on a particle is given by

$$(14) \quad F = A * V * \epsilon * CM * \frac{\nabla |\vec{E}|^2}{2} = k * CM * \nabla |\vec{E}|^2$$

where A is a geometric factor (for a sphere $A = 3$), V is the volume of the particle, ϵ is the permittivity of the medium [41, 52], and k is a constant for a given particle/medium system. For a sphere, CM has a minimum value of -0.5 and a maximum of +1 (the numbers can be larger for an ellipsoid [41]).

The value of CM lies in the fact that it contains the frequency dependence of a particle's behavior (Figure 3-1A); for a given spatial position, k and $\nabla |E|^2$ only change the magnitude and direction of the effect (Figure 3-1B). Specifically, the sign of CM determines whether a particle experiences pDEP or nDEP, which changes at a particular cross-over frequency, ν_{cf} . For live cells, for example, CM is usually negative at low frequency and positive at high frequency. On the other hand, for dead cells it can be quite different. It is the differences in their CM spectra that allow particles to be separated.

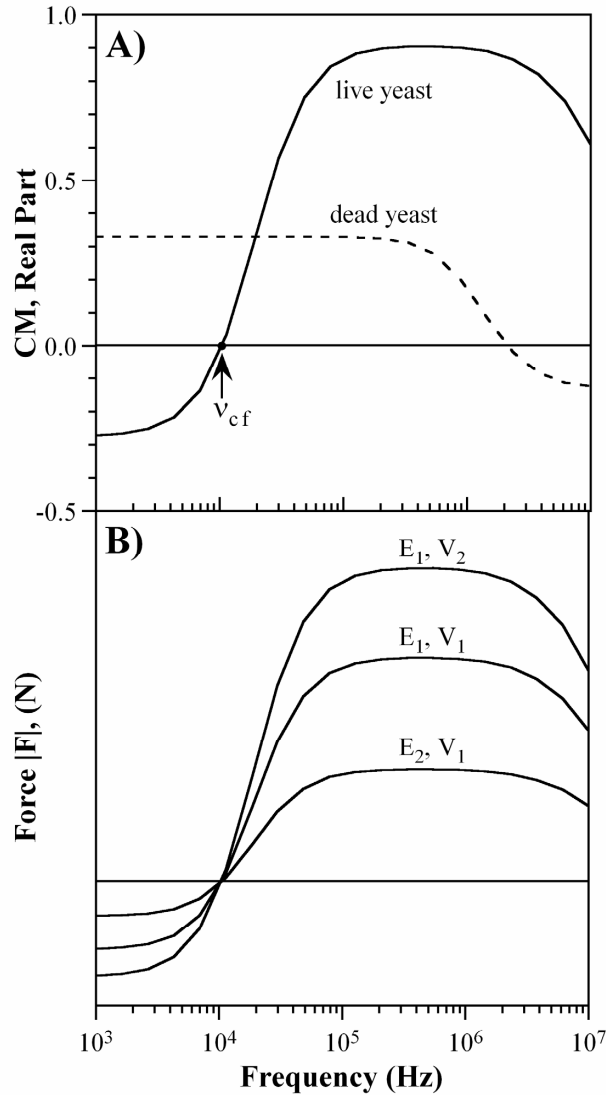


Figure 3-1. A) Real part of the Clausius-Mossotti factors for live and dead yeast as a function of frequency, found as described in section 3.3.2. B) Schematic illustration of how the force on a live yeast cell at a given position can change with particle volume (V_1 vs. V_2) electric field strength and gradient (\vec{E}_1 vs. \vec{E}_2).

Most prior work on DEP has employed only one frequency [6, 51, 55, 58, 72, 76, 94, 95, 112, 113, 171-173]. Although some work has been done with multiple frequencies [70,

85, 97, 100, 101, 145, 154, 155, 174], there has not been a general discussion of how to treat this theoretically. Two frequencies were first used by Arnold et al. [70] to null DEP forces and thereby obtain accurate electro-rotational spectra. In 1992 Kaler et al. [101] pointed out that under two frequencies applied simultaneously, the total force on a particle can be determined by adding the force due to each separately. They experimentally demonstrated simultaneous nDEP and pDEP from a single pair of electrodes, dielectrophoretically levitating cells with pDEP at high frequency while at the same time subjecting them to low frequencies in order to obtain the low-frequency *CM* curve. In 2003, this concept was taken up again, in three papers. Pethig et al. [174] made use of the sum of forces, showing that by adding a DEP signal or a second traveling wave DEP (TWDEP) signal to a first TWDEP signal, the range of frequencies over which TWDEP can operate is extended. Furthermore, one type of particle can be trapped while a second is moved away by TWDEP, and with the right frequencies and field strengths, two types of particles can be made to move in opposite directions. Experimentally, cells were separated within 1/5th the distance than could be achieved with a single frequency. In addition, that year a theoretical analysis of multiple frequency DEP was presented in terms of Laplace transforms and transfer functions [154]. It was shown that the frequency range for particle separation with DEP could also be increased by combining two frequencies. Finally, using that fact, two-frequency DEP was employed to separate latex beads with similar Clausius-Mossotti curves [155]. More recently, in 2005, Aldeus et al. [145] calculated the total forces on *E. coli* due to fluid drag and two DEP frequencies, and from that computed cell trajectories in a microchannel with pDEP electrodes on the bottom and nDEP on the top. The fraction of *E. coli* collected on the

bottom electrodes was predicted to be significantly greater than with pDEP alone because the cells would be pushed downward by the nDEP forces, closer to the bottom electrodes.

Despite this work, the full utility of multiple frequency dielectrophoresis (MFDEP) has not yet been explored. This paper presents a straightforward, general framework for modeling and utilizing MFDEP, based on defining an effective Clausius-Mossotti factor. The many advantages and potential applications of using multiple frequencies to generate more complex DEP forces then become more clearly evident. This is illustrated with particle sorting, one of the most common applications of DEP. For example, we show that by using two frequencies, one can simultaneously trap two types of cells.

Furthermore, as has been recognized, there is sometimes no single frequency at which the particles one wishes to separate have opposite DEP signs, but as long as there are any differences in their Clausius-Mossotti factors, there is a combination of frequencies and amplitudes that produces opposite DEP signs, and we show a method for finding it. The model predictions are validated experimentally by trapping two groups of cells in different locations using a 3-electrode configuration.

3.3 Modeling

We start by using the DEP governing equation to determine how to properly add the effects of n superimposed frequencies. With the objective of using this result to predict the experimental results reported in Section 3.4, we next obtain the CMs for live and dead yeast cells as a function of frequency, and from that their CM_{eff} under two frequencies

simultaneously. The results in this example lead to a discussion of how to systematically engineer particle separation.

3.3.1 Dielectrophoretic Force at Multiple Frequencies

To find the time-average forces due to multiple frequencies f_i , as has been previously noted and as we show in the Appendix, one can add the forces due to each one alone, even though the DEP governing equation (equation (15)) is nonlinear. Another approach is to define an effective Clausius-Mossotti factor CM_{eff} to be used with the total electric field (equation (20) in the Appendix) \vec{E}_{total} so that

$$(15) \quad \vec{F} = k * CM_{eff} * \nabla |\vec{E}_{total}|^2.$$

This approach is better because it preserves the formalism that has been widely used in the DEP community, allowing one to generate curves equivalent to those of CM vs. frequency, bounded by the same limits. CM_{eff} will contain the relevant frequency information for utilizing MFDEP, since its shape determines the important parameters from superposing multiple frequencies on a particle: the sign of the force and the cross-over frequency. Like CM , CM_{eff} is unitless. Once the system has been designed to achieve the desired sorting, trapping, parasitic trap cancellation, etc. by using CM_{eff} to choose appropriate frequencies, then the forces $\vec{F}(x, y, z)$ on each type of particle at every point in space can be obtained to give particle velocities and other information of interest.

This approach leads to (following the derivation in the Appendix)

$$(16) \quad \underline{CM}_{eff} = \frac{\sum_i^n CM_i \nabla |E_i|^2}{\sum_i^n \nabla |E_i|^2},$$

where the underline indicates a time average, E_i is the root mean square electric field at frequency f_i , and CM_i is the CM at frequency f_i . Thus, CM_{eff} is a weighted average of the CM_i , with the weighting determined by the gradient of the squares of the field magnitudes. Thus, unlike the CM_i , $CM_{eff}(x,y,z)$ depends on position as well as frequency. Equation (16) illustrates how control parameters are added with each added frequency. While the Clausius-Mossotti factor is only a function of the frequency, CM_{eff} is a function of both the frequency and the field gradients at each frequency.

Although CM_{eff} can be seen as a position-dependent normalization of the force, conceptually linking this parameter to the Clausius-Mossotti factor is advantageous because it contains the frequency response and can replace the Clausius-Mossotti factor directly in the DEP force equation (compare equations (14) and (15)). Conveniently, CM_{eff} reduces to CM when only one frequency is present. Thus, while CM describes the relative polarization due to a single frequency, CM_{eff} gives the polarization resulting from all the frequencies.

Equation (16) is valid for any number of electrodes and any number of frequencies

applied on those electrodes. In some of the special cases examined below in which two frequencies are applied to the same pair of electrodes, the equation simplifies. However, no assumptions need to be made to employ equation (16).

3.3.2 CM_{eff} for Yeast Cells

Yeast cells were used in this study because they are a well understood model for DEP experiments, and because live and dead yeast cells, while having the same size, have very different CM response. To obtain the Clausius-Mossotti factors for live and dead yeast cells, they were modeled as multi-layered spherical shells in a uniform field with Ohmic loss following Appendix C of Jones [41]. The effective electrical properties of the entire structure were found iteratively: the conductivity and dielectric constant of an inner sphere surrounded by the adjacent layer were calculated so that they could in turn be treated as a single sphere in the next calculation with the next adjacent layer. The effective properties for each sphere were calculated at every frequency using Matlab (MathWorks)¹⁰. Parameters for the model were obtained from [84] (Table 3-1) and the experimentally measured solution conductivity.

¹⁰ The Matlab code used to calculate CM , using multiple-shell and single-shell models, and CM_{eff} are available upon request.

Table 3-1. Parameters used to predict the Clausius-Mossotti factors CM of viable and non-viable yeast cells. Parameters taken from [84] or measured (*).

	Viable	Non-Viable
Interior conductivity (S/m)	0.2	7×10^{-3}
Interior dielectric constant	50	50
Cell diameter (μm)	8	7
Membrane conductivity (S/m)	25×10^{-8}	16×10^{-5}
Membrane dielectric constant	6	6
Membrane thickness (nm)	8	8
Wall conductivity (S/m)	14×10^{-3}	15×10^{-4}
Wall dielectric constant	60	60
Wall thickness (nm)	220	250
Medium dielectric constant	78	78
Medium conductivity*	2.8×10^{-3}	2.8×10^{-3}

The resulting frequency responses are shown in Figure 3-1. The live cells undergo negative DEP until a frequency of 10 kHz, at which the CM changes sign to positive DEP and the cells become attracted to the electrodes. The dead yeast, on the other hand, experiences positive DEP at low frequencies, changing to negative DEP at 2 MHz.

To illustrate the CM_{eff} resulting from two frequencies in the simplest possible

configuration, Figure 3-2 shows the effect of using dual frequencies on a single pair of electrodes. In this special case only, equation (16) reduces to

$$(17) \quad \underline{CM}_{eff} = \frac{CM_1 |\underline{E}_1|^2 + CM_2 |\underline{E}_2|^2}{|\underline{E}_1|^2 + |\underline{E}_2|^2}.$$

because the fields have exactly the same variation.

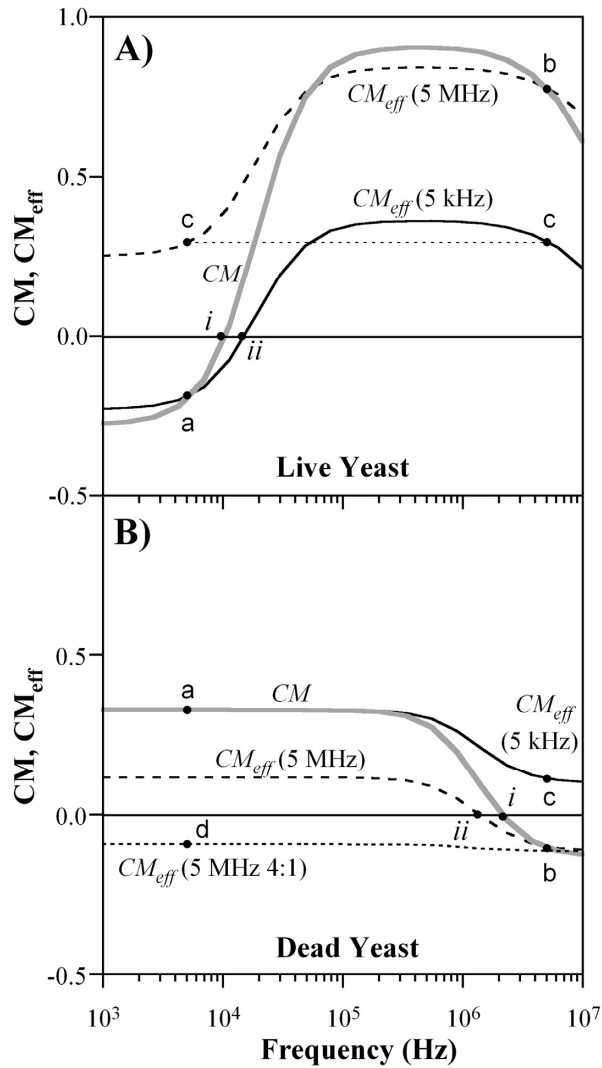


Figure 3-2. The CM_{eff} obtained from the two-shell model as a function of frequency for A) live and B) dead yeast that result from superposing onto the x-axis frequency a 5 kHz (solid line) or 5 MHz (dashed line) signal of equal magnitude. The real part of the Clausius-Mossotti factors (thick gray lines) are shown for comparison. The points *a*, *b*, and *c* correspond to areas in Figure 3-5, and the points *i* and *ii* are the original and altered cross-over points.

The CM spectra (gray lines) are included in Figure 3-2 so the effects of added frequencies are clearly evident. The solid black line is the CM_{eff} as a function of frequency if, in addition to the frequency on the x -axis, a 5 kHz signal of equal magnitude is superimposed on the electrodes. The live yeast curve, negative at 5 kHz, is lowered at high frequencies by the superposed signal, from point b to point c , but not enough to change its sign (Figure 3-2a). (Point c can be represented equivalently on either the 5 kHz or 5 MHz curves, since it is the superposition of these two frequencies.) Thus, the magnitude of the attraction to the electrode is reduced, by approximately 60%, but the cells are still attracted. Note, however, that the crossover frequency is shifted from point i to point ii , which is of utility, as discussed below. The addition of the 5 kHz signal to the dead yeast curve (Figure 3-2b) results in a CM_{eff} that is *positive at all frequencies*. The curve at high frequencies is raised by the addition of the low frequency signal (at which the cells experience positive DEP), with the change being sufficient to switch the sign of their response to negative DEP in going from point b to point c .

The curve shown as a dashed black line is the CM_{eff} resulting from a 5 MHz signal superimposed over the frequency on the x -axis. This raises the curve at low frequency for live yeast, making it positive at all frequencies (moving point a to c). It lowers the curve for the dead yeast cells at low frequency, but it remains overall positive, just as in the absence of the 5 MHz signal, until the 2nd frequency reaches 2 MHz. Again, the cross-over frequency is shifted.

The dotted black curve in Figure 3-2B shows CM_{eff} if the 5 MHz signal is a 4x larger than the frequency on the x -axis. This has the effect of lowering CM_{eff} to the 5 MHz response everywhere. The larger amplitude 5 MHz signal overwhelms the 2nd frequency component, so that the particle is unaffected by it.

3.3.3 Particle Separation

It is convenient to separate particles using a frequency that results in CMs of opposite sign for each particle type because this way one type is retained at a specific location while the other is repelled and can be washed off. For this purpose, it is necessary that the CM crossover frequencies for each type are different. Since there are uncertainties in the calculated crossover frequencies (due primarily to variations in medium conductivity, particle size, and applied frequency), it is desirable that the difference between the crossover frequencies is as large as possible.

Live and dead yeast cells have a large range of frequencies over which their CMs have opposite sign. This is not, however, typically the case. Since the addition of another frequency offsets and scales CM_{eff} (Figure 3-2), one can use multiple frequencies to make the response of particles with very similar CM spectra more dissimilar. It is almost always possible to find a combination of frequencies and amplitudes that gives two groups of particles a CM_{eff} with opposite sign. For this to happen it is only required that both groups have both positive and negative CM and that these curves be non-identical over at least some narrow range of frequencies. When using MFDEP, the crossover

frequency requirements for successful separation are therefore relaxed.

To illustrate how such separation would take place, consider the CM versus frequency plot for human T- and B-lymphocytes shown in Figure 3-3. The CM values were calculated using the single shell model in a uniform field [90], using the parameters given in [89]. The window for separating these cells using one frequency is small (range a), but when a 10 kHz signal of relative amplitude 0.6 is added to the original signal, the two CM_{eff} take on different signs over a larger frequency range (range b). In other words, the force component resulting from the fixed 10 kHz signal is used to offset the net force on the particle due to the other frequency, thus enabling one to manipulate the crossover frequencies. Any difference in the CM response of the particles can be exploited, even if the CMs have the same sign, and the larger the difference in the CM responses, the larger the separation region between crossover frequencies that can be created.

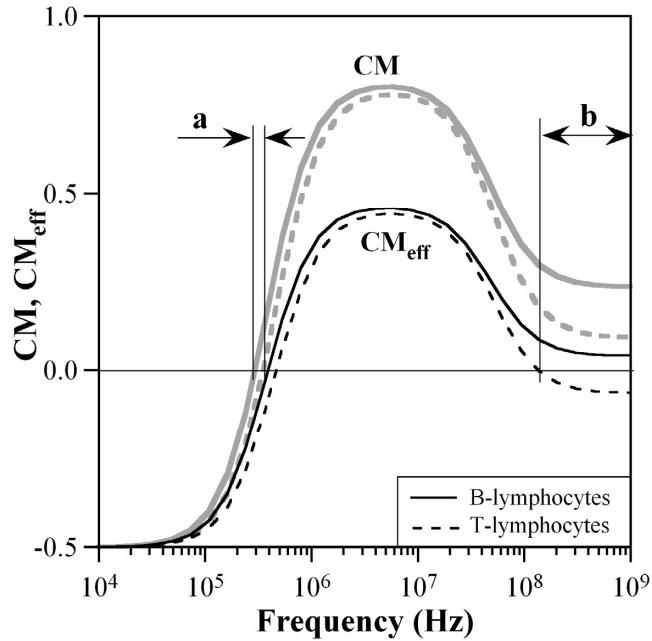


Figure 3-3. CM spectra (gray lines) for human T- and B-lymphocytes as a function of frequency, and their CM_{eff} (black lines) when a 10 kHz signal of relative amplitude 0.6 is added to the original frequency. The range for separation is shifted and widened from a to b .

To find these optimal frequencies and amplitudes, it is helpful to plot CM_{eff} as a function of the two frequencies and their relative amplitudes. Figure 3-4 shows the sign of the product of the CM_{eff} s for T- and B-lymphocytes for signals on a single pair of electrodes with two frequencies, f_1 and f_2 , and various relative amplitudes, $|E_2|/|E_1|$. The regions in white are those at which the CM_{eff} have the same sign, while those in black show the separation regions where the CM_{eff} have opposite sign.

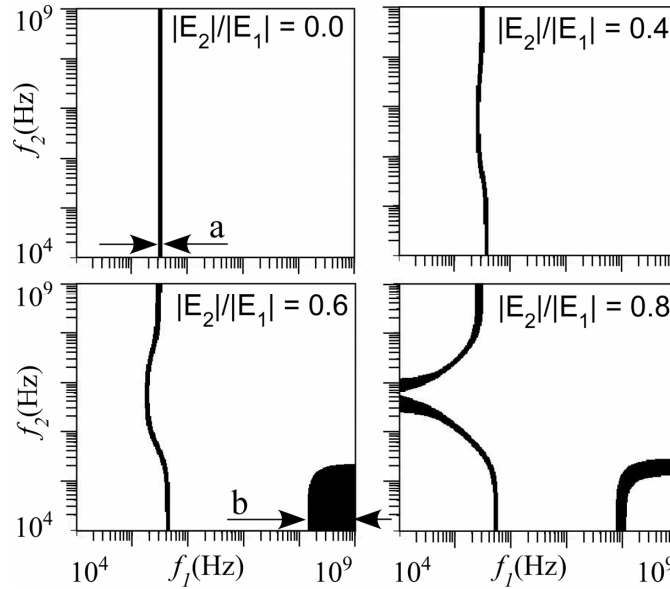


Figure 3-4. Sign of the product of CM_{effs} for T- and B- lymphocytes under two frequencies f_1 (x-axis) and f_2 (y-axis) at four amplitudes $|E_2|/|E_1|$. Regions in which the CM_{effs} are the same are shown in white and regions in which the CM_{effs} are different (i.e., the frequency ranges in which the particles can be readily separated) are shown in black.

When the relative amplitude $|E_2|/|E_1| = 0$, only the frequency f_1 is applied and the separation region is small. (This is the range labeled (a) in Figure 3-3.) At $|E_2|/|E_1| = 0.4$, the second frequency starts to affect the cells, and the separation region becomes a function of f_1 and f_2 , but the contribution from f_2 is not yet significant: although the separation region now spans a wide range of f_2 , it still spans only a small range of f_1 . At $|E_2|/|E_1| = 0.6$, a new separation region appears at high frequencies for f_1 and low frequencies for f_2 . This separation region spans a range almost one decade long for both f_1 and f_2 . At this amplitude there is a large separation between the crossover frequencies.

Such a large separation region means that small errors in the frequency or in CM will not result in failure to separate the cells. The range (b) in Figure 3-4 is the same as the one in Figure 3-3. Increasing $|E_2|/|E_1|$ to 0.8 results in a reduction in the separation region, and the region becomes a more complex function of f_1 and f_2 .

3.3.4 Predicted Cell Positions

As mentioned previously, unlike CM , CM_{eff} is a function of location when multiple frequencies are produced on different electrodes. Thus, to predict the equilibrium positions of different types of cells on a particular electrode geometry, plots of CM_{eff} as a function of position are needed. The simplest configuration with which to demonstrate the use of multi-frequency DEP for simultaneously trapping different types of cells in separate locations is a 3-electrode configuration with two electrodes at different frequencies and the third electrode at ground. If the electrodes are triangular and rotated 60° from each other, the symmetry divides the three gaps between the electrodes into distinct regions. This geometry is nevertheless too complicated to readily solve the divergence of the electrical fields analytically everywhere in order to obtain the forces using equation (16). Instead, we ignored the central region where all three electrodes interact and only considered the "arms".

In the region between any two of the electrodes far from the third electrode, the effect of the third can be neglected because DEP forces decrease with the cube of the distance, so there is a rapid drop-off of the E field from the third electrode as one moves away from

the center. Figure 3-5 shows the CM_{eff} in regions a , b , and c for live and dead cells when 5 kHz and 5 MHz signals of equal amplitude are applied to the lower left and right electrodes, respectively. These values correspond to the labeled points in Figure 3-2. From these values, one would predict that only dead cells would collect between the 5 kHz electrode and ground, that only live cells would collect between the 5 MHz electrode and ground, and that both would collect between the 5 kHz and 5 MHz electrodes.

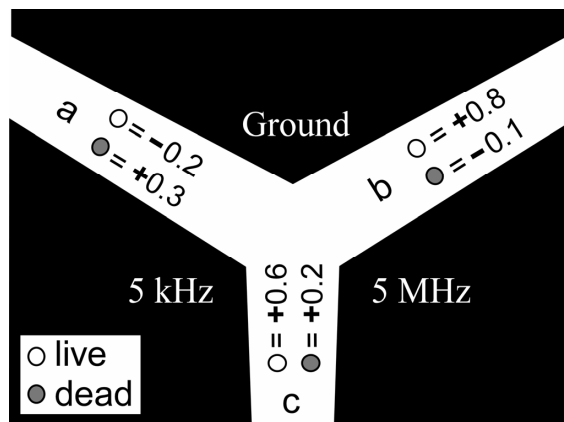


Figure 3-5. The effective Clausius-Mossotti factors for live and dead yeast cells between electrodes at 5 kHz, 5 MHz, and ground, obtained by taking into account only the closest two electrodes.

3.4 Experimental Work

3.4.1 Materials and Methods

The experiments that were performed were inspired by Pohl's early work on DEP [55], but using multiple frequencies coming from different locations instead of a pair of

electrodes at one frequency. Figure 3-6 shows the electrode geometry and connections. Two of the electrodes were excited using two function generators (4011A, BK Precision and F34, Interstate Electronic), both grounds of which were connected to the third electrode. The frequencies were selected based on the curves in Figure 3-2, which show that live yeast cells should experience positive DEP at 5 MHz and negative DEP at 5 kHz, while dead yeast cells should exhibit the opposite behavior.

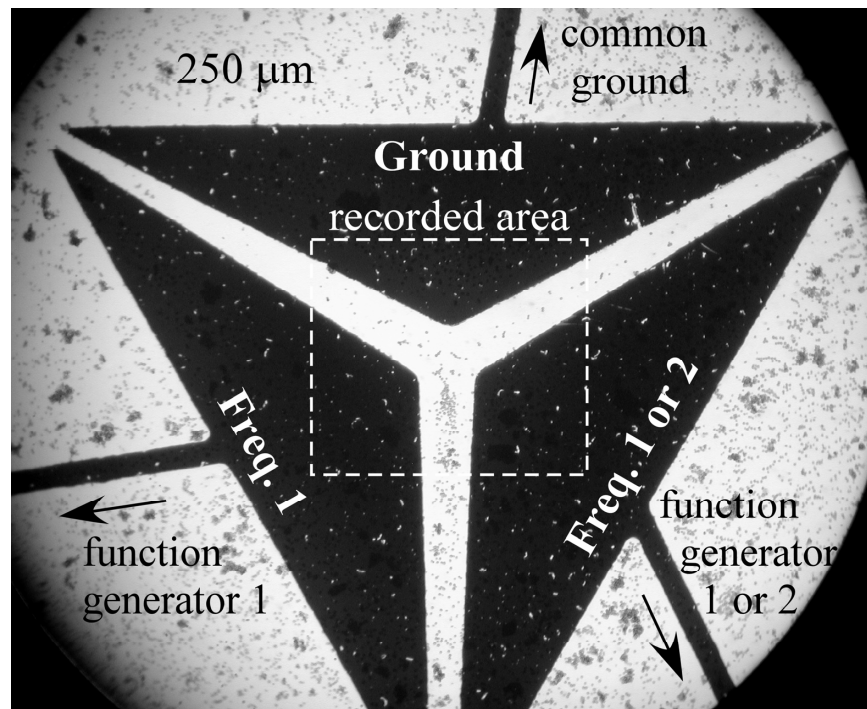


Figure 3-6. Photograph of the 2-frequency device, covered with yeast cells, that was used in the demonstration of simultaneous positive and negative DEP. The area shown in subsequent figures is indicated.

A 1000 Å thick Au film was deposited by thermal evaporation over a thin adhesion layer

of Cr onto a glass substrate (75 x 50 mm). The electrodes were patterned photolithographically using wet chemical etching (Au & Cr etchants, Transene). A polydimethylsiloxane (PDMS) film with a hole in it, made using a razor blade, was placed over the electrodes on the glass substrate, forming a chamber 600 μm deep and 10 mm on a side. This chamber was filled with an aqueous solution containing either dead yeast or a 50-50 mixture of live and dead yeast and covered with a glass cover slip.

Live and dead yeast cells were prepared immediately prior to each experiment because 3-4 hours after preparation the dead cells displayed negative DEP at all frequencies. To prepare live cells, 20 mg of dry yeast (Fleischmann's, ACH Food Companies) was added into 10 ml of deionized water (DI) at room temperature and the flask immersed in a water bath at 33° C. To prepare dead cells, 20 mg of dry yeast was added to 10 ml 50-50% methanol-DI to kill them. After 10 min., 1 ml of aqueous methylene blue (Sigma-Aldrich) solution (0.6 mg/ml) was added to both solutions to stain the dead cells. An additional 40 ml of DI was added 10 minutes later, and the solution left in the bath 50 min. longer with occasional stirring. Mixtures of live and dead yeast cells were prepared by adding the two preparations 1:1 (resulting in 5% methanol content). The yeast solution conductivity was measured with a conductivity meter (Amber Science, model 1056).

Before filling the PDMS chamber with cell solution, the electrodes were excited at a root mean squared (RMS) voltage of 5.7 V so that the quickly settling cells would immediately be subject to the DEP forces upon introduction to the chamber. The cells

settled in the chamber due to gravity, and as they approached the electrodes they were affected by the DEP forces that the electrodes produced. (If the voltage was applied after the solution was introduced, too many cells reached the substrate, where they stuck, before the fields were applied.) The AC signals were monitored using an oscilloscope (TDS 2024, Tektronix), and any DC offsets were reduced by manually adjusting the DC offsets on the function generators.

The cells on the electrodes were monitored through a microscope (Ergolux, Leitz) and images were recorded using a digital camera (Coolpix 990, Nikon) connected to the eyepiece port with an adapter. Transmission illumination best captured the difference in color between the blue cells (which appear dark, in the figures) and the clear cells. The region highlighted in Figure 3-6 was photographed once the cell positions were constant, typically after 10 min. To verify reproducibility, all experiments were repeated at least three times on different days.

3.4.2 Results: Single Frequency on One Type of Particle (Control Experiment)

The effect of using solely negative (Figure 3-7A) or positive (Figure 3-7B) DEP on dead yeast cells was assessed as a control. The two bottom electrodes were connected together to apply the same frequency and phase. Under 5 MHz, the cells were repelled from all three electrodes in the central region of the device shown in Figure 3-7A. This can also be seen in Figure 3-6, which is a less-magnified image of the same experiment, by comparing the cell densities in the areas between and outside the electrodes. (Also note,

in that image, the tendency of the cells to clump.) Cells were strongly repelled from the regions between the excited and ground electrodes. The repulsion in the area between the two 5 MHz electrodes was weaker and dropped rapidly with distance from the ground electrode, since there was no potential drop between the two bottom electrodes (they were at the same voltage at all times). A small percentage (~1%) of dark-dyed cells was attracted to the electrodes, possibly because they may not have been completely dead.

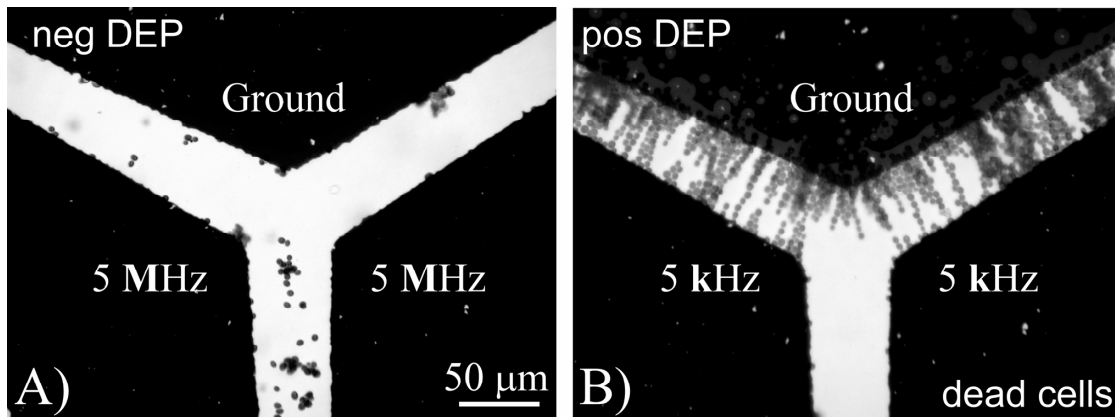


Figure 3-7. A) Killed, methylene blue stained yeast cells under AC fields of 5 MHz (negative DEP). The bottom electrodes were connected together and the top electrode was grounded. This region is a close-up view of Figure 3-6. B) Dead cells under AC fields of 5 kHz (positive DEP). In both A) and B), the voltage was 5.7 V. All images were taken using samples from the same yeast cell solution.

The electrodes in Figure 3-7B were excited at 5 kHz to apply positive DEP. As expected, the dead yeast cells were attracted to the region between ground and the excited electrodes, forming the well-known pearl-chains. Again, there were few cells in the region between the excited electrodes, even fewer than in Figure 3-7A. Although the

same voltage, 5.7 V, was used in both experiments, the CM at 5 kHz is three times that at 5 MHz (Figure 3-2), making the positive DEP forces stronger.

3.4.3 Results: Multiple Frequencies on One Type of Particle

With the control experiments producing the expected outcomes, we next examined the effect of generating negative and positive DEP forces simultaneously on different electrodes, as in Figure 3-5, again using dead yeast cells. The experimental results are shown in Figure 3-8. Just as predicted by the calculations, cells were attracted to the electrode edges between 5 kHz and ground ($CM_{eff} = +0.3$), while at the same time they were repelled from the electrode edges between 5 MHz and ground ($CM_{eff} = -0.1$). (As before, ~1% of dark cells were attracted to the electrodes at 5 MHz.) The cells were also attracted to the region between the 5 kHz and 5 MHz electrodes because, as determined in section 3.3.4, there the $CM_{eff} = +0.2$.

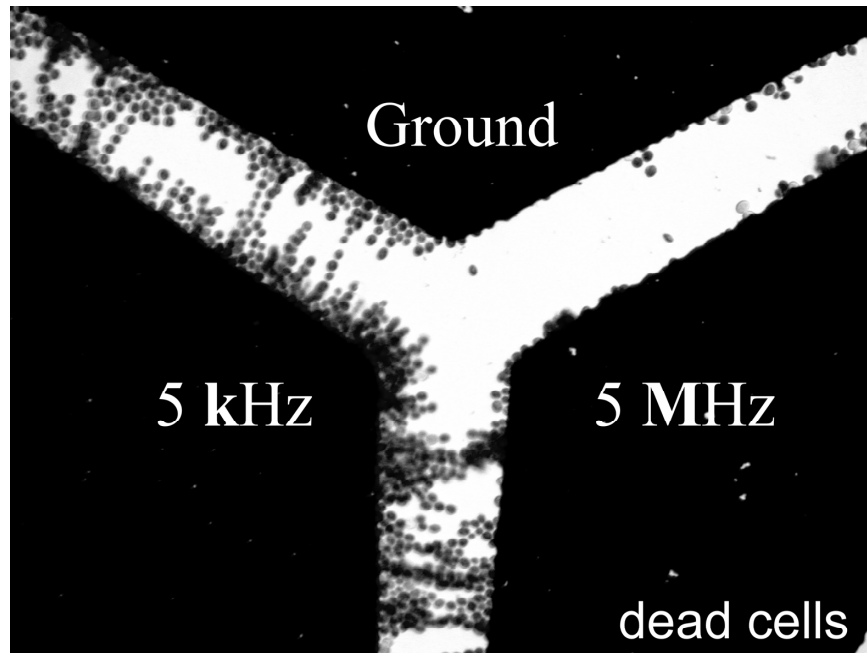


Figure 3-8. Dead yeast cells under simultaneous positive and negative DEP caused by exciting one electrode at 5 kHz and another at 5 MHz with the same magnitude of voltage (5.7 V). Compare model predictions in Figure 3-5.

To show that the position of the cells could be controlled by means of the amplitudes of the signals, as well as the frequencies, the experiment was repeated with different signal amplitudes: the 5 kHz signal had an RMS voltage of 2.2 V, while the 5 MHz signal had an RMS voltage of 8.5 V. As predicted (Figure 3-2B, point d), Figure 3-9 shows that in this case the dead cells were also repelled from between the excited electrodes because the 5 MHz negative DEP signal was stronger, giving a $CM_{eff} = -0.1$. The region between the ground and 5 kHz electrodes still attracted cells, but far fewer than in Figure 3-8.

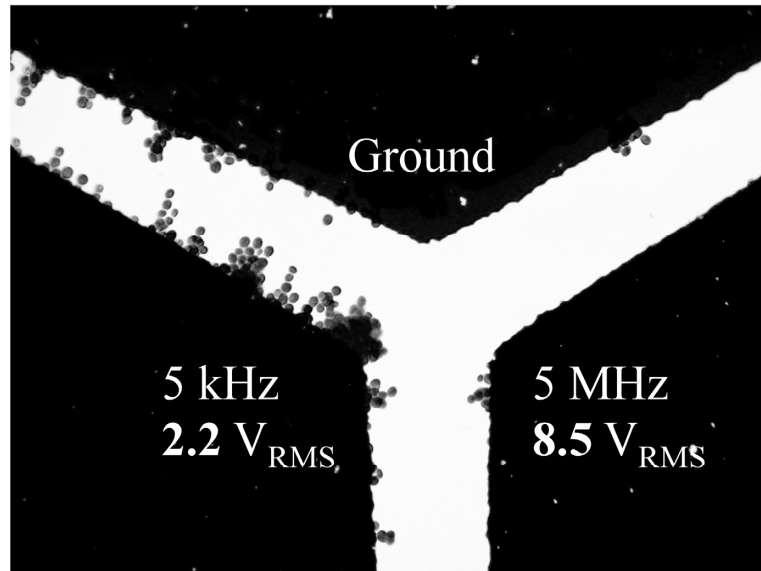


Figure 3-9. Dead yeast cells under simultaneous positive and negative dielectrophoresis caused by electrodes at voltages with different frequency and different amplitude.

3.4.4 Results: Multiple Frequencies on Two Types of Particles

We increased the complexity of the experiments by using a 50–50% mix of live and dead yeast cells (Figure 3-10). Near the 5 kHz electrode were a prevalence (95 +/- 8% based on 3 experiments) of dead cells, while live cells were prevalent (72 +/- 12%) near the 5 MHz electrode. The space between the excited electrodes was occupied by both live and dead cells. In section 3.3.4 we had estimated analytically that CM_{eff} for both live and dead cells was positive in that region. Experimentally, the cells were weakly separated between the excited electrodes, and this separation diminished with distance from the ground electrode.

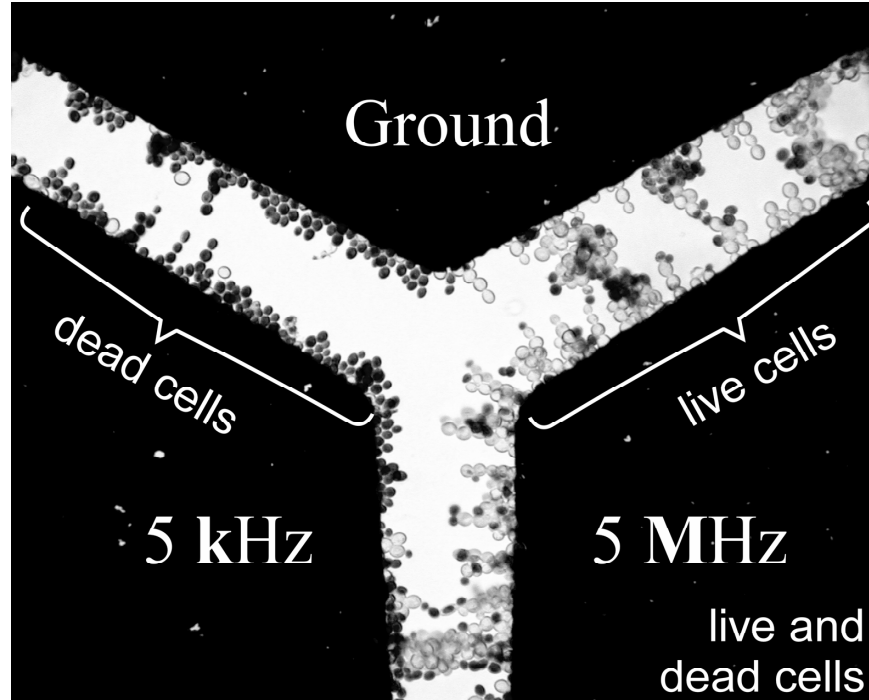


Figure 3-10. Positive and negative dielectrophoresis acting at the same time on live (clear) and dead (dark) yeast cells.

In this experiment live and dead yeast cells were selectively *attracted* to different locations, while at the same time separated from each other. This would not have been possible using only one frequency, which can only attract one group to a location while the other is repelled (compare Figure 3-7A). The separation of the different cells using attraction means that the position of each group is well defined and that the cells will be held there strongly despite other forces that may be present. As discussed below, this technique could be used to pattern different types of cells in close proximity to each other to, for example, form complex geometries of “cell consortia”, which are functional cell groupings that have applications in tissue engineering [5, 6].

There was a significant fraction of dark cells between the 5 MHz and ground electrodes. Based on the image, this appears to have occurred because dead cells clumped with live cells and were brought there by the larger forces on the live cells in the clump. We should note that about half of the dark cells between the 5 MHz and ground electrodes are away from the edges, toward the middle of the region, indicating that they were repelled from the electrodes.

3.5 Discussion

As previously shown in the literature, MFDEP can be used for the selective separation of particles with very similar Clausius-Mossotti spectra, which is problematic with only one frequency. One, two [145, 155], and even three [174] frequencies have been used in the separation of particles, but these frequencies were produced on the same electrodes. In this work, we have introduced the concept of the separation of particles using different frequencies on different electrodes. One can thereby also separate more particle types from a complex mix. By selectively attracting particles to different electrodes, it is possible to separate *at least* as many groups of particles as there are electrodes at different frequencies plus one (one group of particles can be left in the solution). Even more groups could be separated by utilizing the plot of CM_{eff} as a function of location, and by cleverly choosing frequencies and electrode placement.

A potentially valuable MFDEP application is the active canceling of parasitic cages.

DEP is increasingly being implemented in complex microsystems that include several technologies, and electric field distortions caused by those devices can result in parasitic DEP cages. Although such effects have been utilized to advantage [138, 144], at other times they pose a problem [113]. Likewise, undesired DEP parasitic cages can be produced by the electrical fields used in electroosmotic flow, electrical impedance spectroscopy, and electrophoresis. These parasitic cages can be actively cancelled by placing electrodes at or near these field inhomogeneities at frequencies that cancel the undesired DEP forces, provided that the added frequencies have no adverse affect on the action of the main signal.

DEP has been used to position cells with the goal of defining heterogeneous multicellular structures [5, 6]. In previous work [5], hepatocytes were attracted to concentric ring electrodes using positive DEP, and pearl chaining resulted in striations similar to those found naturally in liver tissue. This multicellular pattern was then randomly covered with endothelial cells, resulting in an artificial hepatic lobule, which is the multicellular unit building-block of the liver. MFDEP can be used to go beyond the present work, positioning in a single step different types of cells in close proximity to each by selectively attracting them to different locations. This allows more complex structures to be formed. A relatively simple example is the assembly of arteries, which are cylinders, composed of an outer ring of smooth muscle cells and an inner ring of epithelial cells.

We illustrate in Figure 3-11, using live and dead yeast, how cells can be patterned into concentric rings. Live and dead yeast cells were prepared following the same procedure

described above, but with 5 times higher yeast concentration. The outer ring was set at 5 MHz (5.5 V, RMS), the middle ring was grounded, and the inner ring was set at 5 KHz (4.5 V, RMS). Live cells were thus attracted to the gap between the two outer electrodes, while dead yeast cells were attracted to the gap between the two inner electrodes. Dead yeast, pushed away due to the negative DEP forces produced by the outer electrode, can be seen surrounding the electrode structure. Using this technique, which relies on MFDEP, different types of cells can be segregated from regions that are quite close to each other, in this case as close as 20 μm .

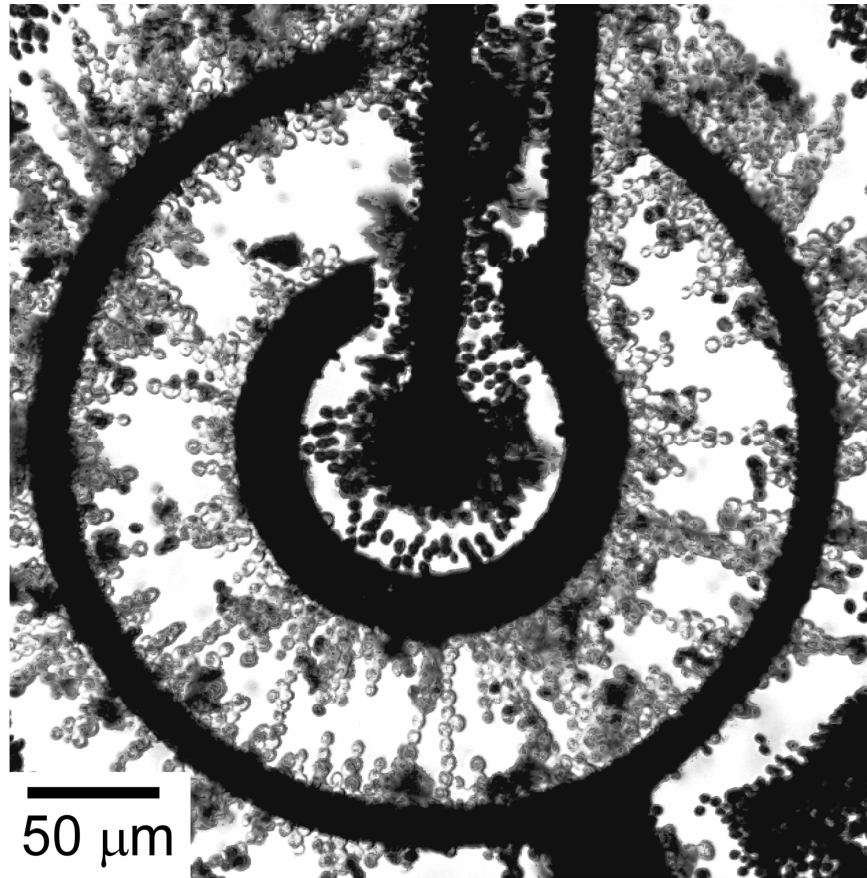


Figure 3-11. Live (clear) and dead (dark) yeast cells selectively patterned in a single step by means of MFDEP. The inner electrode was at 5 kHz, the middle ring electrode was grounded, and the outermost ring electrode was at 5 MHz.

Patterning the cells in a single step not only saves time and reduces the exposure of the cells to potentially harmful DEP-favorable solutions (i.e., solutions with low electrical conductivity), but it also raises the possibility of developing new cell manipulation techniques. For example, it should be possible to re-structure dissociated tissue and organs to form new tissue with a different shape without having to first separate the different types of cells. With such a method, one could envision forming, in minutes,

artery sections out of dissociated vessel tissue from a patient for treatment of coronary disease, or the reconstruction of visual pathways out of dissociated brain tissue for scientific research.

MFDEP would also enable DEP-based particle steering. Armani et al. [40] showed the accurate steering of multiple particles through figure 8s and other trajectories by means of feedback-controlled electroosmotic flow (EOF). This particle-manipulation technique required vented fluid reservoirs for the electrodes because of hydrolysis associated with EOF. In addition, EOF is challenging over surfaces covered by heterogeneous materials because of the varying surface charges. These drawbacks do not exist in DEP-based systems, yet MFDEP makes it possible to control multiple particles. However, one issue with using DEP forces is that they increase rapidly near the electrodes where there are high electric field gradients, and these strong force gradients may pose control problems. Amplitude modulation does not alter the gradients. One solution is to control the force by modulating the frequency, thereby varying the force by means of the Clausius-Mossotti factor. In so doing, the force near each electrode will be dominated by that electrode alone, without interference from the other electrodes, and controlled repulsion can be achieved. An MFDEP-based system would increase the number of particles that can be steered independently because the inflow and outflow drag forces would be replaced by positive and negative DEP forces, and one can in addition exert forces on selected particles based on variations in their CM response (for example, by using frequencies at which some of the particles have $CM \sim 0$).

3.6 Concluding Remarks

In previous work it has been established that the effect of multiple frequencies can be determined by adding the forces produced by each frequency, calculating each force separately. We take a new approach of modeling the effect of multiple frequencies by defining an effective Clausius-Mossotti factor CM_{eff} for multiple frequencies, which allows one to examine the effect of the frequency combination and the relative signal amplitude without the influence of other parameters that are included when studying the forces. This definition of CM_{eff} is consistent with, and it applies to, all previous studies on dielectrophoresis. To model the effect of multiple frequencies on devices designed to use one frequency it is only necessary to adjust CM to CM_{eff} . Because it is based on CM , CM_{eff} can be used with non-spherical particles, such as ellipsoids, as well.

We have analyzed the dielectrophoretic forces due to multiple frequencies coming from different locations and having different amplitudes, and have presented experiments that validated the analysis. We were able to separate a mixture of live and dead yeast cells by simultaneously, and selectively, attracting each group to a different electrode. Since both groups were trapped, it would be possible to separate them from a third group, even if other forces were present. Yet another group could be separated and collected in the region between the excited electrodes if the net force there was repulsive to both live and dead cells. MFDEP thus extends the limits of what is possible using only a single frequency, enhancing the technique by increasing the number of control parameters.

3.7 Appendix

The dielectrophoretic force in the time domain can be written as

$$(18) \quad \vec{F} = (\vec{\mu} \bullet \nabla) \vec{E}$$

where $\vec{\mu}$ is the induced dipole and E is the time-dependent electric field. The induced dipole is given by

$$(19) \quad \vec{\mu} = A * CM * \epsilon * V * \vec{E} .$$

Electric fields from different sources add linearly to give the total electric field at any point:

$$(20) \quad \vec{E}_{total} = \sum_i \vec{E}_i .$$

The force due to \vec{E}_{total} is

$$(21) \quad \vec{F}_{total} = (\vec{\mu}_{total} \bullet \nabla) \vec{E}_{total} .$$

For simplicity, we treat the case of two sinusoidal fields \vec{E}_1 and \vec{E}_2 with $f_1 \gg f_2$. Then equation (18) becomes

$$(22) \quad \vec{F}_{total} = [(\vec{\mu}_1 + \vec{\mu}_2) \bullet \nabla](\vec{E}_1 + \vec{E}_2) \\ = (\vec{\mu}_1 \bullet \nabla) \vec{E}_1 + (\vec{\mu}_1 \bullet \nabla) \vec{E}_2 + (\vec{\mu}_2 \bullet \nabla) \vec{E}_1 + (\vec{\mu}_2 \bullet \nabla) \vec{E}_2$$

The electric field frequencies are much faster than the movement of the particles (the two

signals are at different frequency, but both are far above that of observable motion). \vec{E}_i oscillates between positive and negative values symmetrically around zero, so each of the cross-product terms has a time-average value of zero. Since we are only interested in the time average force,

$$(23) \quad \underline{\vec{F}}_{total} = (\underline{\vec{\mu}}_1 \cdot \nabla) \underline{\vec{E}}_1 + (\underline{\vec{\mu}}_2 \cdot \nabla) \underline{\vec{E}}_2$$

and the total dielectrophoretic force on a body can be found simply by adding the different force components.

To find a value for $\vec{\mu}_{tot}$ to use in equation (21), one can derive a CM_{eff} by combining equations (19) and (21).

$$(24) \quad \frac{A}{2} CM_{eff} \epsilon V \nabla |E_{total}|^2 = \frac{A}{2} CM_1 \epsilon V \nabla |E_1|^2 + \frac{A}{2} CM_2 \epsilon V \nabla |E_2|^2$$

$$(25) \quad CM_{eff} = \frac{CM_1 \nabla |E_1|^2 + CM_2 \nabla |E_2|^2}{\nabla |E_{total}|^2}$$

In the subset of cases in which both frequencies come from the same electrodes, their divergences are the same and equation (25) reduces to

$$(26) \quad CM_{eff} = \frac{CM_1 |E_1|^2 + CM_2 |E_2|^2}{|E_1 + E_2|^2}$$

Averaging over time, equation (26) further reduces to

$$(27) \quad \underline{CM}_{eff} = \frac{CM_1 |E_1|^2 + CM_2 |E_2|^2}{|E_1|^2 + |E_2|^2}$$

where the $E_1 E_2$ cross-product drops out because it averages to zero. Thus, CM_{eff} can be obtained by taking the *amplitude-weighted average* of the signals.

Likewise, extending the analysis to more than two frequencies, if the gradients are unequal, then

$$(28) \quad CM_{eff} = \frac{\sum_i^n CM_i \cdot \nabla |E_i|^2}{\nabla |E_{total}|^2}$$

and if they are equal, then

$$(29) \quad \underline{CM}_{eff} = \frac{\sum_i^n CM_i |E_i|^2}{\sum_i^n |E_i|^2}$$

Chapter 4 Dielectrophoretic Vial Traps to Load Cell into Vials¹¹

4.1 Abstract

This paper presents a method to load cells into microvials using dielectrophoresis. This has not been possible until now because such features produce electric field distortions that interfere with the dielectrophoretic manipulation. We used multiple frequency dielectrophoresis to actively cancel out the effect of these distortions and successfully load many cells into a vial in a matter of seconds in fluid flows of up to 300 $\mu\text{m/s}$. The method of actively cancelling field distortions enables the presence of features that would otherwise be prohibited near regions of dielectrophoretic manipulation, significantly expanding the environments in which dielectrophoresis can be used.

4.2 Introduction

One of the first dielectrophoretic (DEP) devices consisted simply of a wire and a metal dish; its purpose was to demonstrate the exertion of forces on small bodies using DEP [51]. More recent DEP devices are aimed at practical applications, such as neural networks [7], cell manipulation [74], and tissue engineering [5]. Publications on DEP device design have aided this evolution [133-143, 175]. However, there are still issues

¹¹ This chapter will be submitted for review, after minor modifications, to the Journal *Lab on a Chip* under the title “Parasitic Trap Cancellation Using Multiple Frequency Dielectrophoresis, Demonstrated by Loading Cells into Cages”, by M. Urdaneta and E. Smela.

that emerge when DEP is applied to practical applications of increasing complexity. One of these is parasitic traps¹², or regions of undesired accumulation of particles [115].

Parasitic traps appear due to undesirable distortions of the electric fields, caused by electrode geometry or by the presence of either conductors or insulators. Manipulated cells can become “lost” as far as device operation is concerned [115]. While some researchers have found uses for the distortions produced by insulating posts [138, 144, 176], parasitic traps more often limit the usefulness of DEP devices by restricting the locations of other features. In lab-on-a-chip systems, for example, in which DEP is used to prepare cell samples, DEP is limited to regions without such features as filtering screens, pre-concentrating structure, tissue scaffolds, and sensing electrodes.

Parasitic trapping can be reduced by changing the vial geometry or material. However, this is frequently infeasible or difficult in scenarios in which cell manipulation is not a goal in itself, but instead is a means to enable the actions of other device components.

This paper presents a method of eliminating parasitic traps by using multiple frequency dielectrophoresis (MFDEP) [145, 146], thereby allowing the realization of an application

¹² Please note that, because of the widespread use of the term "cell cage" in the community in which this paper will be published to mean a structure used to trap and retain cells, the term "parasitic cage" was changed to "parasitic trap" in the paper that resulted in this chapter.

that would otherwise be impossible: loading cells into microscopic vials. Cell vials, or cages, are used in long-term cell studies to restrict the motion of motile cells, such as neurons [9-12, 177, 178]. Until now, researchers have relied on methods such as random cell seeding, optical tweezers, suction, and manual loading, but DEP is superior to those methods in terms of speed, system integration, accuracy, and miniaturization. While the task of loading cells (or any particle) into a vial using DEP may appear trivial, it is not because parasitic traps inevitably appear at the vial entrances. The cell loading application can be viewed as a case study that illustrates the capabilities of the MFDEP trap-cancelling method.

4.3 Background

4.3.1 Cell Clinics

For our research, cells need to be loaded into the microvials of a “cell clinic”, an integrated, hybrid CMOS/MEMS cell culture and monitoring system with a wide range of potential applications, from chemical sensing to drug discovery [1, 3, 179]. The custom CMOS chips measure the activity and health of cells by means of various sensors [180-182]. The vials are designed to immobilize a desired number of cells on top of the sensors, and with the lids closed provide electrical, physical, and chemical isolation from both other cells and from substances introduced into the system. The lids are opened and closed by Au/polypyrrole bilayer actuators [1, 3, 179], which can be driven using an integrated potentiostat [183, 184]. For the work reported here, the vials were made of SU8 and were 100 μm on a side and 50 μm tall. In the cell clinics system, there are a

limited number of materials that can be used to fabricate the vials, and changing the vial geometry affects the rest of the system.

4.3.2 Cell Loading

As mentioned above, the methods that researchers have been using to load cells have some disadvantages. Randomly seeding cells over the vials [1] is undesired because of poor accuracy in the position and number of cells loaded. Manual placement [9-11, 177] is impractical for large numbers of cells. Suction loading [178] cannot readily be integrated with CMOS chips densely covered with circuits and sensors. Laser tweezers systems [12] are expensive and only allow a few cells to be loaded at one time. DEP, on the other hand, only requires electrodes and signal generators, which are compatible with CMOS/MEMS. DEP systems are compact, their operation can be handled on-chip (the technology is integratable), they can be used to load scores of cells simultaneously, and, in addition, they are inexpensive.

The general loading approach starts with transporting cells suspended in a medium to the vicinity of each vial by means of fluid flow. DEP is then used to bring cells into the vial. An obvious approach is to attract cells using positive (attractive) DEP forces from an electrode inside the vial. Figure 4-1A shows the result of a simulation of this approach: cells do not go into the vial, but are instead trapped at the vial edges. This outcome is also seen experimentally, as shown in Figure 4-1C and D.

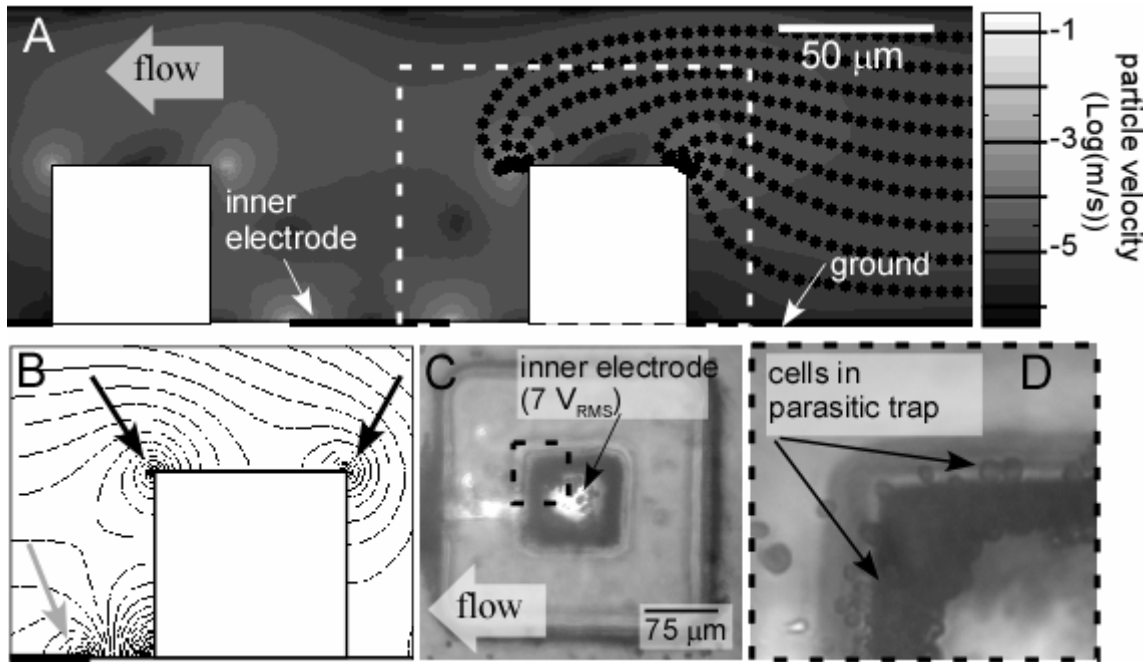


Figure 4-1. Side view of numerical simulation results for positive DEP applied inside a vial without parasitic trap cancellation. The ground electrode is on the floor, outside of the vial. A) Particle tracing results. The background gray levels represent velocity contours, with lighter shades showing higher velocities (forces). The flow speed above the vial is $60 \mu\text{m/s}$ from right to left. B) Close-up of the region inside the dashed white box in A) showing the electric field contours (logarithmic scale) near the vial walls. The arrows point to regions where the electric fields increase rapidly; these are the regions to which cells are attracted. C) Top view of an SU8 vial with an electrode in the center applying positive DEP in a solution containing non-viable yeast cells. D) Close-up of the vial rim (area shown in the dashed box in C), showing cells in the parasitic trap, instead of inside the vial.

DEP forces are proportional to the electric field strength E times the electric field

gradient [41, 51]

$$(30) \quad \vec{F} = 4\pi\epsilon_m \operatorname{Re}(CM) R^3 (\vec{E} \cdot \nabla) \vec{E}$$

where ϵ_m is the medium permittivity, R is the particle radius, and $\operatorname{Re}(CM)$ is the real part of the Clausius-Mossotti factor [41, 51].

The electric field distribution in the region of interest can be found through Laplace's equation,

$$(31) \quad \nabla E = 0$$

, with the condition that at the interface of two materials, 1 and 2, with different electrical properties the continuity of the field, or

$$(32) \quad \epsilon_1 E_1 = \epsilon_2 E_2$$

, holds true [50]. Where $\underline{\epsilon} = \epsilon + \sigma j/\omega$, and σ is the conductivity and ω the field frequency. From this condition follows that when geometrical and electrical inhomogeneities appear, the electric field will be distorted in its vicinity.

The distortions created by the SU8 vials can be visualized by plotting electric field contour lines near the vial wall, as shown in Figure 4-1B. The DEP forces are positive at the frequencies applied on the inner electrode, meaning that cells are attracted to regions where the electric field increases rapidly (indicated by the arrows), and repelled from regions where it decreases rapidly (such as in the corner inside the vial between the vial wall and the electrode). Since cells approach from above, they are trapped at the vial edges.

4.4 Results

4.4.1 MFDEP Vial-Loading Design

Cross sections of devices fabricated with ground electrodes on either the floor (case A) or ceiling (case B) are shown in Figure 4-2. These include an additional electrode on top of the vial walls. Fabrication methods are detailed in the Experimental section. An array of 4 by 3 vials was located within a microfluidic channel 1.8 mm wide and 100 μm tall.

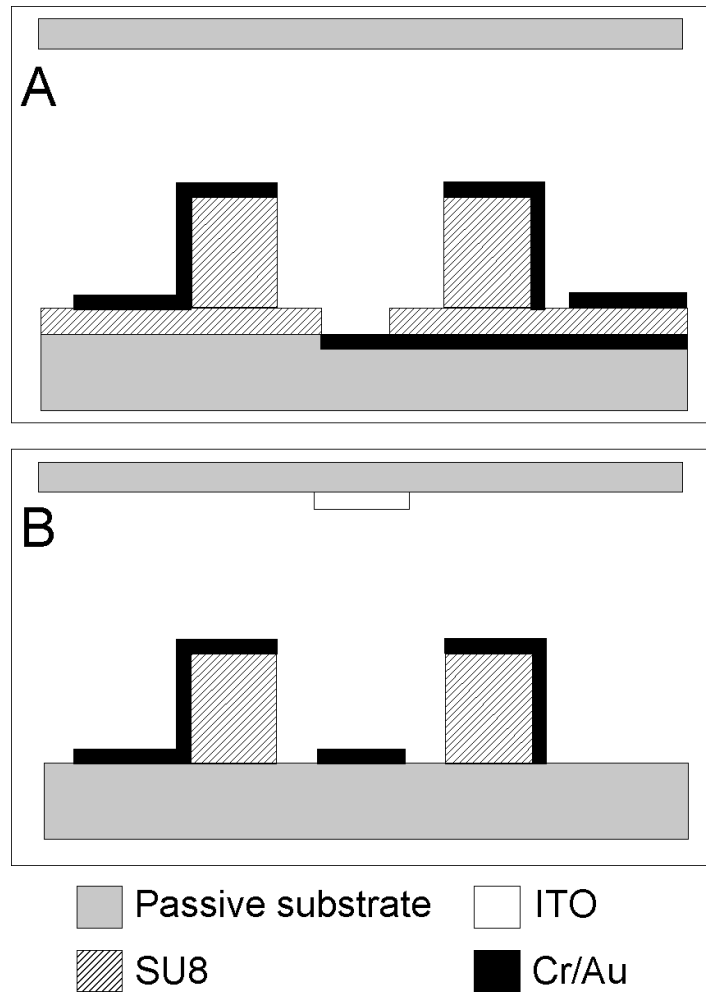


Figure 4-2. Cross-section of vial cage devices with ground electrodes on A) the floor and B) the ceiling.

In order to cancel the parasitic traps, the outer electrodes on top of the vial walls (Figure 4-3) were excited at a frequency that produced negative (repulsive) DEP, nDEP. The purpose of this was to gently push cells away from the parasitic traps so they could travel into the vial under the attractive (positive) DEP forces, pDEP, produced by the electrode within the vial (Figure 4-3C).

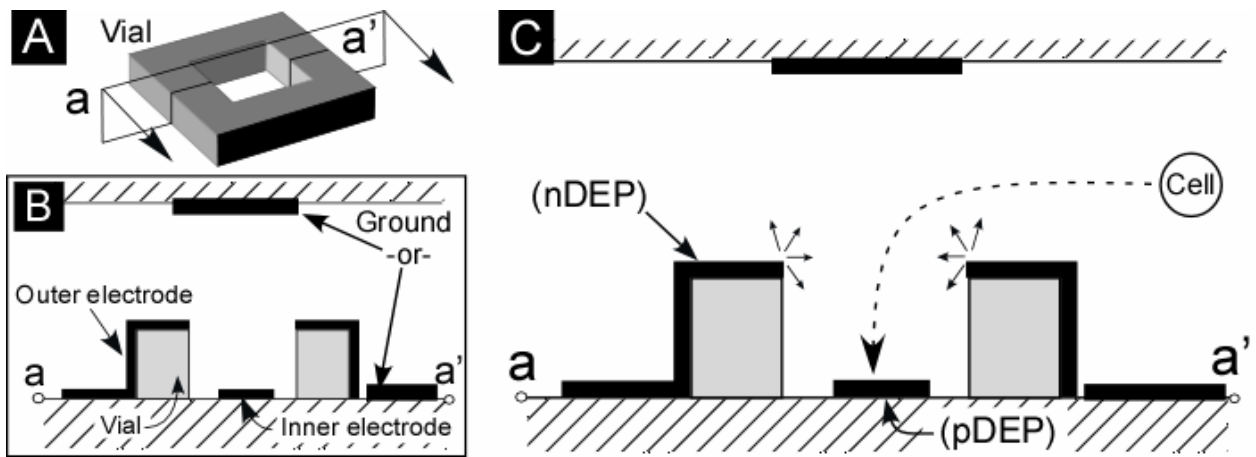


Figure 4-3. A) Schematic of one of the vial traps in a ceiling-ground configuration. B) Cross-section a-a' of the vial trap showing the positions of the inner, outer, and ground electrodes. C) Working principle of the DEP cell-loading system. The inner electrode attracts cells into the vial, and the outer electrodes actively cancel the parasitic trap at the vial rim.

The nDEP force must be large enough to cancel the parasitic trap, but not so large that it prevents cells from going into the vial altogether. The ground electrode needs to be located close to the nDEP and pDEP electrodes in order to produce the desired electric field gradients; if it is too far away, then the electrode with the larger voltage dominates the other to the point that it is effectively inactive.

4.4.2 Floor-Ground Configuration

Simulation and experimental results for a device with the ground electrode on the floor, configuration A, are given in Figure 4-4. The particle-tracing simulations in Figure 4-4A show that the particles are initially pushed up, away from the vial edges, by the nDEP

forces produced by the outer electrode. Once over the vial, those in trajectories that start $< 20 \mu\text{m}$ from the floor become trapped at the inner edge on their way in, those at heights of $25\text{-}35 \mu\text{m}$ are successfully loaded, those at $40\text{-}60 \mu\text{m}$ are trapped at the opposite edge, and those above that height pass over the vial.

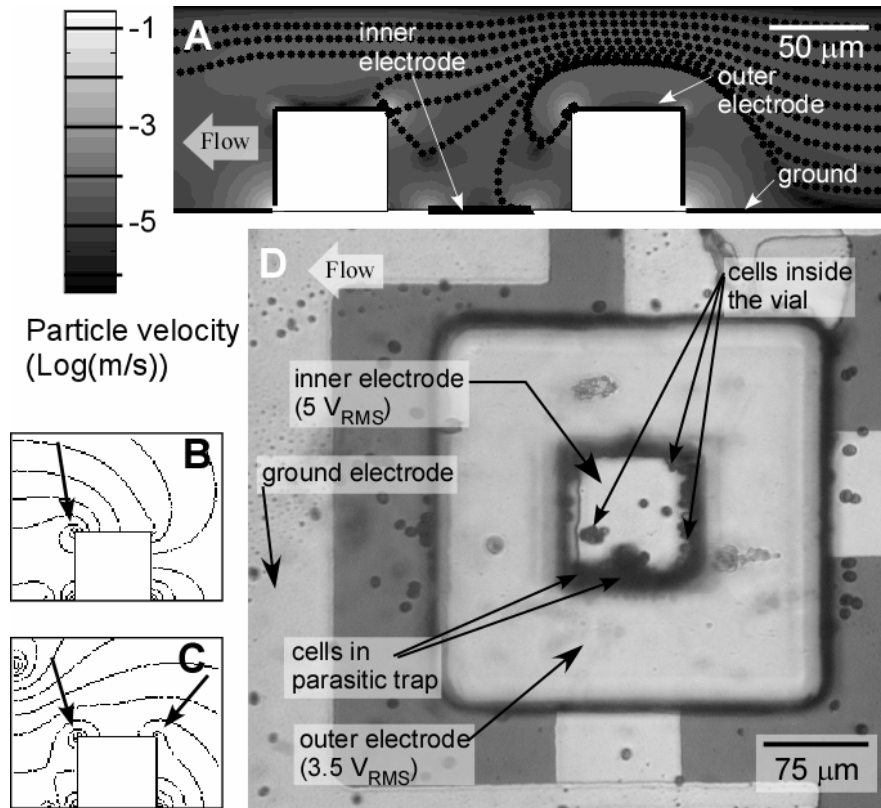


Figure 4-4 . A) Particle tracing simulations of an MFDEP vial trap in a channel 100 μm tall with 60 $\mu\text{m}/\text{s}$ flow speed above the vial, 5 V_{RMS} on the inner electrode, and 3.5 V_{RMS} on the outer electrode. The gray levels represent velocity contours (in log of m/s). B,C) Log scale contours of the electric fields due to the B) pDEP and C) nDEP electrodes, with arrows indicating regions of highest attractive and repulsive force, respectively. D) Experimental results of an MFDEP vial trap in a channel 125 μm tall with 50 $\mu\text{m}/\text{s}$ flow speed above the vial. The inner electrode was held at 5 V_{RMS} , and the outer electrode at 3.5 V_{RMS} .

Experimental results at flow speeds of 50 – 60 $\mu\text{m}/\text{s}$ corroborated the simulations (Figure 4-4D). A number of cells were loaded into the vials, and a similar number were captured

in the parasitic trap. Cells flowing high above the vial continued to flow past it without going in, and this is also consistent with the simulation. The simulations suggested that a larger fraction of cells should be parasitically trapped. The discrepancy is likely due to the different flow velocity distributions: in the 2D simulation the flow accelerates above the vial, to compensate for the reduced channel cross-section, to a greater extent than in the experiments, in which the flow can also bypass the vial around the sides.

These results show that the active cancellation of DEP parasitic traps is possible, but how can cells traveling within a wider height range be loaded? Figure 4-4B and C show contour curves of the electric fields produced by the pDEP and nDEP electrodes. At these voltages, the attractive and repulsive forces almost cancel each other, but near the vial edges the forces from the pDEP inner electrode dominate. This is not just a result of the higher voltage on this electrode, but also a result of interactions between the nDEP and pDEP electrodes: because of the placement of the ground electrode outside the vial, inside the vial the nDEP electrode interacts more strongly with the pDEP electrode than with the ground electrode. Raising the voltage on the nDEP electrode does not solve the problem, but simply prevents cells from entering the vial. To improve loading, the nDEP electrode must interact more strongly with the ground.

4.4.3 Ceiling-Ground Configuration

To decrease the interaction between the outer and inner electrode, the ground electrode was moved to the channel ceiling, closer to the nDEP electrode. This has a second benefit for loading: because of its strong interaction with the nDEP electrode, the ground

electrode will also repel cells, pushing them closer to the vial.

Simulation results, Figure 4-5A, predict that cells starting at heights 25 - 95 μm above the floor will be loaded. At the same time, loading occurs at flow speeds up to five times greater than in the previous configuration (300 - 400 $\mu\text{m/s}$). Notice that cells traveling close to the ceiling are pushed down by the ground electrode edge, as expected. The parasitic trap has still not been completely eliminated, however: lower trajectories, which are closer to the entrance rim, are still trapped. Simulations show that varying the voltages on the electrodes does not improve the cancellation.

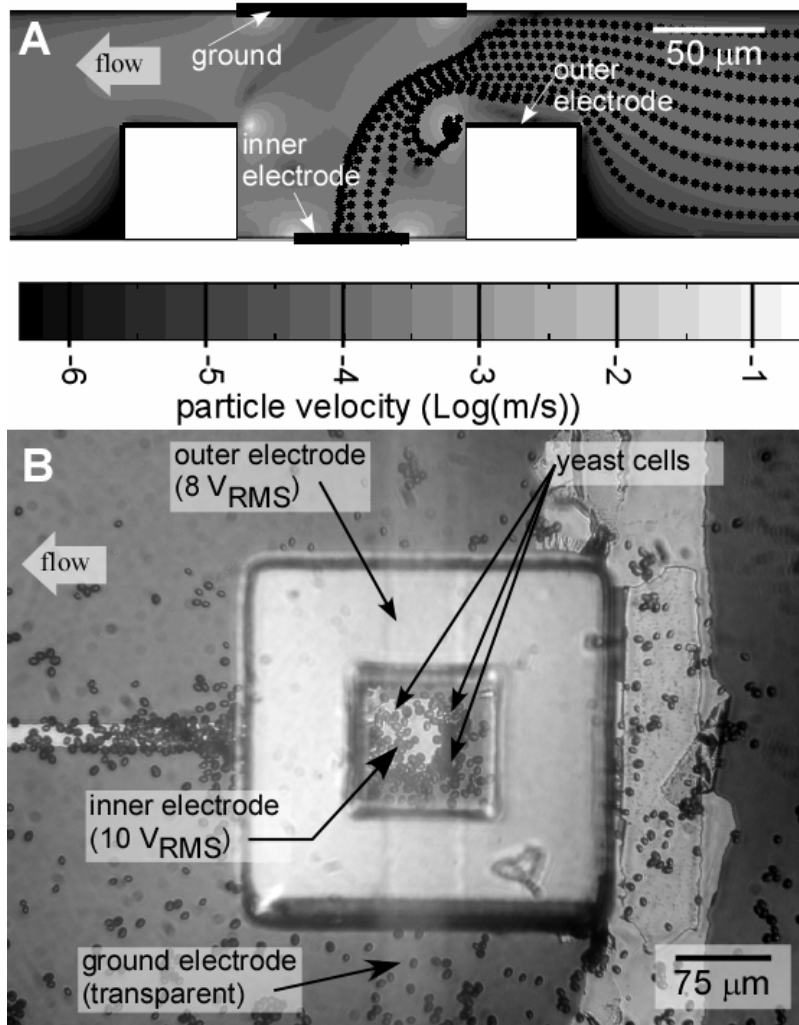


Figure 4-5. A) Particle tracing simulations of an MFDEP vial trap with the ground electrode on the ceiling in a channel 100 μm tall with 300 μm/s flow speed above the vial. The inner pDEP electrode was at 7 V_{RMS}, the outer nDEP electrode was at 5 V_{RMS}.

The simulation results were confirmed experimentally. Cells were loaded into the vials at flow speed of 300 μm/s, as shown in Figure 4-5B, with very few cells trapped at the rim (estimated at < 10%).

4.4.4 Trap Cancellation + Focusing

We have shown how parasitic traps can be cancelled to the point that we can perform manipulations that would be impossible if the parasitic traps were present. Nevertheless, some cells are still trapped at the parasitic trap instead of going into the vial. How can cell loading be further improved?

One way is to shift the original trajectory of the cells to heights in the channel in which they do go into the vial by means of cell focusing. This is a standard procedure in a series of manipulations to give cells a known initial position. Typically particle focusing is done using sheath flows [152, 185-187], but dielectrophoretic focusing has also been demonstrated for some time [74, 121, 125, 166].

Figure 4-6 shows particle tracing simulation results for A) floor-ground and B) ceiling-ground vials combined with particle focusing upstream of the vials. The nDEP focusing electrodes in Figure 4-6A consist of a 25 μm wide electrode on the ceiling and a 250 μm wide electrode on the floor; the asymmetry of the electrodes causes particles to be pushed towards the bottom of the channel [175]. The focusing electrodes in Figure 4-6B consist of two 50 μm wide electrodes across the channel from each other; their symmetry of the electrodes causes particles to be pushed towards the middle of the channel [175]. The design of the focusing electrodes was guided by the design method presented in ref. [175].

Particle focusing dramatically improves the loading capabilities. In Figure 4-6A all the particles that started $> 20 \mu\text{m}$ above the channel floor were loaded, and in Figure 4-6B all the particles were loaded.

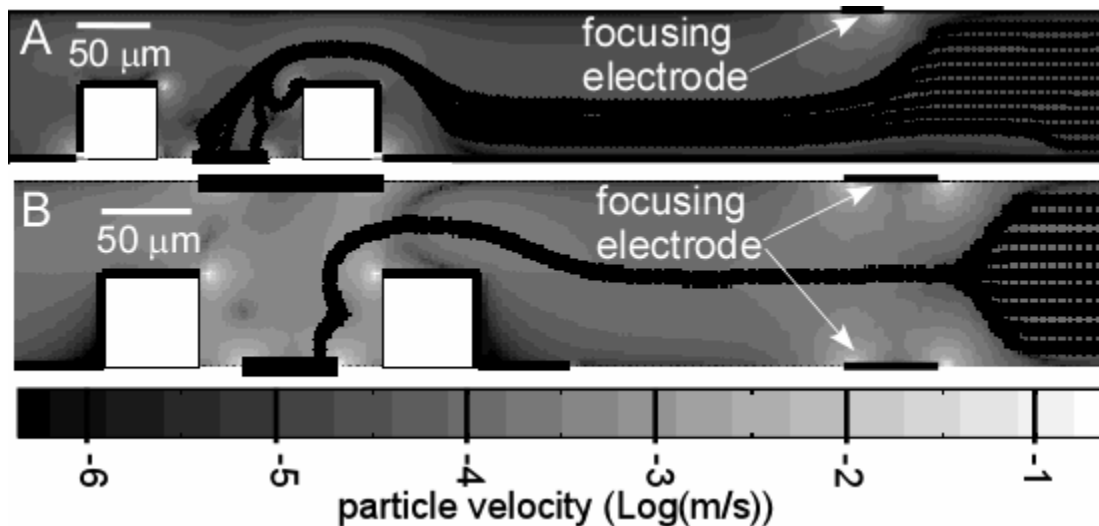


Figure 4-6. Simulations of vial loading enhanced by nDEP particle focusing. A) Floor-ground vial trap with electrodes excited at 5 (inner), 3.5 (outer), and 9 (focusing) V_{RMS} under $20 \mu\text{m/s}$ bulk flow (up to $60 \mu\text{m/s}$ above the vial). B) Ceiling-ground vial with electrodes excited at 7 (inner), 5 (outer), and 9 (focusing) V_{RMS} under $100 \mu\text{m/s}$ bulk flow (up to $300 \mu\text{m/s}$ above the vial).

4.5 Conclusions

It is difficult to estimate the number of applications that have been condemned by parasitic traps, but it is likely that this problem will become more prevalent as DEP is included in increasingly complex systems. Until now, there was no way to deal with

parasitic traps other than surrendering desired feature geometries or materials, which encumbers device development. In this paper, we have presented a method to actively reduce these traps using MFDEP. The method has enabled an automatic microvial cell loading device, which was demonstrated through simulations and experimentally. It is likely that other devices will be enabled by this same method.

4.6 Methods

4.6.1 Numerical Models

The flow velocity distribution and electric fields in the channel were modeled numerically using 2D models (Femlab 3.1, Comsol). The DEP forces were calculated using the governing equation for DEP [41]. The model included multiple electrodes at different frequencies, modeling one electrode at a time, with all the other electrodes grounded and other surfaces insulated, and adding the DEP forces obtained for each frequency.

DEP forces were converted to particle velocities so they could be superimposed on the fluid velocity, yielding a velocity vector field map that can be used to model the trajectory of the cells. The conversion was done by balancing the DEP force and the fluid drag forces on the cells [175]. The Clausius-Mossotti factor of the dead yeast cells was determined using the "multiple shell" model [41] using published [84] and measured [146] parameters and a cell radius of 5 μm .

Particle trajectories were calculated using a particle-tracing routine written in Matlab. The particle velocity vector field was imported from Femlab into Matlab, and the routine modeled the motion of the cells using the local velocity vector. The routine used a fixed distance step of 2 μm (distance steps were used instead of time steps because velocity values spanned several orders of magnitude, so there was no time step appropriate for all velocities in the channel). The initial position of the particles was 100 μm upstream from the vial at heights between 10 and 90 μm in 10 μm increments.

4.6.2 Device Fabrication

The fabrication was done using standard microfabrication techniques. The floor substrates were oxidized silicon wafers. A layer of Cr/Au thermally evaporated was patterned by wet etch served to form the inner electrodes used to apply positive DEP inside the vials, and in case B, also the electrical connections to the outer electrodes used for trap cancellation.

The floor-ground device A required three sets of electrodes on the same plane. For this purpose an insulating SU8-5 (Microchem) layer, 10 μm thick, was patterned on top of the inner electrode metal layer to separate it from the overlying outer and ground electrode layers, with openings inside the vials to expose the inner electrodes to the solution. The fabricating process suggested by the manufacturer was followed. The vials were fabricated next using SU8-50 (Microchem). Each vial was 50 μm tall, had an opening of 100 μm x 100 μm , and had a wall thickness of 50 μm).

The outer electrode lay on top of the vial. Part of the outer electrode had to reach the device floor to make electrical connection. Patterning this metal layer on top and on the sides of the vial without electrical interruption was a fabrication challenge. Photoresist (Shipley 1813) spun near the 50 μm tall vials had an irregular thickness: convex corners tended to have thin or no photoresist, while concave corners tended to accumulate excess resist. In addition, air bubbles became trapped inside the vials if the photoresist was placed directly on the device, and these bubbles ruined the photoresist pattern by bursting during the soft-bake step. Also, the mask could not be brought any closer to the substrate than the height of the vials, 50 μm , which resulted in degradation of the mask pattern on the device floor.

To overcome these problems, lift-off was used instead of wet etching because it required less photoresist on the substrate floor. The air bubbles were eliminated by adding acetone to the substrate while it was on the spinner: the acetone wetted the vials, leaving no air trapped in them. Generous amounts of photoresist were pipetted onto the substrate to displace the acetone, which mixes well with photoresist. After most of the acetone was displaced, the entire device was coated in photoresist, without any air bubbles. A relatively even coat of 1813 was produced by slowly ramping (500 rpm/s) the spinning velocity to 5000 rpm, and leaving it there for at least 1 min. The photoresist was then baked at 95 $^{\circ}\text{C}$ for at least 3 min. (twice as long as suggested by the manufacturer) to ensure that the solvents evaporated from any accumulations of photoresist. This process

resulted in little photoresist excess near concave corners and an even coating near convex corners.

The photoresist was exposed to a dose of 720 mJ/cm^2 of 365 nm UV light (Karl Suss MJB3). This is nearly 10 times the dose recommended by the manufacturer for a $1.8 \text{ }\mu\text{m}$ layer of photoresist, but such a high dose had to be used to fully expose the photoresist on the sidewalls (which is in a film parallel to the UV light rays) as well as remaining photoresist accumulations. The high UV dose, combined with the $50 \text{ }\mu\text{m}$ gap between the substrate floor and the mask, translated into poor pattern transference from the mask to the substrate. Ample spacing between features was prevented unintentional electrical connections, and ensured the continuity of the intentional connections.

The microfluidic channels to the vial traps were fabricated in two different ways. The channel in the floor-ground device was formed by cutting double-sided adhesive tape (Permanent double sided tape, Scotch, 3M), with a thickness of $125 \text{ }\mu\text{m}$, into the shape of the channel and adhering it to a plastic cover into which two holes had been drilled and tubing ports had been glued beforehand. The channel in the ceiling-ground device was formed by patterning $100 \text{ }\mu\text{m}$ thick SU8-50 on the floor substrate. The channel was covered with a glass slide with indium-tin oxide (ITO) on it (Structure Probe Inc.), which served as the ground electrode. The ground electrodes were patterned by etching the ITO in 1:1 HCl:DI water solution. Two holes were drilled in the glass slide, and tubing ports were glued to it. The glass slide was aligned to the bottom substrate, and the two were

fixed together using UV curable glue (Loctite 3108, Henkel).

4.6.3 DEP Experimental Procedures

The cells used in this study were dead yeast cells (Fleischmann's, ACH Food Companies, Inc), killed using methanol. Dead yeast cells show positive and negative DEP at different frequencies, and there is more certainty about their frequency response than that of live yeast cells (when working with live yeast, inevitably some will be dead, resulting in undesired response. This was avoided by killing all the cells instead.) The solution was prepared by dissolving 20 mg of dry yeast pellets in 50% methanol, 50% water at 33 °C. Methylene blue solution (0.6 mg/ml) was added 10 min. later, and 40 ml of DI water was added 10 min. after that. The solution was kept at 33 °C and used between 50 and 120 min. after preparation.

The inner electrodes were excited at 5 kHz, which attracted the cells, and the outer electrodes were excited at 5 MHz, which repelled the cells, using function generators. The voltages were always applied before the cell solution was introduced into the channel. The impedance between the electrodes of the floor-ground vial trap device was so small that the function generator voltage was limited to 5 V_{RMS}.

The tubing ports on the devices were connected, via vinyl tubing, to a syringe pump (NE-1000 New Era Pump Systems, Inc.) and to a reservoir containing the yeast cell solution. Flow was induced through suction, because applying positive pressure would rupture the channel. To prevent air bubbles, the channel was flushed with ethanol, which wetted the

inside of the vials, followed by DI water prior to introducing the cell solution.

The flow velocity was measured by analyzing video captured during the experiments.

The flow velocity was calculated using the time that it took for a cell (not flowing close to DEP electrodes) to travel a known distance.

Chapter 5 Cell Loading Device

In previous chapters I described how cells can be manipulated using two types dielectrophoretic devices: flow-through sorters and MFDEP vial traps. In this chapter I present a device design that employs these devices to load cells in its cages. This loading device may eventually be integrated in the cell clinics chip.

Integrating cell loading devices with the cell clinics chip is challenging because there are several interlocked aspects and if any of them fails the entire system may fail. The integration requires insight on every component of the system to ensure that they do not interfere with each other; and it requires time and the proper execution of immature fabrication techniques (i.e., patterning photoresist on top of the vials and MEMS and fabrication of MEMS on post-foundry CMOS chips) for the cell clinics system to work correctly. This chapter is aimed at easing the integration task. This chapter presents a discussion of issues to be considered during the integration and a description of the cell loading device and its expected characteristics.

5.1 Cell Loading Device Prototype

I fabricated and tested a prototype of the cell loading device to demonstrate some of its working principles and to expose problems that invariably arise when the first generation of a device is used. The prototype, shown and illustrated in Figure 5-1A,B, consisted of a microfluidic channel network, flow-through sorting electrodes that steer cells within this

network, and an array of 12 vial traps, which have their ground electrode on the ceiling of the channel. The vial traps have the same dimensions, and they are arranged the same way with respect to each other, as the vials in the cell clinics chip.

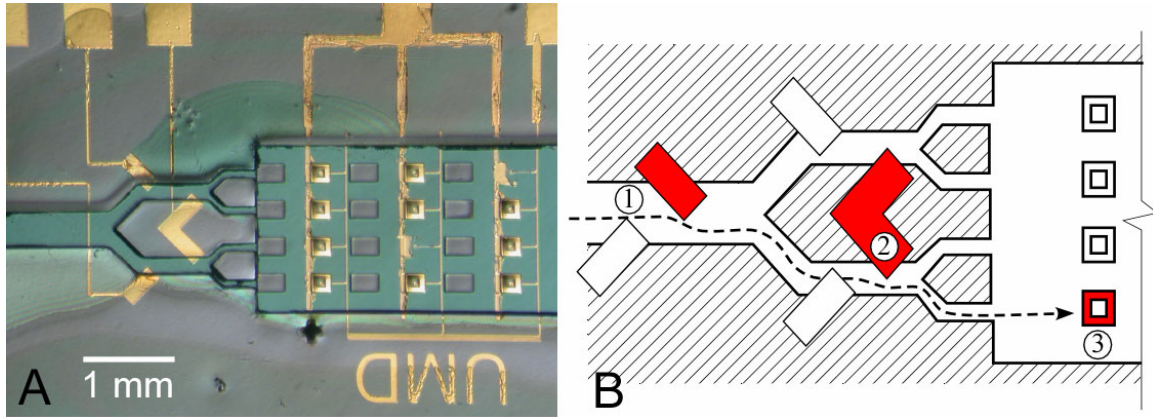


Figure 5-1. A) Picture of the prototype of the cell loading device. B) Illustration of its operation.

This cell loading device uses an external pump that moves a solution with cells along the microchannel network. The steering of cells through the microfluidic network is done by two-levels of flow-through sorting electrodes. An exemplary cell path is illustrated in Figure 5-1B by the dashed line; the cell path is affected by activating the electrodes highlighted in red. The channel is subdivided in two and the first level of sorting electrodes toggles cells between each of these subdivisions (1). Each of these channel subdivisions divide again in two (for a total of four subdivisions), and the second level of sorting electrodes toggles cells between these four channels (2). Each of the four channels is aligned with a row of vials outfitted with the vial trap discussed in Section 4.4.3, such that when a cells flows out one of these channels it will flow above the vials in that row (3). In the prototype the all the vial traps are electrically connected together,

so one vial trap cannot be turned on individually from the others.

The cell loading device was tested using yeast cells. The vial traps worked as designed, as discussed in Section 4.4.3. However, at first, the flow-through sorters were unable to steer cells within the microfluidic network, and this led to the flow-through sorters and the vial traps to be demonstrated separately.

The reason for the initial failure of the sorting electrodes is that in the beginning the ceiling electrode material was ITO, because its transparency would allow visual monitoring of the experiment. However, I found that the ITO electrodes had a resistance of $10\text{ k}\Omega$ (measured) between the region that connects to the function generator and the region in the channel, and this resistance is much higher than the impedance of the channel, $500\ \Omega$ (estimated) at the signal frequency. This means that the voltage across the sorting electrodes was much smaller than originally expected, and thus the maximum sorting speed ($U_{max} = 160\text{ nm/s}$) was too small for the sorting forces to be noticed.

Later on I demonstrated the influence of the sorting electrodes by increasing the voltage at the sorting electrodes using a transformer. The transformer increased the function generator voltage from $< 10\text{ V}_{\text{RMS}}$ to $\sim 250\text{ V}_{\text{RMS}}$. However, the transformer, comprised of two inductors magnetically coupled, filtered high frequency signals and therefore it limited the experiments to using only live yeast cells, which are repelled at 5 kHz , which is low enough for it not to be filtered by the transformer. Live yeast cells do not always

have the frequency response that I would expect, because their state influences their frequency response and their state is dependent on their preparation (unlike dead yeast cells, whose state does not change and thus their frequency response is more consistent than live yeast), therefore experimental results were not repeatable. In addition, the ITO degraded quickly (in matter of seconds) and would be rendered insulating when using high voltages for reasons unknown to me.

Later on I demonstrated the operation of the sorting electrodes using evaporated aluminum as the electrode material. Aluminum electrodes meant that the voltage between the sorting electrodes could be as large as the function generator could deliver, and thus the transformer was not needed. Not using the transformer enabled me to use 5 MHz signals, and this in turn enabled me to use dead yeast cells, leading to more consistent results. Figure 5-2 shows dead yeast cells being affected by a pair of aluminum electrodes (one on the floor and one on the ceiling of the channel) demonstrating the steering of cells within the microfluidic network. The ceiling electrode aluminum film was thin enough for it to be somewhat transparent, revealing cells under it that were attracted by the electrode.

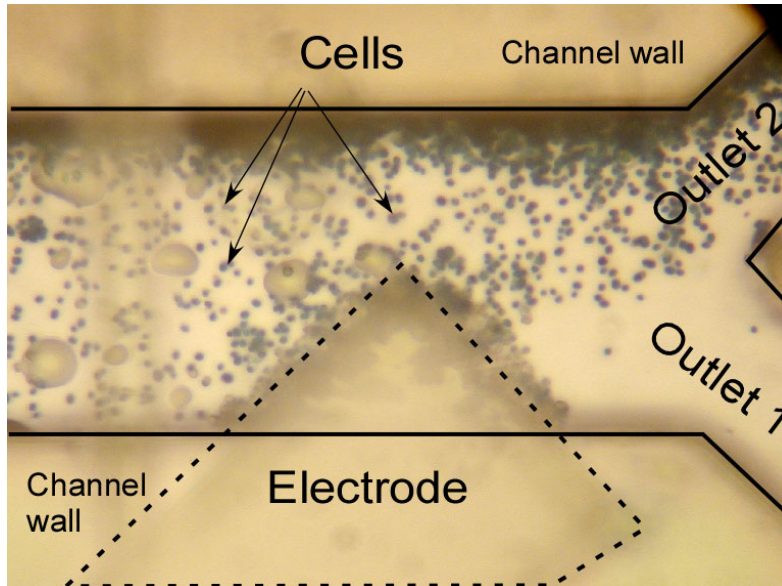


Figure 5-2. Dead yeast cells steered to one of two channels by a pair of sorting electrodes (only one is visible) excited at 5 kHz, 8 V_{RMS}.

Another problem that the prototype presented was that the features that subdivided the channel, highlighted with dashed lines in Figure 5-3, had the tendency of delaminating and then blocking the channel. The device channels were made of SU8, and I later learned that SU8 has known adhesion problems with silicon and silicon dioxide when water is present (personal communication with S. Patil, Laboratory for Microtechnologies). The delamination was more likely during rinsing steps, perhaps due to fluid shear forces on channel walls since during rinsing flow may at times have reached speeds as high as 1 cm /s.

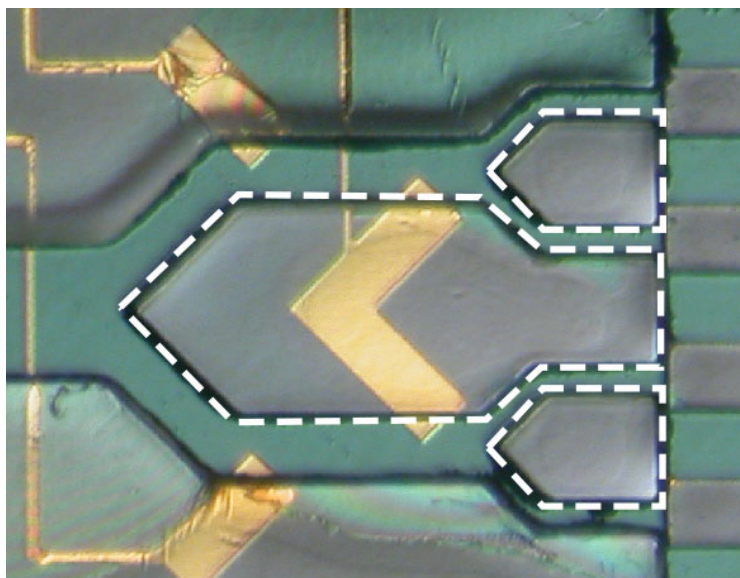


Figure 5-3. Features in the microfluidic network that had the tendency to delaminate.

The prototype provided valuable lessons. Based on these lessons I designed an improved cell loading device which is discussed in the next section.

5.2 Design of Cell Loading Device for the Cell Clinics Chip

Figure 5-4 illustrates the recommended cell clinics chip integration with the cell loading device. The cell clinics chip (red) should be packaged using an approach that enables integrating it with a microchannel (dashed lines). An appropriate packaging approach is discussed in section 5.2.1.2. The microchannel (discussed in section 5.2.1.3) will work with dielectrophoresis to manipulate cells in a similar way as the prototype device does, but in this design it consists of a single channel, it is not subdivided. The dielectrophoretic manipulation involves cell routing (section 5.2.2.3) and focusing

(section 1.2.3) (light green electrodes) and MFDEP vial traps (section 5.2.2.2) (dark green) to bring cells into the vial.

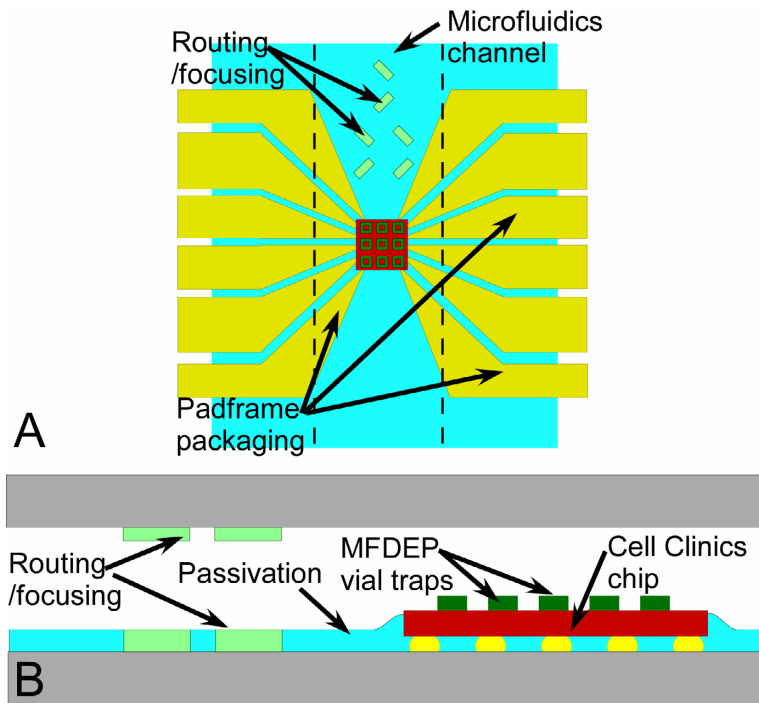


Figure 5-4. Top view A) and side view B) of the recommended cell clinics chip configuration integrated with microfluidics and cell loading capabilities.

The operation of the loading device is illustrated in Figure 5-5 and it is similar to the operation of the prototype device, but it also includes focusing electrodes (their justification is explained in Section 5.2.2.4). An exemplary cell path is illustrated in Figure 5-5 by the dashed line; the cell path is affected by activating the electrodes highlighted in red. The cell is initially at an arbitrary position in the channel. Focusing electrodes move the cell to the middle of the channel span and height (1). The first level of sorting electrodes toggles cells between either one of two paths (2), and then the second level of sorting electrodes aligns the path of cells to one of four vial rows (3).

Before cells reach the vial traps section, their path height is adjusted by a second set of focusing electrodes (4), and then cells are loaded into the desired vial by the vial trap (5).

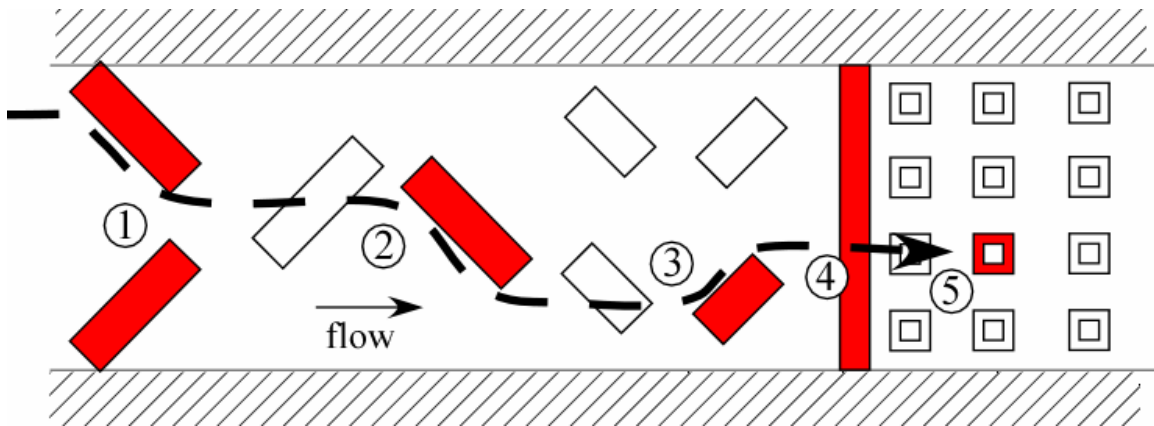


Figure 5-5. Illustration of the operation of the cell loading device design to be integrated with the cell clinics.

5.2.1 Cell Clinics Chip Components

There are a few requirements on the chip which, though not directly related to dielectrophoretic components, are necessary for the cell loading device to work as designed. This section discusses these requirements.

5.2.1.1 Integrated Circuit Chip

Ideally, the integrated circuit chip would generate the signal used by the dielectrophoretic manipulation, otherwise external function generators are required and this would make the cell clinics system larger and less portable than it could be. The chip should be capable of operating at voltages of up to 50 V_{RMS} (+/- 70 V_{amplitude}), which is the highest

voltage required by the dielectrophoretic cell manipulation, used by the cell routing and focusing (their design and requirements are given in detail in sections 5.2.2.3 and 5.2.2.4).

If the signals are generated on the chip, it is the case that square waveforms have well established ways to be generated and they require less chip layout area than generating a sinusoidal waveform (personal communication with D. Sanders, IBIS). The shape of the waveform affects the Clausius-Mossotti factor response, and so I considered the effect of using a square waveform when compared to a sinusoidal waveform. A square wave (as well as any arbitrary function) can be represented by the infinite sum of its Fourier terms [188]. Therefore, the Clausius-Mossotti factor for a square wave can be found using multiple frequency dielectrophoresis theory [146] by decomposing the signal at each frequency into its sinusoidal terms and adding the individual effects of each of them (given their relative amplitude in the Fourier series) to find CM_{eff} .

Figure 5-6 shows the real part of the Clausius-Mossotti factor for a sinusoidal waveform and CM_{eff} for a square waveform (calculated using the first 13 terms of its Fourier series) for PC-12 cells. CM_{eff} for the square waveform has slightly lower values in regions where it changes values, compared to CM for the sinusoidal signal. This is to be expected since higher order terms, which have higher frequencies, shift the CM_{eff} curve towards the values of CM at these higher frequencies. The curve is shifted up if there are higher values of the Clausius-Mossotti factor at higher frequencies, and down if there are lower values at lower frequencies, and since CM_{eff} is bound between fixed values then

these shifts show themselves as lower values at regions in which CM_{eff} changes. At the lowest ($< 10^5$ Hz) and highest ($> 10^9$ Hz) frequency ranges shown, where CM_{eff} does not change (and thus higher harmonic terms have the same CM value as the lower harmonic terms), the square and sinusoidal signals produce the same response.

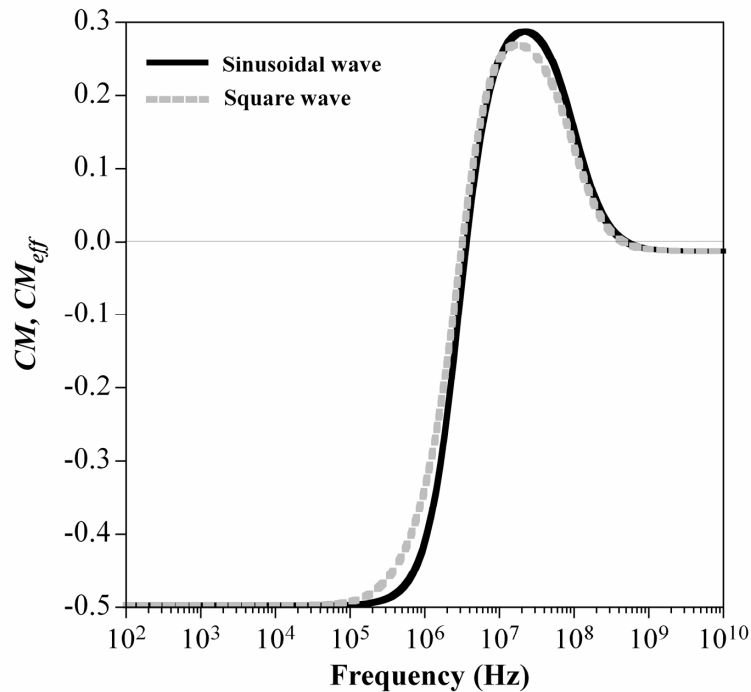


Figure 5-6. Real part of the Clausius-Mossotti versus frequency for PC-12 cells under sinusoidal and square waveforms. Clausius-Mossotti factor calculated using a single-shell model [41] and published cell properties [7].

5.2.1.2 Packaging

The current packaging configuration of the cell clinics chip, shown in Figure 1-7, is not integratable with microfluidics. This packaging configuration only provides access to the chip from the top. In the future the cell clinics system will be integrated with

microfluidics so that cells can be loaded using the approach presented in this dissertation and to automate the supply of nutrients and stimulants to the chip in a configuration that can be placed in a handheld device. A novel packaging approach is being pursued at IBIS and the Laboratory for Microtechnologies that will enable microfluidics integration with the cell clinics chip.

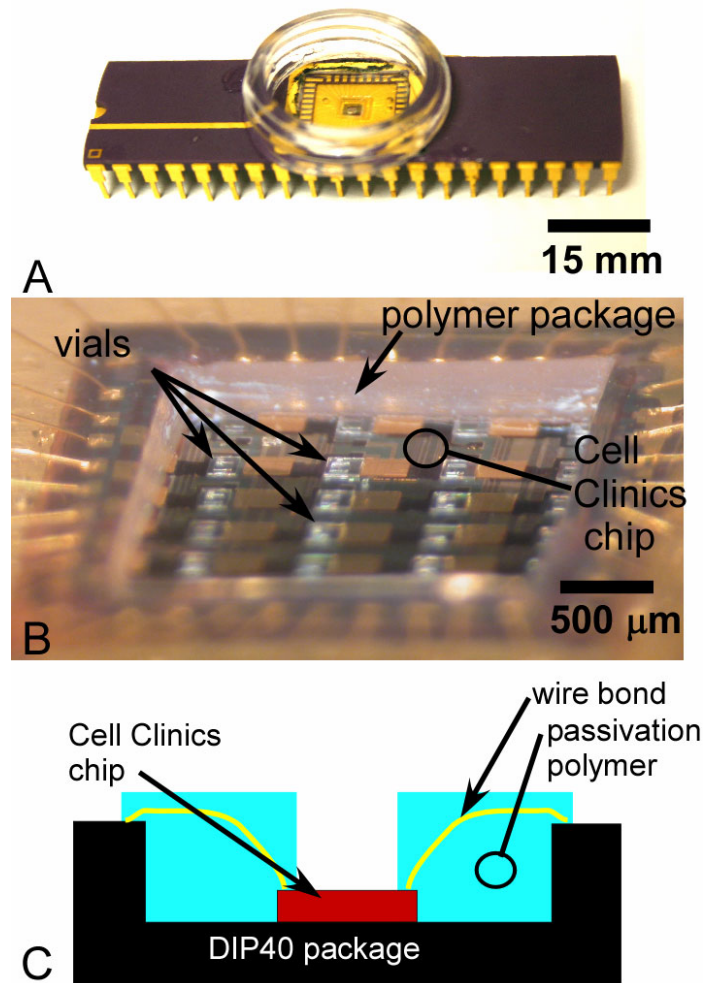


Figure 5-7. A) The current configuration of the cell clinics chip uses a DIP40 B) and a custom polymer package around the wirebonds. C) Cross section schematic of current packaging solution.

The packaging approach was conceived by E. Smela, M. Dandin, and P. Abshire, and under development by M. Dandin. This packaging scheme is sketched in Figure 5-8. In this scheme the electrical pads on the CMOS chip are left covered by the chip passivation layer, which is normally removed above the pads so that they can be wirebonded to the

package from the top surface. Holes are drilled on the back of the chip using deep reactive ion etching (DRIE) [159]. This step is followed by passivation of the hole sidewalls, and by filling the hole with gold electrolessly plated on the aluminum pad. The gold, which is an electrical contact extending from the electrical pad to the back of the chip, is bonded to a pad frame. The pad frame can be wirebonded to different kinds of packages, and the package to be used is yet to be defined. The electrical leads on the pad frame and the space under the chip will be covered with a passivation layer, yet to be defined, so that cell solution does not short-circuit the electrical leads. With this scheme, the wirebonds are moved away from the chip so that a microchannel can pass between them to access the channel.

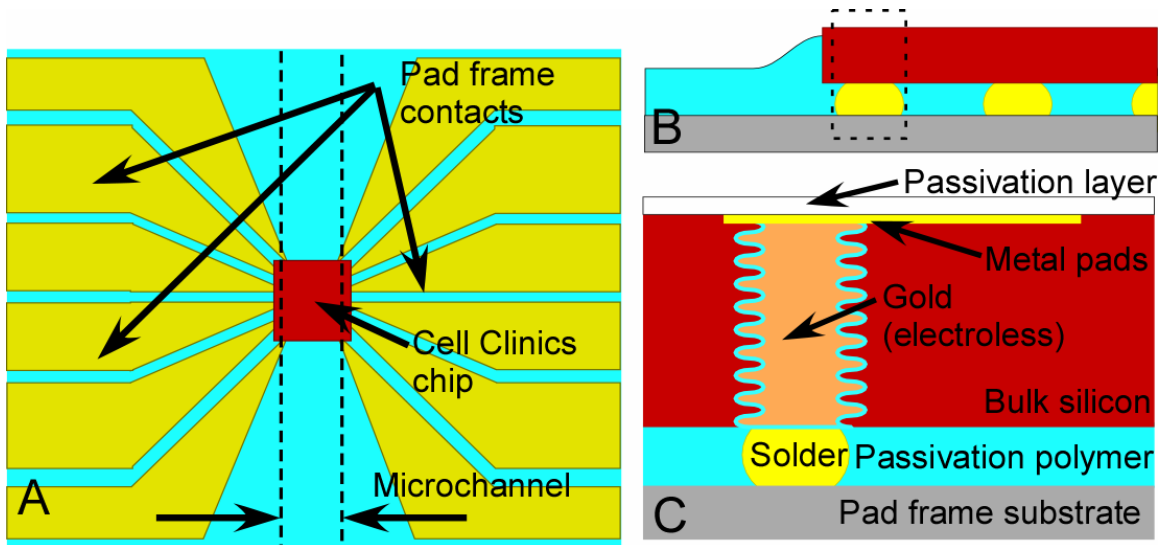


Figure 5-8. Packaging scheme under development by M. Dandin. A) Top view, B) partial side view, and C) cross-section detail of pad and back-side connection.

5.2.1.3 Microchannel

It is necessary that the channel is tall enough to allow the cell clinics vial lids to open.

Figure 5-9 shows a sketch of a vial with its lid closed A) and open B). The bi-layer hinge responsible for opening and closing the lid bends at a constant curvature [179], and when the lid is closed it must rest on top of the vial and parallel to the floor; at this position the lid has turned π radians from its fully open position. The bi-layer hinge length, L , can be found through the geometry at the close position (Figure 5-9A), and since the bi-layer does not change its length, one can use the value of L to calculate the highest point of the lid as it swings open by finding the radius of curvature, R , when the hinge has turned $\pi/2$ radians (Figure 5-9B) given an arch length L . Given that current Cell clinic vials are $50 \mu\text{m}$ tall and the lids are $200 \mu\text{m}$ long [179], then the tip of the lid reaches up to $250 \mu\text{m}$ from the floor as it opens. The channel must have at least that height so that lid operation is not impeded. Since the flow speed that is allowed by the sorting electrodes is higher at lower channel heights then I recommend the height of the channel to be $250 \mu\text{m}$.

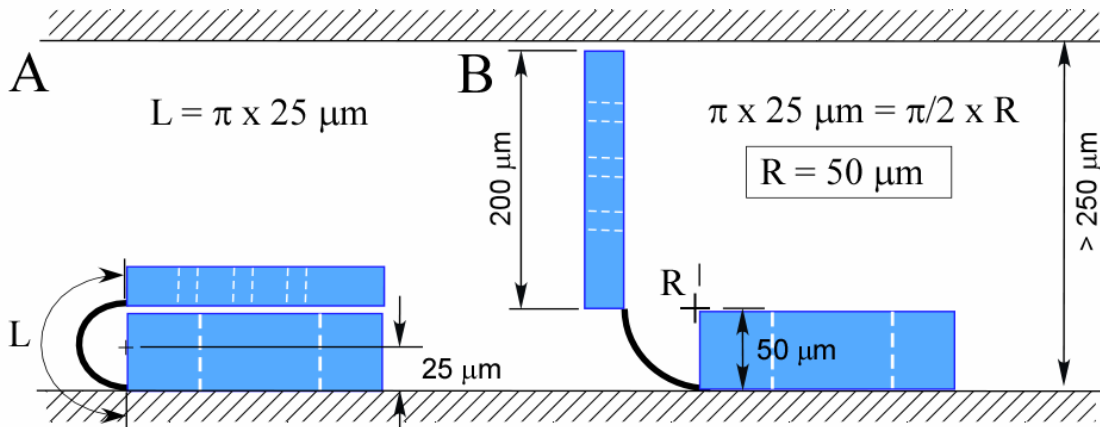


Figure 5-9. Cell clinic vial with its lid closed A) and open B).

In Section 5.1 I described how the microfluidic network was ruined when SU8 structures delaminated from the substrate; based on this experience I recommend using a different material. I recommend using polydimethylsiloxane (PDMS) which is a material often used in microfluidics [189-195] and it has no reported adhesion problems.

The trajectory of the cells can be controlled using flow-through sorters even if the channel is as wide as the entire chip. Therefore I also recommend forgoing the structures that subdivide the channel, since they are not strictly required.

5.2.2 Dielectrophoretic components

5.2.2.1 *Cells and Cell Media*

The particles that I used demonstrate the functioning and working principles of the devices presented are yeast cells. Yeast cells are readily available at the groceries stores and they are easy to maintain, compared to mammalian cells, which require significant time and effort (personal communications with N. Nelson, IBIS). Since I wanted to focus on the devices this made yeast cells the appropriate choice of cells. However, the cell clinics chip is undergoing testing using PC-12 and bovine aortic smooth muscle cells and the question of whether cell loading is possible using these cells arises.

The devices presented work the same way regardless of the body being moved. Whether the bodies are polystyrene beads, live, or dead cells, the functioning of the device is not

affected as long as the proper fluid drag and dielectrophoretic attractive and repulsive forces can be generated. Differences in the Clausius-Mossotti response of different bodies can be addressed by simply using different frequencies and signal amplitudes such as the direction and magnitude of the dielectrophoretic forces is as desired.

Figure 5-10 shows the real part of the Clausius-Mossotti factor as a function of frequency for PC-12 cells for various medium conductivities calculated using a single-shell model [41] and published cell properties [7]. Though the electrical properties of bovine aortic smooth muscle cells have not been published or measured by me, I expect that their resulting Clausius-Mossotti response to be similar to that of PC-12 based on the fact that disparately different living cells (yeast [84], PC-12 cells [7], breast cancer [95], and various kinds of blood cells [89, 95]) all have a similar response that differ only within certain frequency ranges, and they have a similar dependence with medium conductivity [59]. In general, when the medium conductivity is above a certain value (0.7 S/m for PC-12 cells) the Clausius-Mossotti factor no longer takes positive values. Therefore low conductivity solutions should be used. On the other hand, cells are damaged if they are in solutions of conductivity below a certain value [7]. Thus, the cell medium must be carefully selected such positive dielectrophoresis is possible and at the same time cells are not harmed.

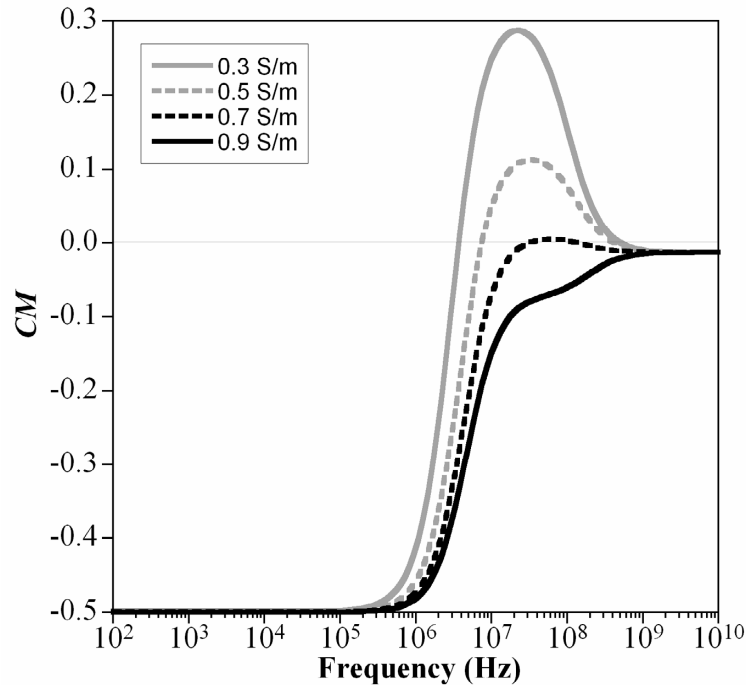


Figure 5-10. Real part of the Clausius-Mossotti factor as a function of frequency and solution conductivity for PC-12 cells.

Typical cell media have conductivities in the order of 1 S/m. Whether diluted solutions, such that they have lower conductivities, can be used with cell types of interest to the cell clinics project without harming them is yet to be determined because some cells are more delicate than others. We know that olfactory sensory neurons, which are of particular interest to the cell clinics project in the future, are known to be quite delicate (personal communications between Prof. G. Ronnett, Johns Hopkins University, and Prof. E. Smela, Laboratory for Microtechnologies) and is likely that they would be harmed if in diluted cell media. However, the cells currently being used in the cell clinics project, PC-12 cells, cultured in cell medium diluted to have a conductivity of 0.3 S/m have been found to display similar viability after 24 and 48 hours to cells cultured in undiluted cell

medium [7]. At such medium conductivity PC-12 cells to have positive Clausius-Mossotti factor at frequencies between 10^6 and 10^8 Hz, as it is shown in Figure 5-10. Figure 5-10 also shows that positive values of the Clausius-Mossotti factor are lower for higher solution conductivities, with no positive values for solution conductivities above 0.7 S/m.

I recommend using yeast cells to test and characterize the cell loading device unless other cell types are necessary. If electrically active cells, such as PC-12 are needed, then I recommend using PC-12 cells with cell media conductivity adjusted to 0.3 – 0.7 S/m. Lower solution conductivity values are preferred since they result in higher positive values of the Clausius-Mossotti factor values which and this leads to lower voltages required to attract cells into the vials.

Another aspect to consider is the transmembrane potential elated by the electric field. If this potential is above 1V (across the membrane) the membrane may undergo electrical breakdown and rupture [196]. The transmembrane potential can be calculated by [196]

$$(33) \quad V_{transmembrane} = \frac{1.5RE \cos(\beta)}{\sqrt{1 + (2\pi f \tau)^2}}$$

where β is the angle between the membrane site and the electric field direction, and τ is the relaxation time of the membrane. This relaxation time constant is $\tau =$

$R \cdot C_{membrane}(\rho_{interior} + 0.5\rho_{exterior})$, where ρ is the resistivity and C is the membrane capacitance, and a reasonable value is 227.7 ns. By approximating the electric field

between the vial trap electrodes a constant value of $5 V_{\text{RMS}}/100 \mu\text{m} = 5 \times 10^4 \text{ V/m}$, then the transmembrane potential is estimated at 215 mV. This suggests that there is no risk of harming the cell.

5.2.2.2 *MFDEP Vial Trap*

The vial traps were discussed in detail in Chapter 4. I showed two configurations, one in which the ground electrodes is on the floor and one in which the ground electrode is on the ceiling. While the ceiling-ground vial traps are able to load cells within a larger height window, they do not perform well when the channel height is greater than 100 μm . This is because the ground is so far from the inner and outer electrodes that they do not interact with it as much as needed. Given that the channel height is 250 μm , the ground electrode should be on the floor. In Chapter 4 I showed cells loaded at speeds of $\sim 50 \mu\text{m/s}$ when the ground electrode is on the floor and the channel height is 100 μm . Figure 5-11 shows particle tracing simulations results for a tall channel (the actual channel height is 200 μm , but I found little height dependence for channels taller than 100 μm) at bulk flow speeds of 100 $\mu\text{m/s}$, thus cell loading at this speed can be expected.

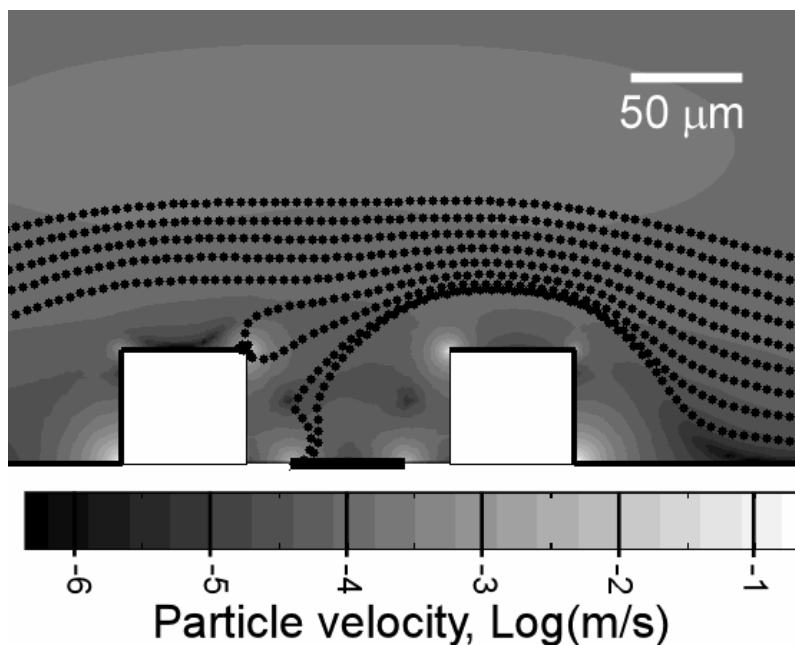


Figure 5-11. Particle tracing simulations of a MFDEP vial trap in a channel 250 μm tall (only 200 μm shown) with 100 $\mu\text{m}/\text{s}$ bulk flow speed. The inner electrode (at 7 V_{RMS}) is located inside the vial, the outer electrode (at 5 V_{RMS}) on top of the vial and on the outer sidewalls.

I fabricated vial traps on the current version of the cell clinics chip (which was designed by S. Prakash, IBIS) to show that it is possible to integrate them with CMOS. The chip and the detail of a vial trap are shown in Figure 5-12. The vial trap ground was on the floor. The floor electrode pattern was the same as the devices discussed in Section 4.4.2, which were designed specifically to imitate the CMOS chip electrode pattern. The external electrodes were deposited using the same method discussed in Chapter 4, but the electrode interfaced with CMOS electrodes on the chip surface, instead of using electrical leads fabricated at the same time as the rest of the device to interface with the function

generator. The electrodes inside the vial (inner electrodes) were part of the CMOS chip and I fabricated the vials around them. The signals on the dielectrophoretic electrodes were generated using external function generators and sent to the CMOS electrodes through the chip circuitry. In addition to the same fabrication challenges associated with fabricating the dielectrophoretic vial traps (discussed in Appendix A), there were additional challenges associated with fabricating MEMS on top of CMOS chips [197]. After fabrication of the vial traps the chip was wirebonded to a DIP40 by N. Nelson, IBIS, and packaged by me using the method presented in [162].

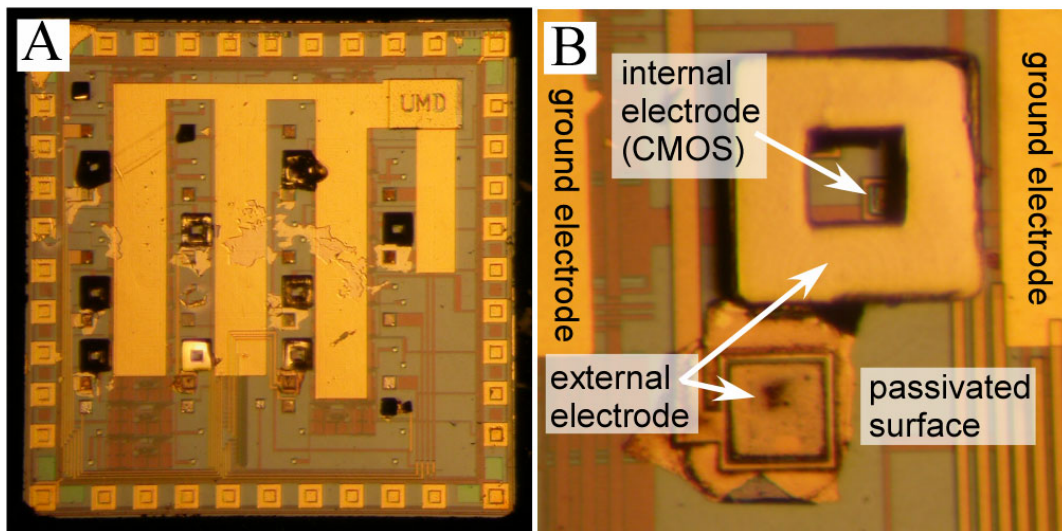


Figure 5-12. Dielectrophoretic vial traps fabricated on a bio-amplifier cell clinics chip. A) Overhead view of the unpackaged chip. B) Detail of one of the vial traps.

I attempted loading cells using this chip. Figure 5-13 shows a picture of the experimental set-up. I placed a solution containing dead yeast cells on the chip, and cells close to the vial entrance went inside the vial as they were settling onto the chip. The chip was

operated by S. Prakash, because addressing each of the electrodes on the chip requires knowledge on the chip design and functioning. The inner and outer electrodes were stimulated using external function generators, but the signals were limited to $6 V_{\text{peak-to-peak}}$ ($\pm 3 V_{\text{amplitude}}$) because of chip voltage limitations [198]. While many cells entered the vials, I cannot conclude that they entered only because of dielectrophoresis since gravity would bring those cells initially above the vial into it anyways. However, this exercise was successful by demonstrating the possibility of integration with CMOS.

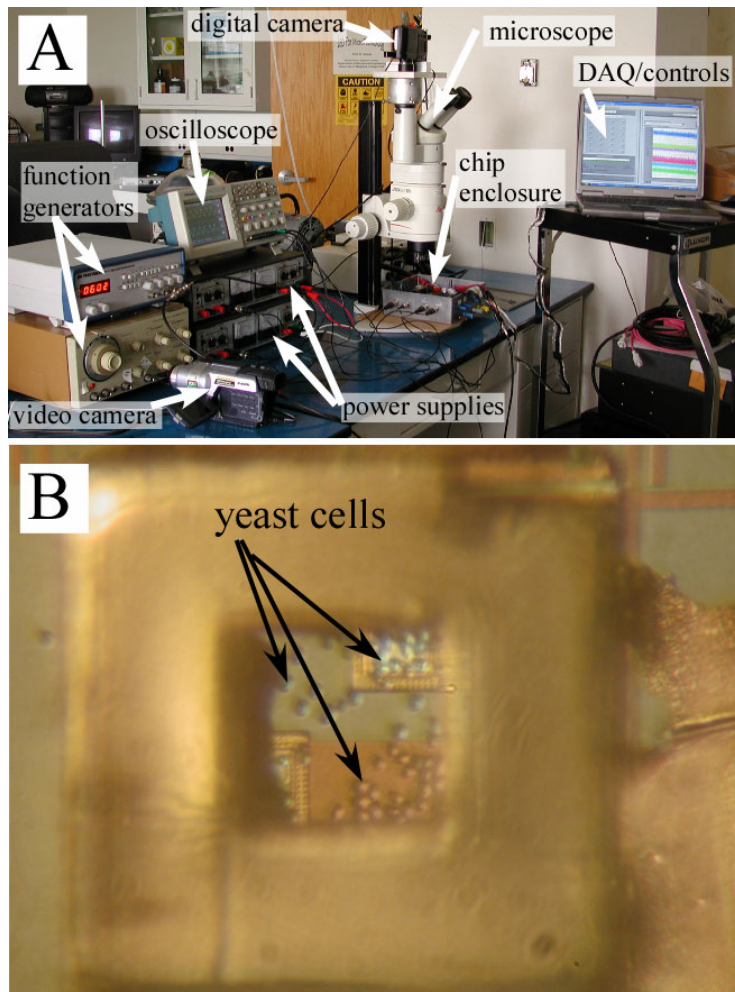


Figure 5-13. A) Experimental set up of the CMOS/MFDEP vial trap chip. B) Yeast cells inside one of the vials.

5.2.2.3 Cell Routers

Cells need to be routed within the channel so they flow above the vials in which they will be loaded. I recommend using flow-through sorters because their fabrication is simple, it only requires a pair of electrodes, and their control, which consists only on on-off, could be handled by the chip. In addition, using the design approach presented Chapter 2, their design is straight forward.

I showed in Chapter 2 that flow-through sorters of geometry A (an electrode on the floor of the channel mirrored by an electrode on the ceiling) have the highest maximum operating flow velocity of the geometries presented, *ceteris paribus*. Thus, I recommend using sorting electrodes of geometry A to minimize the excitation voltage required. For this geometry, the highest flow velocity allowed is reached when $w' \geq 1$, or $w \geq h$, therefore given a channel height of $h = 250 \mu\text{m}$ then the electrodes should have a width of $w \geq 250 \mu\text{m}$.

The angle α that the electrodes make with the flow affects the loading time, but this relationship is not straight forward. If $\alpha \sim 0^\circ$ (electrode edge nearly parallel to the flow direction) U_{max} reaches the highest values possible, because U_{max} varies with $1/\sin(\alpha)$. On the other hand, the streamwise length of the electrodes, which varies as $1/\tan(\alpha)$, becomes very large. The time that a particle spends in the region of the channel should be minimized to maximize cell the sorting rate, as I will explain shortly. This time is

proportional to the streamwise electrode distance divided by the flow velocity, resulting in a $\cos(\alpha)$ dependence and this points to $\alpha \sim 90^\circ$ as an optimal value. Nevertheless, for such angles the cell motion perpendicularly to the flow, which varies as $1/\cos(\alpha)$, is very slow, and since the cell must travel a certain distance perpendicularly to the flow so it is aligned with the vial rows, then $\alpha \sim 90^\circ$ will also result in large sorting times. We can see that the electrode angle affects the electrode length, the flow speed, and the speed perpendicular to the flow, all of which need to be optimized at the same time to yield the shortest possible sorting time. Since either extreme values of α result in high sorting times then I recommend to use $\alpha = 45^\circ$ until a more exhaustive study suggests a better value.

Figure 5-14 shows a plot of U_{max} , given cells $10 \mu\text{m}$ in diameter in DI water, $\text{Re}(CM) = 0.5$, and $\alpha = 45^\circ$, as a function of electrode voltage. This curve was obtained using the methodology presented in Chapter 2. As discussed before, the vial loading flow speed is $< 100 \mu\text{m/s}$. I recommend using $U_{max} = 50 \mu\text{m/s}$ since I have demonstrated experimentally cell loading at such flow speeds. For this flow velocity, the electrode voltage should be no lower than $11 \text{ V}_{\text{RMS}}$ ($\pm 15 \text{ V}_{\text{amplitude}}$) (point *a* in Figure 5-14).

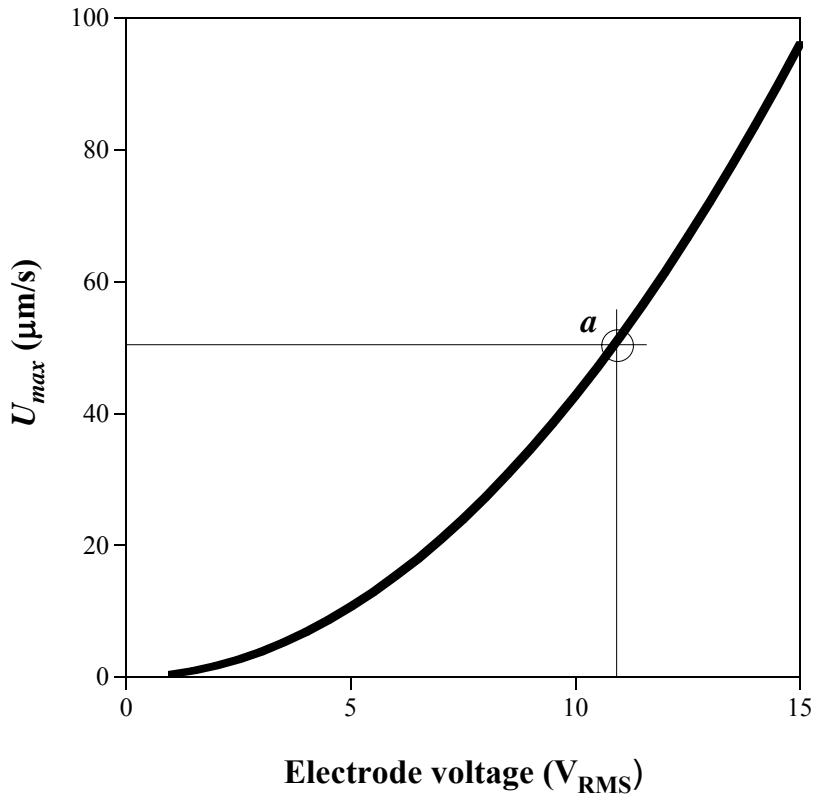


Figure 5-14. U_{max} for the routing section of the loading device as a function of electrode voltage.

I recommend using the two-level routing electrode configuration used in the prototype (Section 5.1), which was illustrated in Figure 5-5.

One of the requirements for the cell loading device is a loading time of minutes. I will assume the following condition to estimate the loading time: for two cells flowing one right after the other to be loaded in different vials, they must be far apart enough such as one does not enter the channel region with a set of routing electrodes until the other one has left it, otherwise the trajectory of each cell will be affected by the activation, or lack

thereof, of the electrode. This condition addresses the most challenging loading scenario, in which different types of cells are present in the solution and only certain types of cells should be loaded into specific vials.

The electrodes are $250\ \mu\text{m}$ wide and form 45° with the direction of the flow, therefore the channel region with electrodes is $(250\ \mu\text{m})/\cos(45^\circ) = 353\ \mu\text{m}$ in streamwise length.

Given a flow speed of $50\ \mu\text{m/s}$, cells must flow 7 seconds apart to comply with the only-one-cell-in-the-electrode-region condition. Assuming that 10 cells will be loaded in each of the 24 vials of the cell clinics chip, a total of 240 cells are to be sorted. If only one set of flow-through sorters is operated at a time, then it would take 28 minutes to load 240 cells. However, the sorters at the second level can operate in parallel, independently of each other, and this means that cells can be loaded in half the time, 14 minutes. (First level sorting electrodes are not a bottleneck to the routing process because two cells can be allowed to be present in the electrode regions at the same time. This can be tolerated because the resulting sorting errors could be corrected by the electrodes in the second level.)

The only-one-cell-in-the-electrode-region assumption represents the worst case scenario, since it implies that a specific cell flowing along the channel will be loaded into a different vial, along a different row, than the next cell. In reality, it is more likely that at any one time any of the cells in the solution can be loaded into any of the vials. The more flexible the sorting requirements, the faster that cells can be loaded. If the cells that need

to be loaded are in different solutions, then the loading process would involve alternating flowing one solution with cells and flushing the channel to remove cells not loaded into vials before the next solution with cells is introduced. In this case, loading times will be different than reported. Since any of the cells in each of the solutions can be loaded into any of the vials, then sorting is not warranted, instead cells can flood the area with vial traps and each of the vial traps can be activated as long as needed to load in it enough cells. I demonstrated that several cells can be loaded into a vial in matter of seconds. In my experiments I estimate that I was able to load 10 cells into a vial in 10 seconds or less. After the loading step, the channel is flushed and the same method can be used to load subsequent types of cells. Faster flow rates can be used during the flushing step than during the loading step to reduce the flushing time. This method should result lower loading times than in the first scenario discussed.

5.2.2.4 Cell Focusers

Span Focusing

In the prototype presented in Section 5.1 cells initially traveled in a channel that is much narrower than the region where the vials lay and cells were to be sorted through the microfluidic networks. However, in the design to be integrated with the cell clinics, cells flow over the span of a channel that can be a few millimeters wide. Therefore, cells need to be centered before they are manipulated, so they have defined initial location and then their path can be controlled from there. A first set of focusing electrodes (Figure 5-5(1)) should be constantly activated producing negative dielectrophoresis to move cells

flowing across the entire span of the channel to the middle. The span focusing electrodes are similar to flow-through sorters in the sense that they are designed to prevent cells from crossing over the electrodes and they move cells along the plane parallel to the floor, therefore the same width (250 μm) and voltage (11 V_{RMS}) as the routing electrodes should be used.

Height Focusing

A second set of electrodes is needed to bring cells to a height at which they can be loaded into the vials. After cells are routed to the desired vial row by the routing electrodes, they travel along the channel mid-height, at 125 μm above the channel floor, because flow-through sorters of geometry A push particles to the middle of the channel (as explained in Chapter 2). According to the simulation results shown in Figure 5-11 only cells traveling at certain heights will go into the vial, and so cells must be focused to this height from the channel mid-height before reaching the vials.

Focusing the traveling height can be also done using a pair of electrodes producing negative dielectrophoretic forces. In focusing cells to a given height they need to be pushed up or down to a specific height, not to be prevented from crossing the electrodes (as is the case for sorting and span focusing electrodes), and cell in-plane trajectory must be left unchanged (because at this point cells have already been aligned with the vials by the routing electrodes). Thus, the design of this set of focusing electrodes is different to the sorting electrodes. For one thing, the electrodes must be perpendicular to the flow ($\alpha = 90^\circ$) so that the cell trajectory in the plane parallel to the floor remains unchanged

and only the traveling height is affected.

The dimensions and voltage of the focusing electrodes will depend on many parameters, including the voltages used to load the cells into the vials (because this affects the height windows in which cells need to be traveling for them to go into the vial). The design of these electrodes can be guided using the methods presented in Chapter 2. Modeling results of cell loading aided by the focusing effect produced by a 100 μm wide electrode at 50 V_{RMS} on the channel ceiling facing a 500 μm wide grounded electrode on the channel floor. The bulk flow speed is 50 $\mu\text{m/s}$, and $U_{\text{max}} = 35 \mu\text{m/s}$ (according to the method presented in Chapter 2 and the geometry and voltages modeled). The vial trap electrodes were excited at 5 (inner) and 3.5 (outer) V_{RMS} .

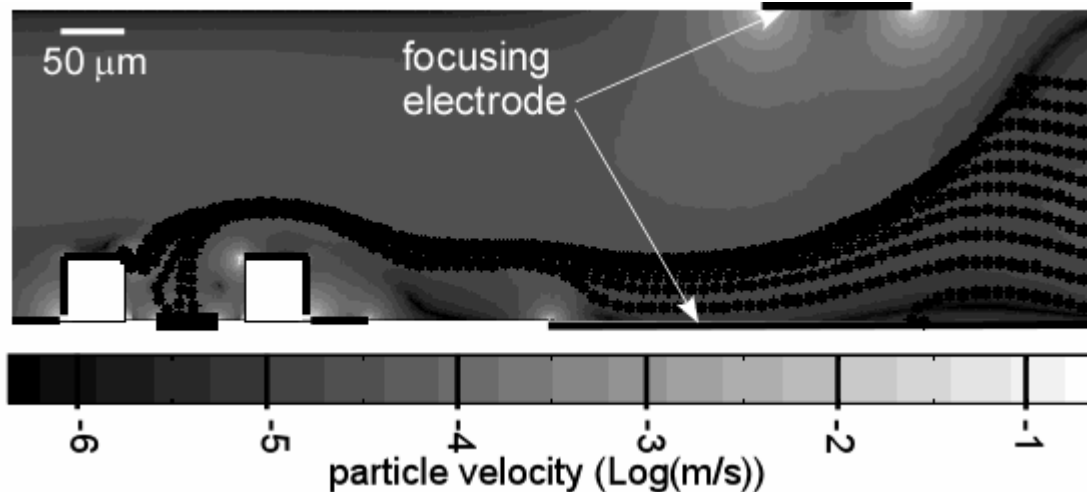


Figure 5-15. Particle tracing simulation results of the floor-ground vial trap loading aided by the effect of focusing electrodes.

5.2.3 Summary of the Cell Loading device

5.2.3.1 Loading Device Physical Specifications

Table 5-1 summarizes the physical specifications that the design presented will have. These values are based on the theory, models, and experiments presented in this dissertation.

Table 5-1. Physical specifications of the cell loading device design presented

Channel height:	250 μm
Electrode frequencies:	Positive DEP: $10^6 - 10^8$ Hz Negative DEP: $10^3 - 10^6$ Hz
Cell medium conductivity:	0.3 – 0.6 S/m
Maximum electrode voltage:	50 V_{RMS}
Maximum flow speed at the main channel:	50 $\mu\text{m/s}$
Time to load 10 cells in 24 vials:	Any cell into any vial: ~10 seconds Specific cell into a specific vial: 14 minutes

5.2.3.2 Loading Device Capabilities

- The loading device manipulates cells suspended in an aqueous solution and brings them into microvials
- The microvial in which cells are loaded can be selected using a series of flow-through sorter electrodes

- Integration with the cell clinics chip has been demonstrated.
- The method does not harm the cells it manipulates [55]
- The loading of cells can be controlled by the chip, by simply turning on and off electrodes. The signal necessary to produce the dielectrophoretic forces can also be generated on-chip.
- The loading device is expected to take 14 minutes or less to load 240 specific cells into specific vials and in the order of 10 seconds to bring any 240 cells into any of the vials.

Chapter 6 Conclusions

The goal of this dissertation was to design a device capable of loading individual cells suspended in a solution into microscopic vials and that can be applied to the cell clinics chip. Such a device is presented in Chapter 5. The different dielectrophoretic devices that make up this device have been demonstrated, either in this dissertation or on previous publications by other researchers. The work towards this dissertation focused on establishing the basis for fabricating the loading device. This was a challenge of on itself because one part of the theory to accomplish this did not exist before (multiple frequency dielectrophoresis) and the other was immature to the point that it needed to be processed before it was practical to use (flow-through sorter design).

It would be considered a limited success to only provide the exact dimensions of the loading device presented in Chapter 5 because the design would cease to be relevant if any of the many parameters involved changed for any reason. It is likely that there will be such changes because the cell clinics chip, though a reality today, it is still undergoing improvements and many of the factors that come into play in these improvements are not fully known. For example, vial and lid dimensions may vary to best accommodate different types of cells or cell consortia, the number of vials is likely to increase in future versions of the cell clinics chip, and the vial arrangement may change to optimize cell loading, circuit layout, or to facilitate chip packaging. Therefore it is more important to provide design concepts and tools that can be used to adapt a basic design than to give a device blueprint that would be rendered obsolete shortly after it is finished.

The loading design presented is flexible, because it can be applied to virtually any geometric variation of the cell clinics chip (different chip sizes or vial arrangements) and because it is scalable, so it can be used to load cells into one vial or hundreds of vials. The design is relatively inexpensive to fabricate and is integratable with the chip, so it could be implemented in the lab as well as in handheld devices. The loading approach can also be adapted to be used in other devices as well, such as [9-12, 177, 178]. The main fabrication challenges, patterning electrodes on top of the vial, were solved and vial trap fabrication was demonstrated on CMOS chips. Design methods were developed and used to give concrete device parameters, such as channel dimensions and electrode voltage. All the tools for subsequent contributors to make modifications and fabricate and use the cell loading device were provided. The combination of all these aspects makes the design successful and the contribution to the cell clinics project valuable.

It is true, however, that there are unresolved issues. It is possible that the cells of interest do not perform normally in solutions of conductivity low enough for positive dielectrophoresis, and packaging small CMOS chips to be integrated with microfluidics, on which the loading method presented relies, even though it is outside the scope of the dissertation, is still an unresolved challenge. Also, metal wires in the CMOS chip carrying signals may generate undesired DEP forces. Though this could be addressed in a variety of ways (i.e., placing the wires in the lowest metal layer possible, shielding the wires with metal films on top of the film, or active cancellation through MFDEP), it is difficult to subscribe to a solution in particular since so many factors are in play.

In this dissertation the manipulation of particles using dielectrophoresis was described and its content is likely to find applications in biotechnology and nanotechnology. These fields are cross-disciplinary fields and people working on them include biologists, medical doctors, physicists, chemists, and different kinds of engineers, to name a few. It would be unrealistic to assume that, as the end-users of the methods and devices presented, they would have expertise on dielectrophoresis. "Plug-and-chug" dielectrophoresis methods are likely to appeal to them, and my intention was to provide them with just that.

All the methods and approaches taken in this dissertation have the underlying theme of facilitating the implementation of dielectrophoresis. For example, the method to design flow-through sorters presented in Chapter 2 relies only on arithmetic and on the chart provided, and the approach presented to treat multiple frequency dielectrophoresis yields CM_{eff} , which can be applied to existing dielectrophoretic devices transparently. It took 4 years for the author to reach the expertise to come up with these contributions; now it takes five minutes to someone new to dielectrophoresis to design a flow-through sorter: my goal has been accomplished.

Scientific Contributions

The scientific contributions included in this dissertation can be summarized as follows:

- Dielectrophoresis in the presence of multiple frequencies was studied analytically, numerically, and experimentally. This subject was termed multiple frequency

dielectrophoresis, or MFDEP. In doing so, the effect of multiple frequencies coming from one or more electrodes was formalized through using an effective Clausius-Mossotti factor, CM_{eff} . This parameter is consistent with previous analysis of DEP forces and therefore builds on previous knowledge. This is an enabling technology that improves dielectrophoretic manipulation.

- For the first time different types of cells in different nearby locations in a single step using dielectrophoresis were patterned.
- A new method to design dielectrophoretic flow-through electrodes was created. The method simplifies significantly the design process, compared to the current approach. The method serves as a guideline, indicating the trends of the dielectrophoretic force that the electrode produce as a function of geometry.
- A novel method involving multiple frequency dielectrophoresis to actively cancel dielectrophoretic parasitic traps was used.
- For the first time, a device to load cells into vials using dielectrophoresis was demonstrated.

Appendix A. Challenges on Patterning Photoresist on and Around the Vials

This appendix describes the challenges associated with photolithography [159] when the SU8 cell cages discussed in this dissertation are present on the substrate. Normally, photoresist is patterned on substrates with features of less than a few microns in height. In this work the photoresist must be patterned on a substrate with 50 μm tall cell cages on it. The photoresist needs to be patterned at the same time on top of the SU8 structure, on the sidewalls, and on the substrate. To my knowledge there is no photoresist designed to meet these requirements, and therefore I used a standard photoresist (Shipley 1813, Rohm and Haas Co.) with a standard aligner (MJB3, Karl Süss) and modified the standard process to obtain acceptable results. I will explain the challenges that I faced using the basic geometry shown in Figure A -1, which consists of a 50 μm tall SU8 structure on an oxidized silicon substrate.

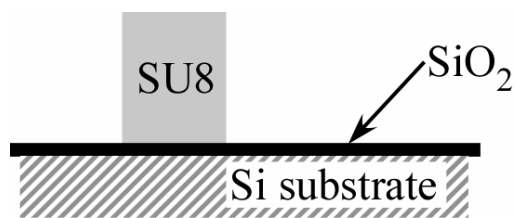


Figure A -1. Side view illustration of the topography on photolithography was done

A.1. Photoresist Deposition

Right before spinning photoresist on a substrate, photoresist is applied directly on it using

a pipette. However, sometimes air bubbles remained trapped inside the SU8 vials, with the consequence that they would ruin the photoresist film by bursting during subsequent baking steps. To solve this problem I used acetone as an intermediate fluid between air and photoresist because acetone wets the vials without leaving air bubbles in it and it also dissolves the photoresist solution. I applied acetone on the substrate prior to the photoresist and I applied photoresist before the acetone evaporated. The photoresist dissolved in the acetone and the vials filled with a mix of the two substances. I applied more photoresist to dilute the acetone out of the mix, because the photoresist spinning curve (the relationship between final film thickness and spinning speed) is affected by the presence of acetone. In the end, virtually all the acetone was replaced by photoresist, and the inside of the vials is fully wet with photoresist. The substrate is ready for spinning.

A.2. Photoresist Spinning

Typically 1813 is spun at 2000 - 3000 rpm for 30 seconds to obtain a fairly uniform 1.8 - 1.4 μm thick film. However, I found that under these conditions the presence of the SU8 structure results in uneven film coverage. Figure A -2 shows an illustration A) and a photo B) of the non-uniformities. The non-uniformities consist of accumulation of photoresist on the top face of the SU8 structure, near the edges (1), discontinuous films on the top and side faces, at the convex edges of the SU8 structure (2), and accumulation of photoresist near the concave corners between the SU8 structure and the substrate (3). Photoresist accumulations take a long time to bake during the soft-baking steps, and if the photoresist is not fully baked it will be dissolved by the developer regardless of exposure.

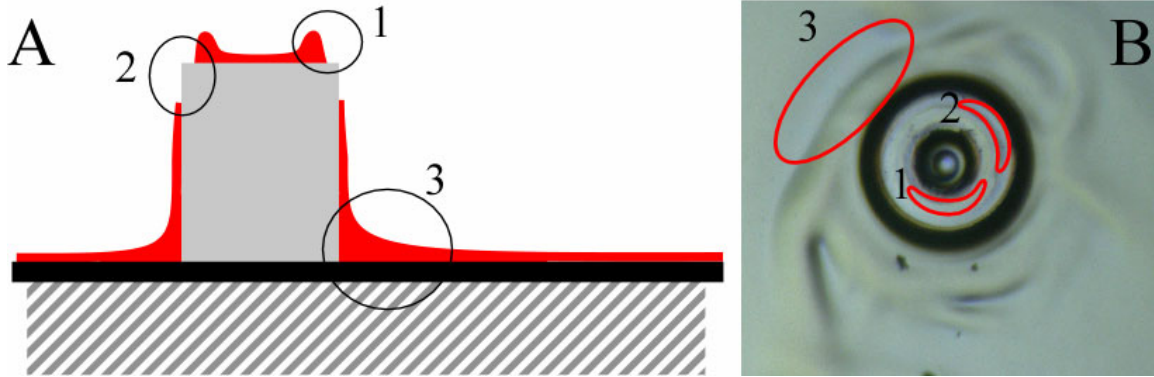


Figure A -2. A) Illustration and B) photography of 1813 film after spinning at 2000 rpm for 30 seconds.

I found that these non-uniformities were ameliorated if the substrate was spun at higher speeds and for longer times. I used the highest spinning speed available in the cleanroom spinner, 5000 rpm, for one minute or longer. The photoresist coating after this procedure is illustrated in Figure A -3. Photoresist accumulations on top of the SU8 structure (1) and on the concave corner of the SU8 and the substrate (2) still remained, but to a lesser extent as before. To bake these accumulations the soft-baking step that follows spinning was extended from 90 seconds to 180 seconds. The baking temperature, 90 °C, did not change from the original process.

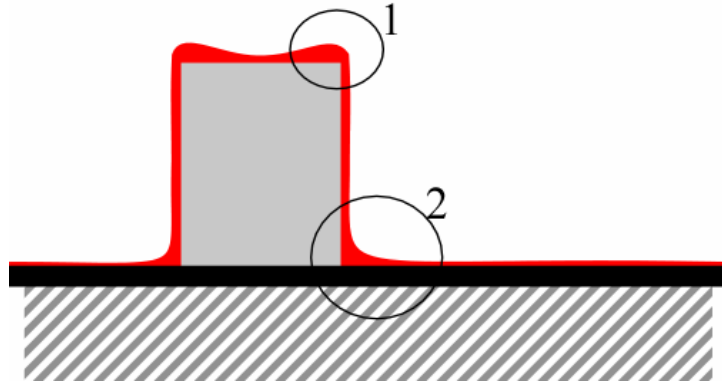


Figure A -3. Photoresist layer after spinning at 5000 rpm for > 1 minute.

A.3. Exposure

Photoresist 1813 films 1.8 - 1.4 μm thick typically need an exposure of 80 mJ/cm^2 of 365 nm light. However, this exposure was not sufficient for the photoresist accumulations and the film on the sidewalls. I found that these regions were properly exposed after roughly 720 mJ/cm^2 of 365 nm light. However, such long exposure degraded the mask pattern transferred on the photoresist because of diffraction. Normally, diffraction causes small amounts of light to leak near the edges of mask features, as illustrated in Figure A -4. Normally, the radiation doses associated with diffraction are not enough as to expose the photoresist much beyond the mask feature edges. However, I need to use ten times the regular exposure dose. In addition, the region affected by diffraction when the vials are present is larger because the mask cannot be brought closer than 50 μm from the substrate, when the mask enters contact with the top of the vial (normally the substrate and the mask are in direct contact). As a result of these factors, illustrated in Figure A -4 the mask pattern is degraded several microns away from every mask feature.

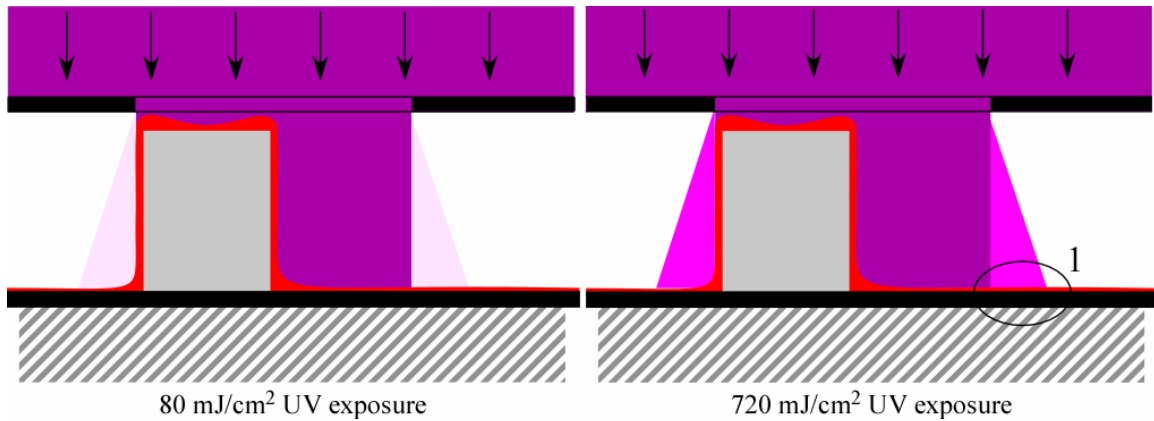


Figure A -4. Exposure of 80 mJ/cm² and 720 mJ/cm². The gap between the mask and the substrate, due to the presence of the SU8 structure, and the increased exposure results in degraded pattern transfer from the mask.

A picture of the resulting pattern is shown in Figure A -5. The dashed line indicates the boundary of the mask used to pattern the photoresist. This figure shows how the photoresist boundary is up to 30 μm beyond where the edge of the mask pattern originally was. The device fabricated, the MFDEP vial traps, could tolerate the poor mask pattern transfer because the features patterned once the SU8 structures were present are large, and they were located far enough from other features so that variations of 30 μm from the mask did not interfere with device function.

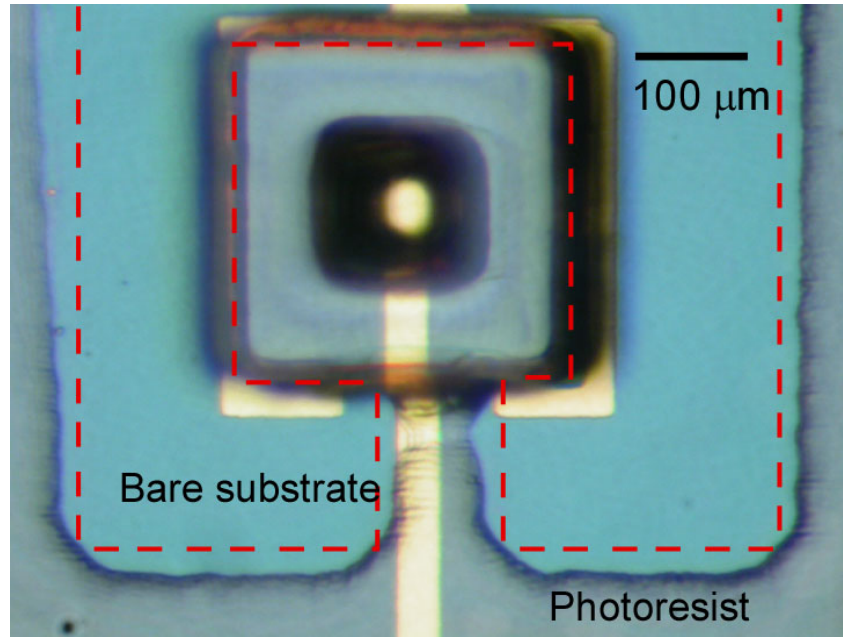


Figure A -5. Photoresist near a 50 μm tall SU8 vial after development.

Appendix B. Cell Clinics Technology Platform for Cell-Based Sensing¹³

B.1. Abstract

The cell clinics microsystem is a platform for long-term cell monitoring for such applications as cell-based sensing. This system includes microvials with individually actuated lids, integrated circuits that monitor cells and control the position of the vial hinges, and an automated cell loading mechanism that relies on dielectrophoresis to manipulate individual cells into the vials.

B.2. Introduction

The cell clinics system is designed to house individual cells or small groups of cells for long-term monitoring and experimentation (Figure B -1) [1], with potential applications ranging from medical diagnosis to detection of biochemical agents. The system uses micro-electro-mechanical systems (MEMS) fabricated over complementary metal oxide semiconductor (CMOS) chips that include sensing, signal conditioning, and MEMS control circuitry. The MEMS comprise cell-sized cavities (vials) that have lids that can be opened and closed using bilayer hinges.

¹³ This chapter was presented as a paper at the *Life Science Systems & Applications Workshop*, Bethesda, Maryland, July 13 – 14, 2006, under the title “Cell clinics technology platform for cell-based sensing”, by M. Urdaneta, M. Christophersen, E. Smela, S. B. Prakash, N. Nelson, and P. Abshire,

Dielectrophoresis shall be used for automated loading of the cells into the vials.

Dielectrophoresis is appropriate in this case because of the high vial density, chip surface inhomogeneities, small size ranges of operation, and the presence of CMOS/MEMS, which limits integration of other methods.

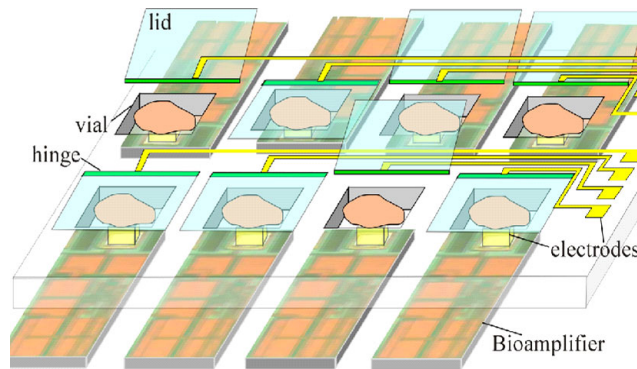


Figure B -1. The cell clinics array microsystem for long term monitoring of cells.

B.3. MEMS PLATFORM: Vials and lids

The purpose of the lidded vials is to keep specific types of cells over specific CMOS sensors, as well as to isolate them physically, chemically, and/or electrically from other cells. The lids and vials are both made from SU8, a biocompatible negative photoresist. The bilayer hinges comprise gold and the electro-active polymer polypyrrole, whose volume is voltage controlled [3]. These actuators can operate in bio-fluids and are fabricated at CMOS-compatible temperatures.

The actuators shown in Figure B -2 were controlled using an external potentiostat. Actuators were also successfully cycled using a CMOS control circuit designed in-house (see below), which will ultimately be integrated into the system.

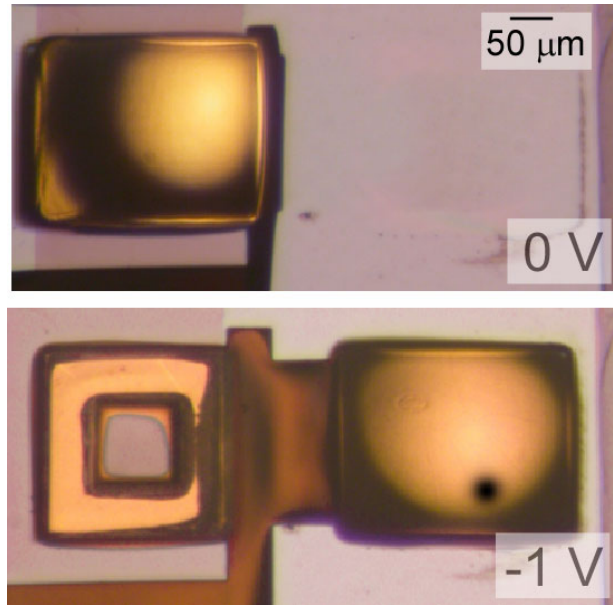


Figure B -2. SU8 microvial with a polypyrrole/gold bilayer hinge on a dummy silicon sample. The hinge is shown in the open ($V = -1$ V vs. Ag/AgCl) and closed ($V = 0$ V) positions.

B.4. CMOS PLATFORM

B.4.1. Bio-amplifier

For the purpose of monitoring the activity of electrically active cells (such as neurons and muscle cells), a bio-amplifier has been designed for amplifying weak extracellular signals. The bioamplifier is a low voltage, low noise CMOS transconductance amplifier, designed for a gain of 100 and a bandwidth of 3 kHz. The circuit has been tested and characterized with live cells cultured on the chip [182]. A bioamplifier test chip for integration with the MEMS structures has been fabricated in a commercially available 0.5 μm CMOS process. A packaged chip is shown in Figure B -3 with MEMS microvials on the surface. The bioamplifier chip comprises an array of amplifier modules connected to

an array of on-chip electrodes for cell sensing and an array of actuation electrodes for actuator control.

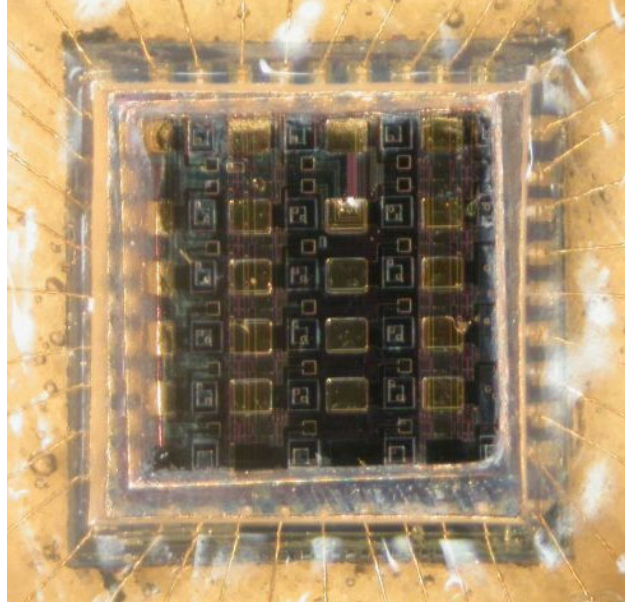


Figure B -3. 24-bioamplifier CMOS chip with MEMS structures. The chip has been packaged as described in [162].

B.4.2. Integrated Potentiostat

A CMOS potentiostat circuit was designed for control of, and integration with, the MEMS actuators [183]. The test chip comprises single-ended amperometric potentiostat modules connected to on-chip working, reference, and counter electrodes. The potentiostat module was successfully bench-tested for cycling off-chip polypyrrole films on a gold-coated silicon substrate. Actuation tests were successfully performed on an array of 416 microactuators with hinge lengths varying from 4 μm to 200 μm .

B.4.3. Cell Loading

Since the cell clinics system comprises an array of vials in which a few cells must be individually loaded, we are pursuing an automated loading device. The device is illustrated in Figure B-4. Dielectrophoretic forces, which act on uncharged particles in non-uniform electrical fields [52], are used to steer the cells over the chip surface and into a vial. Two electrodes are used to accomplish this: the DEP electrode (1), inside the vial, is used to pull the cell in, while electrode (2), outside the vial, is used to keep other cells out of the vial. The upper edge of the vial can give rise to localized parasitic cages. During loading, we observe that particles become trapped at the upper edge of the vial. To solve this issue, we are using numerical models (FEMLAB, Comsol, Inc.) and are varying the electrode configuration and vial geometries.

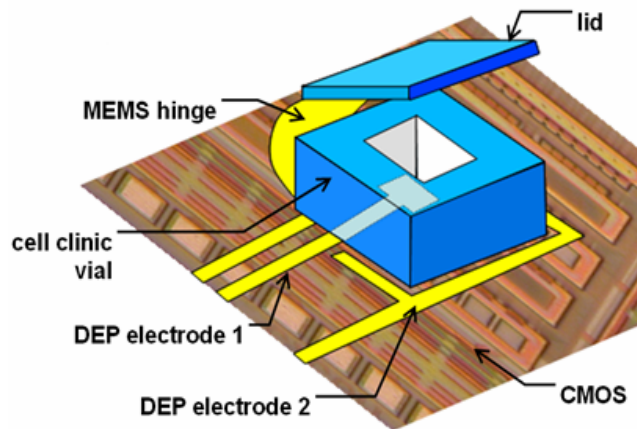


Figure B-4. The dielectrophoretic trap used to load individual cells into the microvials.

B.5. Summary

We present a hybrid CMOS/MEMS microsystem for housing and monitoring cells long-term. The hinged microvials have been tested and integrated with the CMOS chip. The bioamplifier and potentiostat circuits have been successfully tested, and the amplifier has been integrated into the cell clinics chip. Cell loading, which relies on dielectrophoresis, has been tested, and parasitic cage problems are being addressed with the aid of numerical modeling.

Appendix C Flow-Through Sorter Modeling Consideration

C.1. Order of Magnitude Confirmation

The maximum opposing velocity that an electrode pair of configuration A produces can be solved analytically by using the parallel plate fringing fields solution. This solution assumes that the electric fields are not constrained to the channel and that the electrodes are very long so that the two ends of the electrodes do not interact with each other. This velocity is [49]

$$(C1) \quad U_{\max} = \frac{9\pi\epsilon \cdot CM \cdot R^2 \cdot V_{RMS}^2}{64\eta \cdot h^3}$$

If we use U_{DEP} to non-dimensionalize this velocity we obtain

$$(C2) \quad \frac{U_{\max}}{U_{DEP}} = \frac{27\pi}{64} = 1.33$$

which is similar in order of magnitude to U'_{max} found for geometry A ($U'_{max} \sim 1.6$). This confirms that our simulations are consistent with existing theory.

C.2. Sources of Error in the Solution

C.2.1. Brownian Motion

The force on a particle due to Brownian motion is [199]

$$(C3) \quad F_{Brown} = \sqrt{\frac{12\pi R\eta k_b T}{\Delta t}}$$

where k_b is the Boltzmann constant, T is the absolute temperature, and Δt is the magnitude of the time step.

Comparing Brownian motion to fluid velocity is convenient because in this dissertation I have used fluid velocity to describe the dielectrophoretic velocity as well. The Brownian motion-derived force divided by the drag on the same particle produced by fluid moving at a velocity U opposite to the Brownian motion is

$$(C4) \quad \frac{F_{Brown}}{F_{drag}} = \frac{1}{6U(R\eta)^{1/2}} \sqrt{\frac{12\pi k_b T}{t_R}}$$

In the application featured in this dissertation, particles 10 μm in diameter suspended in water at room temperature in a flow moving at 50 $\mu\text{m/s}$. Given these conditions, the forces derived from the Brownian motion of the particle will be comparable to fluid drag forces over time periods of 0.1ms. Over such periods of time the particle is expected to move about 5 nm, which is small (1/1000th) compared to the particle diameter, and it is a distance over which the DEP forces at the location of U_{max} are expected to vary very small amounts, as we will discuss in the next section. Therefore we conclude that Brownian motion is not important in the applications here discussed.

Furthermore, one could look at the motion away from the modeled trajectory due to Brownian motion using Equation (C5) [40].

$$(C5) \quad \delta_B = \sqrt{\frac{k_b T dt}{3\pi\eta R}}$$

Based on the simulations we know that a particle will take between 0.1 and 0.01 seconds

to go from above the vial to the inner electrode. During that time, the yeast cells used in this study will move 30 - 90 nm, which is 10 - 30 times smaller than the cell diameter and 100 - 300 times smaller than the vial. Therefore we may conclude that Brownian motion does not affect the loading of cells.

C.2.2. Spatial Distribution of U'_{max}

Will small motions of the particle at or near the point of U'_{max} affect greatly the fluid velocity that the electrode pair can oppose? Figure C-1A) and B) shows U' along the line of weakest force for a flow-through sorter of geometry A and $w' = 0.1$. In this case, $U'_{max} = 1.6$, and for U' to decrease by 10% the particle needs to move $\Delta x' = 0.052$ in either direction along the x' axis. In a channel 100 μm tall, like those used in this dissertation to illustrate the loading and steering of cells, this distance translates to 5 μm , which is 1000 times the motion expected due to Brownian motion upon the particle. The smallest change in U' that can be measured (after improving the mesh obtained after the 7 automatic refinements) is 0.008, which is 0.5% of U'_{max} , and this change occurs over distances of $\Delta x' = 0.004$. Such distance translates to 400 nm, or nearly 100 times the distance the particle is expected to move due to Brownian motion during a single jump, thus we conclude that force variations due to Brownian motion displacement for the system considered in this dissertation will be negligible.

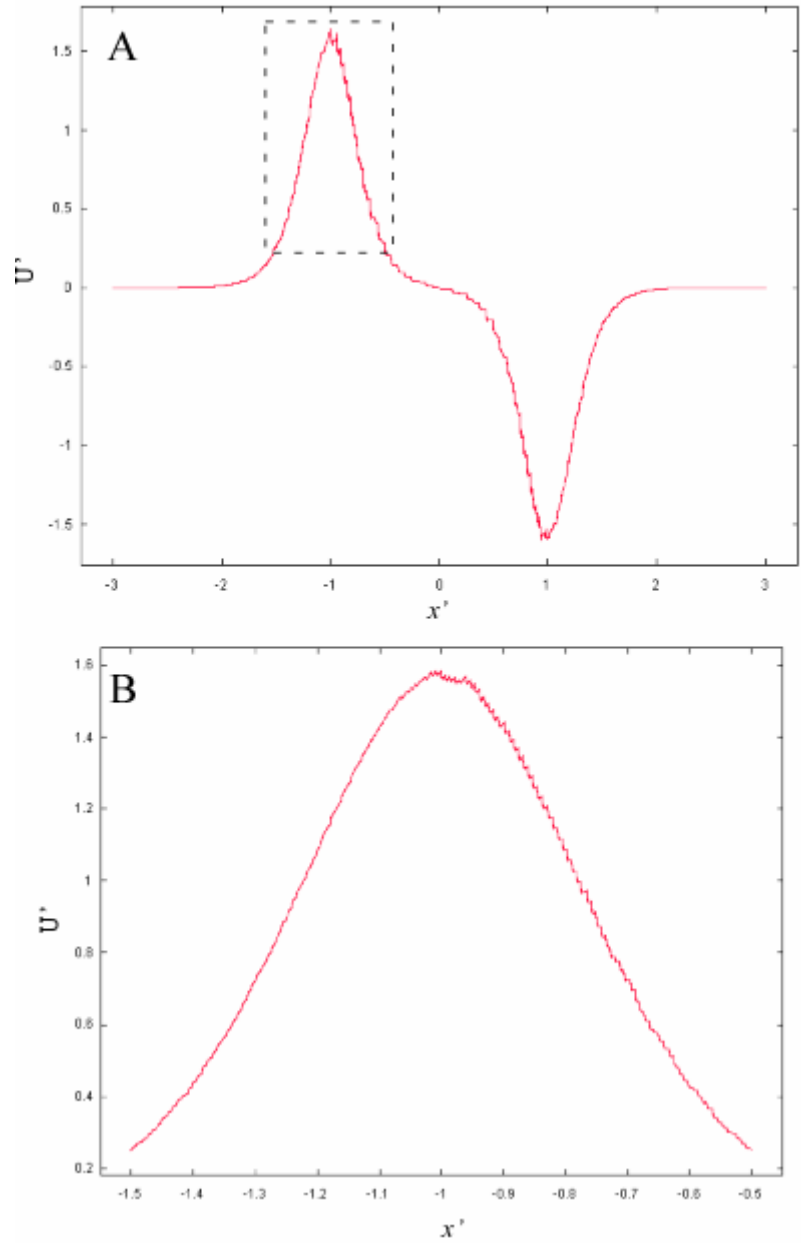


Figure C-1. A) U' as a function of x -position along y' of weakest force. B) Zoom in of the dashed box in (A) (obtained after increased mesh refinement).

C.2.3. Uncertainty of Properties and Parameters

In Chapter 2 the expected uncertainty on U_{max} was based on 5% for every parameter

involved in U_{DEP} . The purpose of this exercise is to illustrate that the curves of U'_{max} vs. w' are meant as a guideline because relatively small uncertainties can distort the value of U_{max} significantly.

The equation that describes the sensitivity on uncertainty to different parameters is [169]

$$(C6) \quad \left(\frac{dU_{DEP}}{U_{DEP}} \right)^2 = \left(\frac{dCM}{CM} \right)^2 + \left(\frac{d\varepsilon}{\varepsilon} \right)^2 + \left(2 \frac{dR}{R} \right)^2 + \left(2 \frac{dV_{RMS}}{V_{RMS}} \right)^2 + \left(\frac{d\eta}{\eta} \right)^2 + \left(3 \frac{dh}{h} \right)^2$$

Perhaps uncertainties more reasonable¹⁴ than 5% for each parameter would be the following. CM (for an insulating particle in a very conductive medium): < 1%, ε : 2%, R :

¹⁴ CM: Assuming that the medium is much more conductive than the fluid, then CM will take the constant value of -0.5 with an uncertainty of \sim (cell membrane conductivity/medium conductivity), which for yeast cells it is typically $\sim 10^{-5}$ [84].

ε : The dielectric constant of water can vary between 72 and 80 at the extremes, depending on the field frequency and concentration of ions in the solution [200]. In more reasonable solutions the permittivity will vary between 74 and 78 [200].

R: Assuming cells 10 μm in diameter and whose diameter is measured using an optical microscope. The uncertainty in such measurements, based on personal experience, is $\pm 1 \mu\text{m}$.

V_{RMS} : Assuming that the voltage is measured using an oscilloscope. Typically oscilloscopes have screen sizes of 10 divisions in the voltage and time axis, and a readout uncertainty of $1/10^{\text{th}}$ of a division. Given a voltage of 8 $V_{\text{peak-to-peak}}$, the readout uncertainty will be 0.04 V, which in turn is $\sim 1\%$ of the RMS value.

η : Due to heating the water in the channel can increase up to 4 $^{\circ}\text{C}$ [134]. Therefore the uncertainty arises from variations between ambient and the actual fluid temperature, which varies greatly with fluid conductivity, field frequency, voltage, fluid velocity, and velocity profile.

10%, V_{RMS} : 1%, η (based on temperature variations of 4 °C): 15% and h : 1%. With these uncertainties, the uncertainty on U_{DEP} will be 18%.

C.3. Numerical Simulation Programs

The programs used in the modeling were written in Matlab 7 and they used Femlab 3.1 as the numerical model engine (Matlab needs to be opened through the "Femlab with Matlab" option in the Femlab start-up program menu). The program builds the geometries, defines the boundary conditions, initializes the mesh, it solves the model and instructs Femlab to refine the mesh 7 times using Femlab's "adaptation method". The program then takes the solution along a predefined y -axis value (which is the height of lowest DEP force) and extracts the highest DEP force in the x -direction. This value is recorded in a matrix, and is at last plotted as a function of electrode width. A typical mesh, after 7 iterations of refinement is shown in Figure C-2.

The Femlab models were done using the Electromagnetics Module, using the quasi-statics (time-harmonic), small in-plane currents mode, which solves Laplace's equation using quadratic Lagrange elements, and solved using the UMFPAK solver. The initial mesh was constructed by Femlab using the "extra coarse" predefined mesh size. The maximum element size was not constrained, the maximum element size scaling factor was 3, and the mesh curvature and curvature cut-off were 0.8 and 0.02 respectively. The

h: The uncertainty is based on the uncertainty of the caliper (Starrett, 120AM 150) used to measure the thickness of the SU8 film that makes up the channel. In our lab the profilometer is limited by a step height of 130 μm , and this limits the height measurement, thus prompting the use of a caliper.

mesh refinements were done automatically by Femlab using the "rough global minimum" element selection method (the L2 error norm had a scaling factor of 1) while increasing the number of elements by 1.7.

The mesh shown in Figure C-2 is typical. In this case, the initial mesh had 24 elements (14 boundary elements, 63 degrees of freedom) and after the 7 refinement iterations the mesh had 14360 elements (396 boundary elements and 29117 degrees of freedom).

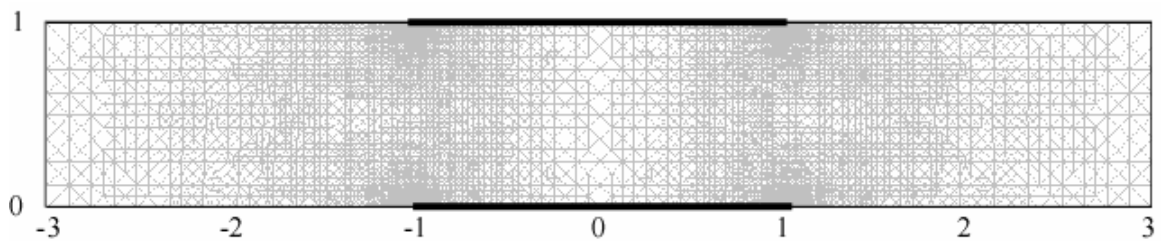


Figure C-2. Typical mesh used to find U'_{max} (this case is for $w' = 1$). The electrodes, on the floor and ceiling of the channel, are illustrated by the black lines.

The normalized average discrepancy between values of U'_{max} (evaluated for $w = 0.02$ to 4 in increments of 0.02) between two subsequent iteration refinements are shown in Figure C-3. This plot suggests that, in average, the error of the solution due to meshing after 7 iterations will be in the order of 2%.

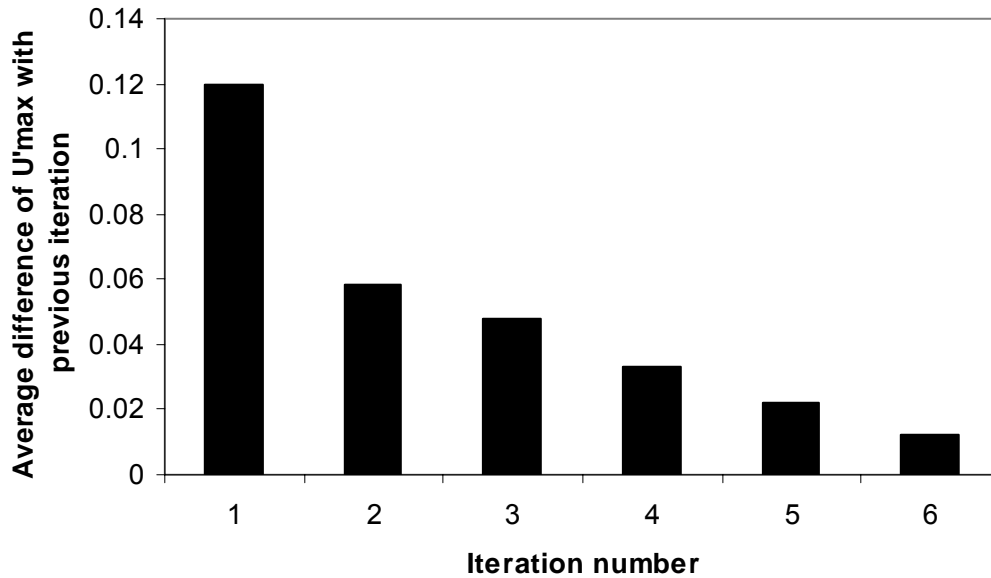


Figure C-3. Average difference between U'_{max} obtained from models with i and $(i+1)$ mesh refinements, where i is the number of refinement iterations ($w' = 0.002 - 4$).

The programs used are given below for each geometry. Each section contains the main program used, followed by the functions called by that program. All of these functions are needed by the program.

C.3.1. Geometry A

Main program

```
clear all

fem = FLstartup;

b=1;

%L = 0.02:1:4;
%L = .1:1:1;
L = .5
n = length(L);
%maxDEP = zeros(n);
for i = 1:n
    fem = FLgeometry_mirror(L(i),b,fem);
    fem=FLextracoarsemesh(fem);
```

```

    fem = FLBCs_mirrorX(fem);
    fem = FLSolve(fem,7);
    [fem,maxDEPx(i)] = FLplotX(fem,[-L(i)/.8,b/2],[L(i)/.8,b/2]);
end
figure(30),plot(10.^maxDEPx,'b'), Uprime_whole = 10.^maxDEPx;

save('mirror_roof_data_extracoarsemeshX.mat','L','Uprime_whole')

```

FLgeometry_mirror

```

function fem = FLgeometry_mirror(a,b,fem)
H = 1; %Domain heigth
L = 5*a + H; %Domain length

% Geometry
g1=rect2(L,H,'base','corner','pos',[-L/2,0]);
carr={curve2([-a,a],[0,0],[1,1])};
g2=geomcoerce('curve',carr);
carr={curve2([-a,a],[H,H],[1,1])};
g3=geomcoerce('curve',carr);
clear c s
c.objs={g2,g3}
c.name={'B1','B2'};
c.tags={'g2','g3'};

s.objs={g1};
s.name={'R1'};
s.tags={'g1'};

fem.draw=struct('s','c',c);
fem.geom=geomcsg(fem);

figure(1),geomplot(fem.geom)
axis equal

```

FLBCs_mirrorX

```

function fem=FLBCs_mirrorX(fem)

% (Default values are not included)

% Application mode 1
clear appl
appl.mode.class = 'QuasiStatics';
appl.module = 'CEM';
appl.assignsuffix = '_qvw';
clear prop
prop.elemdefault='Lag2';
prop.analysis='smallcurr';
appl.prop = prop;
clear bnd
bnd.V0 = {1,0,0};
bnd.eltype = {'V','nJ0','V0'};
bnd.ind = [2,2,2,1,3,2,2,2];
appl.bnd = bnd;

```

```
fem.appl{1} = appl;
fem.border = 1;

% Subdomain expressions
clear equ
equ.ind = [1];
equ.dim = {'V'};
equ.expr = {'DEPx','log10(diff(normE_qvw^2,x))'};
fem.equ = equ;

% Multiphysics
fem=multiphysics(fem);
```

C.3.2. Geometry B

Main program

```
clear all

fem = FLstartup;

b=1;

L = 0.02:0.02:4;
L=0.25
n = length(L);
maxDEPx = zeros(n);
for i = 1:n
    fem = FLgeometry(L(i),fem);
    fem=FLextracoarsemesh(fem);
    fem = FLBCsX(fem);
    fem = FLSolve(fem,7);
    [fem,maxDEPx(i)] = FLplotX_gray(fem,[-L(i)/.8,b],[L(i)/.8,b]);
end
hold on
figure(30),plot(10.^maxDEPx,'k'), Uprime_whole = 10.^maxDEPx;

save('whole_roof_data_extracoarsemeshX.mat','L','Uprime_whole')
```

FLBCsX

```
function fem=FLBCsX(fem)

% (Default values are not included)

% Application mode 1
clear appl
appl.mode.class = 'QuasiStatics';
appl.module = 'CEM';
appl.assignsuffix = '_qvw';
clear prop
prop.elemdefault='Lag2';
prop.analysis='smallcurr';
appl.prop = prop;
clear bnd
```

```

bnd.V0 = {1,0,0};
bnd.etype = {'V','nJ0','V0'};
bnd.ind = [2,2,3,1,2,2];
appl.bnd = bnd;
fem.appl{1} = appl;
fem.border = 1;

% Subdomain expressions
clear equ
equ.ind = [1];
equ.dim = {'V'};
equ.expr = {'DEPx','log10(diff(normE_qvw^2,x))'};
fem.equ = equ;

% Multiphysics
fem=multiphysics(fem);

```

C.3.3. Geometry C

Main program

```

clear all

fem = FLstartup;

b=1;

%L = .02:0.02:4;
L = 1;
n = length(L);
maxDEPx = zeros(n);
for i = 1:n
    fem = FLgeometry(L(i),fem);
    fem=FLextracoarsemesh(fem);
    fem = FLBCs_parallelX(fem);
    fem = FLSolve(fem,7);
    [fem,maxDEPx(i)] = FLplotX_gray(fem,[-L(i)/.8,b],[L(i)/.8,b]);
end
hold on
figure(30),plot(10.^maxDEPx,'k'), Uprime_whole = 10.^maxDEPx;

save('parallel_data_extracoarsemeshX.mat','L','Uprime_whole')

```

FLBCs_parallelX

```

function fem=FLBCsX(fem)

% (Default values are not included)

% Application mode 1
clear appl

```

```

appl.mode.class = 'QuasiStatics';
appl.module = 'CEM';
appl.assignsuffix = '_qvw';
clear prop
prop.elemdefault='Lag2';
prop.analysis='smallcurr';
appl.prop = prop;
clear bnd
bnd.V0 = {1,0,0};
bnd.etype = {'V','nJ0','V0'};
bnd.ind = [2,3,2,2,1,2];
appl.bnd = bnd;
fem.appl{1} = appl;
fem.border = 1;

% Subdomain expressions
clear equ
equ.ind = [1];
equ.dim = {'V'};
equ.expr = {'DEPx','log10(diff(normE_qvw^2,x))'};
fem.equ = equ;

% Multiphysics
fem=multiphysics(fem);

```

C.3.4. Geometry D

Main Program

```

clear all

fem = FLstartup;

b=1;

L = .02:.02:4;
n = length(L);
%maxDEP = zeros(n);
L = 2.*L;%This line is necessary to make L consistent with the other programs. L = 2W
for i = 1:n
    fem = FLgeometry_parallel_large_small(L(i),fem);
    fem=FLextracoarsemesh(fem);
    fem = FLBCs_parallel_large_smallX(fem);
    fem = FLSolve(fem,7);
    [fem,maxDEPx(i)] = FLplotX(fem,[-L(i)/.8,b],[L(i)/.8,b]);
    %[fem,maxDEPx(i)] = FLplotX_gray(fem,[-L(i)/.8,b],[L(i)/.8,b]);
end
figure(20),plot(10.^maxDEPx,'b'), Uprime_whole = 10.^maxDEPx;

save('parallel_large_small_data_finemeshX_.mat','L','Uprime_whole')

```

FLgeometry_parallel_large_small

```

function fem = FLgeometry_parallel_large_small(a,fem)
H = 1; %Domain heighth
L = 5*a + H; %Domain length

% Geometry
g1=rect2(L,H,'base','corner','pos',[-L/2,0]);
parr={point2(-a/2,0)};
g2=geomcoerce('point',parr);
parr={point2(a/2,0)};
g3=geomcoerce('point',parr);
parr={point2(3*a/2,0)};
g4=geomcoerce('point',parr);
clear p s
p.objs={g2,g3,g4};
p.name={'PT1','PT2','PT3'};
p.tags={'g2','g3','g4'};

s.objs={g1};
s.name={'R1'};
s.tags={'g1'};

fem.draw=struct('p',p,'s',s);
fem.geom=geomcsg(fem);

figure(1),geomplot(fem.geom)
axis equal

```

FLBCs_parallel_large_smallX

```

function fem=FLBCs_parallel_large_smallX(fem)

% (Default values are not included)

% Application mode 1
clear appl
appl.mode.class = 'QuasiStatics';
appl.module = 'CEM';
appl.assignsuffix = '_qvw';
clear prop
prop.elemdefault='Lag2';
prop.analysis='smallcurr';
appl.prop = prop;
clear bnd
bnd.V0 = {0,0,1};
bnd.eltype = {'V0','nJ0','V'};
bnd.ind = [2,1,2,2,3,2,2];
appl.bnd = bnd;
fem.appl{1} = appl;
fem.border = 1;

% Subdomain expressions
clear equ
equ.ind = [1];
equ.dim = {'V'};
equ.expr = {'DEPx','log10(diff(normE_qvw^2,x))'};

```

```
fem.equ = equ;

% Multiphysics
fem=multiphysics(fem);
```

C.3.5. Functions Used by All Geometries

FLstartup

```
function fem = FLstartup

fclear fem

% Femlab version
clear vrsn
vrsn.name = 'FEMLAB 3.1';
vrsn.ext = '';
vrsn.major = 0;
vrsn.build = 157;
vrsn.rcs = '$Name: $';
vrsn.date = '$Date: 2004/11/12 07:39:54 $';
fem.version = vrsn;
```

FLextracoarsemesh

```
function fem=FLextracoarsemeshh(fem)

% Initialize mesh
fem.mesh=meshinit(fem, ...
    'hmaxfact',3, ...
    'hgrad',1.8, ...
    'hcurve',0.8, ...
    'hcutoff',0.02);
```

FLsolve

```
function fem=FLsolve(fem,adpatation_itt)

% Extend mesh
fem.xmesh=meshextend(fem);

% Solve problem
fem.sol=femlin(fem,'solcomp',{'V'},'outcomp',{'V'});

% Save current fem structure for restart purposes
fem0=fem;

% Evaluate initial value using current solution
init = assemnit(fem,'u',fem0.sol);

% Solve problem
```

```
fem=adaption(fem, ...
    'init',init, ...
    'solcomp',{'V'}, ...
    'outcomp',{'V'}, ...
    'nonlin','off', ...
    'solver','stationary', ...
    'l2scale',[1], ...
    'l2staborder',[2], ...
    'eigselect',[1], ...
    'maxt',10000000, ...
    'ngen',adpatation_itt, ...
    'resorder',[0], ...
    'rmethod','longest', ...
    'tppar',1.7, ...
    'geomnum',1);
```

FLplotX

```
function [fem,maxDEP] = FLplot(fem,X1,X2)
```

```
% Plot solution
figure(2), postplot(fem, ...
    'tridata',{'DEPx','cont','internal'}, ...
    'trimap','jet(20)', ...
    'title','Surface: DEP forces', ...
    'refine',3, ...
    'axis',[-1.8468085106383,1.8468085106383,-1.00851063829787,1.0,-1,1]);
```

```
%Make cross-section plot:
figure(3), h=postcrossplot(fem,1,[X1(1) X2(1);X1(2) X2(2)],'lindata','DEPx','npoints',100);
```

```
%This will plot from the point (0 0) to (0 0)
```

```
% Create p,t,d and call meshintegrate:
d=get(h,'YData');
maxDEP = max(d)
```

FLgeometry

```
function [fem,maxDEP] = FLplot(fem,X1,X2)
```

```
% Plot solution
figure(2), postplot(fem, ...
    'tridata',{'DEP','cont','internal'}, ...
    'trimap','jet(20)', ...
    'title','Surface: DEP forces', ...
    'refine',3, ...
    'axis',[-1.8468085106383,1.8468085106383,-1.00851063829787,1.0,-1,1]);
```

```
%Make cross-section plot:
figure(3), h=postcrossplot(fem,1,[X1(1) X2(1);X1(2) X2(2)],'lindata','DEP','npoints',100);
```

```
%This will plot from the point (0 0) to (0 0)
```

```
% Create p,t,d and call meshintegrate:
```

```
d=get(h,'YData');  
maxDEP = max(d)
```

References

- [1] Reeves, N., *et al.*, "Integrated MEMS structures and CMOS circuits for bioelectronic interface with single cells", in *IEEE Intl. Symp. Cir. Sys. (ISCAS)*, Vancouver, Canada, 3, p.673 - 676, 2004.
- [2] Abshire, P., J.-M. Lauenstein, Y. Liu, and E. Smela, "Cell clinics for bioelectronic interface with single cells", in *IEEE Intl. Symp. Cir. Sys. (ISCAS)*, Bangkok, Thailand, 2003.
- [3] Urdaneta, M., *et al.*, "Integrating conjugated polymer microactuators with CMOS sensing circuitry for studying living cells", in *Smart Structures and Materials: Electroactive Polymer Actuators and Devices (EAPAD)*, San Diego, California, 5759, p.232, 2005.
- [4] Prasad, S., *et al.*, "Neurons as sensors: individual and cascaded chemical sensing", *Biosens. Bioelectron.*, 19, p.1599-1610, 2004.
- [5] Ho, C., *et al.*, "Rapid heterogeneous liver-cell on-chip patterning via the enhanced field-induced dielectrophoresis trap", *Lab Chip*, 6, p.724-734, 2006.
- [6] Alp, B., G.M. Stephens, and G.H. Markx, "Formation of artificial, structured microbial consortia (ASMC) by dielectrophoresis", *Enzyme Microb. Technol.*, 31, p.35-43, 2002.
- [7] Yu, Z., *et al.*, "Negative dielectrophoretic force assisted construction of ordered neuronal networks on cell positioning bioelectronic chips", *Biomed. Microdevices*, 6 (4), p.311-324, 2004.
- [8] Castellarnau, M., *et al.*, "Integrated cell positioning and cell-based ISFET biosensors", *Sensors Actuat. B-Chem.*, 120 (2), p.615-620, 2007.
- [9] Tooker, A., *et al.*, "Biocompatible parylene neurocages", *IEEE Eng. Med. Biol.*, 24 (6), p.30-33, 2005.
- [10] Zeck, G., and P. Fromherz, "Noninvasive neuroelectronic interfacing with synaptically connected snail neurons immobilized on a semiconductor chip", *P. Nat'l Acad. Sci. USA*, 98 (18), p.10457-10462, 2001.
- [11] Merz, M., and P. Fromherz, "Polyester microstructures for topographical control of outgrowth and synapse formation of snail neurons", *Adv. Mater.*, 14 (2), p.141-144, 2002.
- [12] Tooker, A., *et al.*, "Parylene neurocages for electrical stimulation on silicon and glass substrates", in *IEEE EMBS Annu. Intl. Conf.*, New York, USA, p.4322 -

- 4325, 2006.
- [13] Ionescu-Zanetti, C., *et al.*, "Mammalian electrophysiology on a microfluidic platform", *P. Nat'l Acad. Sci. USA*, 102 (26), p.9112-9117, 2005.
 - [14] Lidstrom, M.E., and D.R. Meldrum, "Life-on-a-chip", *Nature Reviews Microbiology*, 1 (2), p.158-164, 2003.
 - [15] Weigl, B.H., R.L. Bardell, and C.R. Cabrera, "Lab-on-a-chip for drug development", *Adv. Drug Delivery Rev.*, 55 (3), p.349-377, 2003.
 - [16] van den Berg, A., and P. Berveld, "Labs-on-a-chip: origin, highlights, and future perspectives", *Lab Chip*, 6, p.1266-1273, 2006.
 - [17] Gomez-Sjoberg, R., D.T. Morissette, and R. Bashir, "Impedance microbiology-on-a-chip: Microfluidic bioprocessor for rapid detection of bacterial metabolism", *J. Microelectromech. S.*, 14 (4), p.829-838, 2005.
 - [18] Jager, E.W.H., O. Inganäs, and I. Lundstrom, "Microrobots for micrometer-size objects in aqueous media: Potential tools for single-cell manipulation", *Science*, 288 (5475), p.2335-2338, 2000.
 - [19] El-Ali, J., P. Sorger, and K.F. Jensen, "Cells on chip", *Nature*, 442 (27), p.403-411, 2006.
 - [20] Johann, R.M., "Cell trapping in microfluidic chips", *Anal. Bioanal. Chem.*, 385, p.408-412, 2006.
 - [21] Lodish, H., *et al.*, *Molecular Cell Biology*. 4th ed. 2001, New York: W. H. Freeman and Co.
 - [22] Lambacher, A., *et al.*, "Electrical imaging of neuronal activity by multi-transistor-array (MTA) recording at 7.8 μm resolution", *Appl. Phys. A-Mater.*, 79 (7), p.1607-1611, 2004.
 - [23] Vassanelli, S., and P. Fromherz, "Neurons from rat brain coupled to transistors", *Appl. Phys. A-Mater.*, 65, p.85-88, 1997.
 - [24] DeBusschre, B.D., and G.T.A. Kovacs, "Portable cell-based biosensor system using integrated CMOS cell-cartridges", *Biosens. Bioelectron.*, 16, p.543-556, 2001.
 - [25] Prakash, S.B., and P. Abshire, "On-chip capacitance sensing for cell monitoring applications", *IEEE Sens. J.*, 7 (3-4), p.440-447, 2007.
 - [26] Strong, T.D., S.M. Martin, R.F. Franklin, and R.B. Brown, "Integrated electrochemical neurosensors", in *IEEE Intl. Symp. on Circuits and Systems*

- (ISCAS), p.4110 - 4113, 2006.
- [27] Heer, F., *et al.*, "Fully integrated 128-electrode CMOS chip for bidirectional interaction with electrogenic cells", in *Proc. Eurosensors XIX*, Barcelona, Spain, 2, 2005.
 - [28] Futai, N., G. Wei, J. Song, and S. Takayama, "Handheld recirculation system and customized media for microfluidic cell culture", *Lab Chip*, 6, p.149 - 154, 2006.
 - [29] Folch, A., and M. Toner, "Microengineering of cellular interactions", *Annu. Rev. Biomed. Eng.*, 2, p.227-256, 2000.
 - [30] Chronis, N., and L. Lee, "Electrothermally activated SU8 microgripper for single cell manipulation in solution", *J. Microelectromech. S.*, 14 (4), p.857 - 863, 2005.
 - [31] Roch, I., P. Bidaud, D. Collard, and L. Buchaillot, "Fabrication and characterization of an SU8 gripper actuated by a shape memory alloy thin film", *J. Micromech. Microeng.*, 13 (2), p.330-336, 2003.
 - [32] Klemic, K.G., J.F. Klemic, M.A. Reed, and F.J. Sigworth, "Micromolded PDMS planar electrode allows patch clamp electrical recordings from cells", *Biosens. Bioelectron.*, 17 (6-7), p.597-604, 2002.
 - [33] Klemic, K.G., J.F. Klemic, and F.J. Sigworth, "An air-molding technique for fabricating PDMS planar patch-clamp electrodes", *Pflugers Archiv.*, 449 (6), p.564-572, 2005.
 - [34] Lehnert, T., M.A.M. Gijs, R. Netzer, and U. Bischoff, "Realization of hollow SiO₂ micronozzles for electrical measurements on living cells", *Appl. Phys. Lett.*, 81 (26), p.5063-5065, 2002.
 - [35] Fertig, N., *et al.*, "Activity of single ion channel proteins detected with a planar microstructure", *Appl. Phys. Lett.*, 81 (25), p.4865-4867, 2002.
 - [36] Fertig, N., R.H. Blick, and J.C. Behrends, "Whole cell patch clamp recording performed on a planar glass chip", *Biophys. J.*, 82 (6), p.3056-3062, 2002.
 - [37] Lau, A.Y., P.J. Hung, A.R. Wu, and L.P. Lee, "Open-access microfluidic patch-clamp array with raised lateral cell trapping sites", *Lab Chip*, 6 (12), p.1510-1515, 2006.
 - [38] Han, A., *et al.*, "A single cell multi-analysis system for electrophysiological studies", in *Intl. Conf. on Solid State Sensors, Actuators, and Microsystems (TRANSDUCERS)*, Boston, USA, p.674-677, 2003.
 - [39] Maher, M.P., J. Pine, J. Wright, and Y.-C. Tai, "The neurochip: a new multielectrode device for stimulating and recording from cultured neurons", *J.*

- Neuroscience Methods, 87, p.45 - 56, 1999.
- [40] Armani, M.D., S.V. Chaudhary, R. Probst, and B. Shapiro, "Using feedback control of microflows to independently steer multiple particles", J. Microelectromech. S., 15 (4), p.945-956, 2006.
- [41] Jones, T., Electromechanics of Particles. 1995, New York: Cambridge University Press.
- [42] Folch, A., *et al.*, "Microfabricated elastomeric stencils for micropatterning cell cultures", J. Biomed. Mater. Res., 52 (2), p.346-353, 2000.
- [43] Folch, A., *et al.*, "Molding of deep polydimethylsiloxane microstructures for microfluidics and biological applications", J. Biomech. Eng., 121 (1), p.28-34, 1999.
- [44] Hodgkin, A.L., and A.F. Huxley, "Resting and action potentials in single nerve fibres", Journal of Physiology-London, 104 (2), p.176-195, 1945.
- [45] Wong, P.K., U. Ulmanella, and C.M. Ho, "Fabrication process of microsurgical tools for single-cell trapping and intracytoplasmic injection", J. Microelectromech. S., 13 (6), p.940-946, 2004.
- [46] Ashkin, A., "Optical trapping and manipulation of neutral particles using lasers", Proc. Nat. Acad. Sci. USA, 94 (10), p.4853-4860, 1997.
- [47] Poole, C., W. Losert, D. English, and K. Okamoto, "Probing local and large scale membrane stiffness of giant unilamellar vesicles with holographic laser tweezers", Biophys. J., 88 (1), p.414A, 2005.
- [48] Park, J., *et al.*, "Design and fabrication of an integrated cell processor for single embryo cell manipulation", Lab Chip, 5, p.91-96, 2005.
- [49] Durr, M., *et al.*, "Microdevices for manipulation and accumulation of micro- and nanoparticles by dielectrophoresis." Electrophoresis, 24 (4), p.722-731, 2003.
- [50] Jackson, J.D., Classical Electrodynamics. 2nd ed. Classical electrodynamics. 1975, New York: John Wiley & Sons.
- [51] Pohl, H., "Some effects of nonuniform fields on dielectrics", J. Appl. Phys., 29 (8), p.1182-1188, 1958.
- [52] Pohl, H.A., Dielectrophoresis. 1978, Cambridge: Cambridge University Press.
- [53] Turku, I., and C.M. Lucaciu, "Dielectrophoresis: a spherical shell model", Journal of Physics A: Mathematical and General, 22, p.985-993, 1989.
- [54] Tenopir, C., and D.W. King, "Trends in scientific scholarly journal publishing in

- the United States", *J. Scholarly Publ.*, 28 (3), p.135-170, 1997.
- [55] Pohl, H., and I. Hawk, "Separation of living and dead cells by dielectrophoresis", *Science*, 152, p.647-649, 1966.
- [56] Crane, J.S., and H. Pohl, "A study of living and dead yeast cells using dielectrophoresis", *Journal of Electrochemical Society*, 118 (8), 1967.
- [57] Pohl, H.A., and J.S. Crane, "Dielectrophoresis of cells", *Biophys. J.*, 11 (9), p.711-727, 1971.
- [58] Crane, J.S., and H.A. Pohl, "A study of living and dead yeast cells using dielectrophoresis", *J. Electrochem. Soc.*, 115 (6), p.584-586, 1968.
- [59] Crane, J.S., and H.A. Pohl, "Theoretical models of cellular dielectrophoresis", *Journal of Theoretical Biology*, 37 (1), p.15-41, 1972.
- [60] Benguigui, L., and I.J. Lin, "Experimental analysis of dielectrophoretic forces", *J. Appl. Phys.*, 49 (4), p.2536-2539, 1977.
- [61] Jones, T.B., and G.W. Bliss, "Bubble dielectrophoresis", *J. Appl. Phys.*, 48 (4), p.1412-1417, 1977.
- [62] Molinari, G., and A. Viviani, "Analytical evaluation of the electro-dielectrophoretic forces acting on spherical impurity particles in dielectric fluids", *J. Electrostat.*, 5, p.343-354, 1978.
- [63] Jones, T.B., and G.A. Kallio, "Dielectrophoretic levitation of spheres and shells", *J. Electrostat.*, 6, p.207 - 224, 1979.
- [64] Bahaj, A.S., and A.G. Bailey, "Dielectrophoresis of microscopic particles", *J. Phys. D- App. Phys.*, 12, p.L109-112, 1979.
- [65] Benguigui, L., and I.J. Lin, "More about the dielectrophoretic force", *J. Appl. Phys.*, 53 (2), p.1141-1143, 1982.
- [66] Benguigui, L., and I.J. Lin, "Dielectrophoretic filtration of nonconductive liquids", *Sep. Sci. Technol.*, 17 (8), p.1003-1017, 1982.
- [67] Batchelder, J.S., "Dielectrophoretic manipulator", *Review of Scientific Instruments*, 54 (3), p.300-302, 1983.
- [68] Benguigui, L., and I.J. Lin, "A two-regime approach to the dielectrophoretic effect", *J. Phys. D- App. Phys.*, 17, p.L9 -L12, 1984.
- [69] Benguigui, L., and I.J. Lin, "The dielectrophoresis force", *American Journal of Physics*, 54 (5), p.447-450, 1986.

- [70] Arnold, W.M., H.P. Schwan, and U. Zimmermann, "Surface conductance and other properties of latex particles measured by electrorotation", *Journal of Physical Chemistry*, 91, p.5093-5098, 1987.
- [71] Hughes, M.P., "Strategies for dielectrophoretic separation in laboratory-on-a-chip systems", *Electrophoresis*, 23 (16), p.2569-2582, 2002.
- [72] Schnelle, T., *et al.*, "Paired microelectrode system: dielectrophoretic particle sorting and force calibration", *J. Electrostat.*, 47, p.121-132, 1999.
- [73] Schnelle, T., *et al.*, "3-dimensional electric-field traps for manipulation of cells - calculation and experimental-verification", *Biochimica Et Biophysica Acta*, 1157 (2), p.127-140, 1993.
- [74] Fiedler, S., S.G. Shirley, T. Schnelle, and G. Fuhr, "Dielectrophoretic sorting of particles and cells in a microsystem", *Anal. Chem.*, 70, p.1909-1915, 1998.
- [75] Suehiro, J., and R. Pethig, "The dielectrophoretic movement and positioning of a biological cell using a three-dimensional grid electrode system", *J. Phys. D: Appl. Phys.*, 31, p.3298-3305, 1998.
- [76] Gascoyne, P., *et al.*, "Dielectrophoretic detection of changes in erythrocyte membranes following malarial infection", *Biochim. Biophys. Acta, Biomembr.*, 1323, p.240-252, 1997.
- [77] Fernandez-Morales, F., *et al.*, "Design and simulation of a dielectric-based microsystem for bioparticle handling", in *1st Annu. Intl. IEEE-EMBS Special Topic Conference on Microtechnologies in Medicine & Biology*, Lyon, France, p.429-433, 2000.
- [78] Wang, X.-B., J. Vykoukal, F.F. Becker, and P.R.C. Gascoyne, "Separation of polystyrene microbeads using dielectrophoretic/gravitational field-flow-fractionation", *Biophys. J.*, 74, p.2689-2701, 1998.
- [79] Matsue, T., N. Matsumoto, S. Koike, and I. Uchida, "Microring-ring electrode for manipulation of a single cell", *Biochim Biophys Acta.*, 1157 (3), p.332 - 335, 1993.
- [80] Cheng, J., *et al.*, "Isolation of cultured cervical carcinoma cells mixed with peripheral blood cells on a bioelectronic chip", *Anal. Chem.*, 70 (11), p.2321-2326, 1998.
- [81] Talary, M.S., J.P.H. Burt, J.A. Tame, and R. Pethig, "Electromanipulation and separation of cells using traveling wave dielectrophoresis", *J. Phys. D: Appl. Phys.*, 29, p.2198-2203, 1996.
- [82] Huang, Y., and R. Pethig, "Electrode design for negative dielectrophoresis",

- Meas. Sci. Technol., 2, p.1142-1146, 1991.
- [83] Huang, Y., *et al.*, "Separation of simulants of biological warfare agents from blood by a miniaturized dielectrophoresis device", *Biomed. Microdevices*, 5 (3), p.217-225, 2003.
- [84] Huang, Y., R. Hölzel, R. Pethig, and X.-B. Wang, "Difference in the AC Electrodynamics of Viable and Non-Viable Yeast Cells Determined through Combined Dielectrophoresis and Electrotation Studies", *Phys. Med. Biol.*, 37 (7), p.1499-1517, 1992.
- [85] Hughes, M.P., R. Pethig, and X.-B. Wang, "Dielectrophoretic forces on particles in traveling electric fields", *J. Phys. D: Appl. Phys.*, 29, p.474 - 482, 1996.
- [86] Kaler, K., and R. Paul, "Bioparticle mechatronics", in *Electrical and Computer Engineering, 1996. Canadian Conference on*, Calgary, Alta., Canada, 1, p.100-103, 1996.
- [87] Green, N.G., and H. Morgan, "Dielectrophoresis of submicrometer latex spheres. 1. Experimental results", *J. Phys. Chem. B*, 103, p.41 - 50, 1999.
- [88] Paul, R., and K. Kaler, "Theory of electrode polarization in dielectrophoresis and electrorotation", *J. Colloid. Interf. Sci.*, 194, p.225 - 238, 1997.
- [89] Yang, J., *et al.*, "Dielectric properties of human leukocyte subpopulations determined by electrorotation as a cell separation criterion", *Biophys. J.*, 76, p.3307 - 3314, 1999.
- [90] Gimsa, J., P. Marszalek, U. Loewe, and T. Tsong, "Dielectrophoresis and electrorotation of neurospora slime and murine myeloma cells", *Biophys. J.*, 60, p.749 - 760, 1991.
- [91] Hughes, M.P., and H. Morgan, "Measurement of bacterial flagellar thrust by negative dielectrophoresis", *Biotechnol. Progr.*, 15 (2), p.245-249, 1999.
- [92] Wang, X.-B., *et al.*, "Changes in Friend murine erythroleukaemia cell membranes during induced differentiation determined by electrorotation", *Biochimica and Biophysica Acta*, 1193, p.330-344, 1994.
- [93] Kakutani, T., S. Shibatani, and M. Sugai, "Electrorotation of non-spherical cells: theory for ellipsoidal cells with an arbitrary number of shells. *Bioelectrochem. Bioenerg.* 31:131-145", *Bioelectrochemistry and Bioenergetics*, 31, p.131 - 145, 1993.
- [94] Becker, F.F., *et al.*, "The removal of human leukemia cells from blood using interdigitated microelectrodes", *J. Phys. D: Appl. Phys.*, 27, p.2659-2662, 1994.

- [95] Becker, F.F., *et al.*, "Separation of human breast cancer cells from blood by differential dielectric affinity", *Proc. Nat. Acad. Sci.*, 92, p.860-864, 1995.
- [96] Hagedorn, R., G. Fuhr, T. Muller, and J. Gimsa, "Traveling-wave dielectrophoresis of microparticles", *Electrophoresis*, 13, p.49-54, 1992.
- [97] Wang, X.-B., L. Huang, P. Gascoyne, and F.F. Becker, "Dielectrophoretic manipulation of particles", *IEEE T. Ind. Appl.*, 33 (3), p.660-669, 1997.
- [98] Huang, Y., X.B. Wang, J.A. Tame, and R. Pethig, "Electrokinetic behavior of colloidal particles in traveling electric-fields - studies using yeast cells", *J. Phys. D- App. Phys.*, 26 (9), p.1528-1535, 1993.
- [99] Andres, U., "Dielectric separation of minerals", *J. Electrostat.*, 37, p.227-248, 1996.
- [100] Hölzel, R., "Electric-field calculation for electrorotation electrodes", *J. Phys. D- App. Phys.*, 26 (12), p.2112-2116, 1993.
- [101] Kaler, K., J. Xie, T.B. Jones, and R. Paul, "Dual-frequency dielectrophoretic levitation of canola protoplasts", *Biophys. J.*, 63 (1), p.58-69, 1992.
- [102] Wang, X.-B., Y. Hunang, F. Becker, and P. Gascoyne, "A unified theory of dielectrophoresis and traveling wave dielectrophoresis", *J. Phys. D: Appl. Phys.*, 27, p.1571-1574, 1994.
- [103] Sihvola, A., "Dielectric polarizability of a sphere with arbitrary anisotropy", *Optical Letters*, 19 (7), p.430-432, 1994.
- [104] Wang, X.-B., *et al.*, "Selective dielectrophoretic confinement of bioparticles in potential energy wells", *J. Phys. D: Appl. Phys.*, 26, p.1278-1285, 1993.
- [105] Green, N.G., A. Ramos, and H. Morgan, "AC electrokinetics: a survey of sub-micrometre particle dynamics", *J. Phys. D: Appl. Phys.*, 33, p.632 - 641, 2000.
- [106] Pethig, R., and G.H. Markx, "Applications of dielectrophoresis in biotechnology", *Trends in Biotechnology*, 15 (10), p.426-432, 1997.
- [107] Ramos, A., H. Morgan, N.G. Green, and A. Castellanos, "The role of electrohydrodynamic forces in the dielectrophoretic manipulation and separation of particles", *J. Electrostat.*, 47 (1-2), p.71-81, 1999.
- [108] Pethig, R., "Dielectrophoresis: Using inhomogeneous AC electrical fields to separate and manipulate cells", *Crit. Rev. Biotechnol.*, 16 (4), p.331-348, 1996.
- [109] Holmes, D., H. Morgan, and N.G. Green, "High throughput particle analysis: Combining dielectrophoretic particle focusing with confocal optical detection",

- Biosens. Bioelectron., 21 (8), p.1621-1630, 2006.
- [110] Hu, X., *et al.*, "Marker-specific sorting of rare cells using dielectrophoresis", P. Nat'l Acad. Sci. USA, 102 (44), p.15757-15761, 2005.
- [111] Gascoyne, P.R.C., and J. Vykoukal, "Dielectrophoresis-based sample handling in general-purpose programmable diagnostic instruments", Proceedings of the IEEE, 92 (1), p.22 - 42, 2004.
- [112] Li, H., and R. Bashir, "Dielectrophoretic separation and manipulation of live and heat-treated cells of *Listeria* on microfabricated devices with integrated electrodes", Sens. Actuators, B, 86, p.215-221, 2002.
- [113] Manaresi, N., *et al.*, "A CMOS chip for individual cell manipulation and detection", IEEE J. Solid-St. Cir., 38 (12), p.2297-2305, 2003.
- [114] Cen, E.G., *et al.*, "A combined dielectrophoresis, traveling wave dielectrophoresis and electrorotation microchip for the manipulation and characterization of human malignant cells", J. Microbiol. Meth., 58 (3), p.387-401, 2004.
- [115] Medoro, G., *et al.*, "A lab-on-a-chip for cell detection and manipulation", IEEE Sens. J., 3 (3), p.317-325, 2003.
- [116] Borgatti, M., *et al.*, "Separation of white blood cells from erythrocytes on a dielectrophoresis (DEP) based 'Lab-on-a-chip' device", Int. J. Mol. Med., 15 (6), p.913-920, 2005.
- [117] Grom, F., *et al.*, "Accumulation and trapping of hepatitis A virus particles by electrohydrodynamic flow and dielectrophoresis", Electrophoresis, 27, p.1386 - 1393, 2006.
- [118] Minerick, A.R., R.H. Zhou, P. Takhistov, and H.C. Chang, "Manipulation and characterization of red blood cells with alternating current fields in microdevices", Electrophoresis, 24 (21), p.3703-3717, 2003.
- [119] Hong, S.H., *et al.*, "Fabrication of single electron transistors with molecular tunnel barriers using ac dielectrophoresis technique", Journal of Vacuum Science & Technology B, 24 (1), p.136-138, 2006.
- [120] Bakewell, D.J., and H. Morgan, "Dielectrophoresis of DNA: Time- and frequency-dependent collections on microelectrodes", IEEE T. Nanobiosci., 5 (1), p.1-8, 2006.
- [121] Holmes, D., N.G. Green, and H. Morgan, "Microdevices for dielectrophoretic flow-through cell separation", IEEE Eng. Med. Biol., (November/December), p.85-90, 2003.

- [122] Chiou, P.Y., A.T. Ohta, and M.C. Wu, "Massively parallel manipulation of single cells and microparticles using optical images", *Nature*, 436 (7049), p.370-372, 2005.
- [123] Hölzel, R., *et al.*, "Trapping single molecules by dielectrophoresis", *Phys. Rev. Lett.*, 95 (12), 2005.
- [124] Chen, D.F., H. Du, and W.H. Li, "A 3D paired microelectrode array for accumulation and separation of microparticles", *J. Micromech. Microeng.*, 16 (7), p.1162 – 1169, 2006.
- [125] Flores-Rodriguez, N., and G.H. Markx, "Flow-through devices for the AC electrokinetic construction of microstructured materials", *J. Micromech. Microeng.*, 16 (2), p.349-355, 2006.
- [126] Evoy, S., *et al.*, "Dielectrophoretic assembly and integration of nanowire devices with functional CMOS operating circuitry", *Microelectron, Eng.*, 75, p.31-42, 2004.
- [127] Bakewell, D., *et al.*, "Dielectric relaxation measurements of 12 kbp plasmid DNA", *Biochimica and Biophysica Acta*, 1493, p.151-158, 2000.
- [128] Asbury, C.L., A.H. Diercks, and G. van den Engh, "Trapping of DNA by dielectrophoresis", *Electrophoresis*, 23 (16), p.2658-2666, 2002.
- [129] Asokan, S.B., *et al.*, "Two-dimensional manipulation and orientation of actin-myosin systems with dielectrophoresis", *Nano Letters*, 3 (4), p.431 - 437, 2003.
- [130] Hunt, T.P., and R.M. Westervelt, "Dielectrophoresis tweezers for single cell manipulation", *Biomed. Microdevices*, 8 (3), p.227-230, 2006.
- [131] Docoslis, A., and P. Alexandridis, "One-, two-, and three-dimensional organization of colloidal particles using nonuniform alternating current electric fields", *Electrophoresis*, 23 (14), p.2174-2183, 2002.
- [132] Albrecht, D.R., *et al.*, "Probing the role of multicellular organization in three-dimensional microenvironments", *Nature Methods*, 3 (5), p.369-375, 2006.
- [133] Chen, D.F., H. Du, W.H. Li, and C. Shu, "Numerical modeling of dielectrophoresis using a meshless approach", *J. Micromech. Microeng.*, 15 (5), p.1040 - 1048, 2005.
- [134] Nieuwenhuis, J.H., A. Jachimowicz, P. Svasek, and M.J. Vellekoop, "Optimization of microfluidic particle sorters based on dielectrophoresis", *IEEE Sens. J.*, 5 (5), p.810 - 816, 2005.
- [135] Nieuwenhuis, J.H., and M.J. Vellekoop, "Simulation study of dielectrophoretic

- particle sorters", *Sens. Actuators, B*, 103, p.331-338, 2004.
- [136] Voldman, J., M. Toner, M.L. Gray, and M.A. Schmidt, "Design and analysis of extruded quadrupolar dielectrophoretic traps", *J. Electrostat.*, 57 (1), p.69-90, 2003.
- [137] Li, H., Y. Zheng, D. Akin, and R. Bashir, "Characterization and modeling of a microfluidic dielectrophoresis filter for biological species", *J. Microelectromech. S.*, 14 (1), p.103-112, 2005.
- [138] Cummings, E.B., and A.K. Singh, "Dielectrophoresis in microchips containing arrays of insulating posts: theoretical and experimental results", *Anal. Chem.*, 75, p.4724 - 4731, 2003.
- [139] Markarian, N., M. Yeskel, B. Khusid, and K. Farmer, "Limitations on the scale of an electrode array for trapping particles in microfluidics by positive dielectrophoresis", *Appl. Phys. Lett.*, 82 (26), p.4839-4841, 2003.
- [140] Chang, D.E., S. Loire, and I. Mezic, "Closed-form solutions in the electrical field analysis for dielectrophoretic and traveling wave inter-digitated electrode arrays", *J. Phys. D- App. Phys.*, 36 (23), p.3073-3078, 2003.
- [141] Albrecht, D., R. Sah, and S. Bhatia, "Geometric and material determinants of patterning efficiency by dielectrophoresis", *Biophys. J.*, 87, p.2131-2147, 2004.
- [142] Liang, E., R. Smith, and D. Clague, "Dielectrophoretic manipulation of finite sized species and the importance of the quadrupolar contribution", *Phys. Rev. E*, 70 (6), p.066617 1-8, 2004.
- [143] Morgan, H., *et al.*, "The dielectrophoretic and traveling wave forces generated by interdigitated electrode arrays: analytical solution using Fourier series", *Appl. Phys. D.*, 34, p.1553 - 1561, 2001.
- [144] Chou, C.-F., and F. Zenhausern, "Electrodeless dielectrophoresis for micro total analysis systems", *IEEE Eng. Med. Biol.*, 22 (6), p.62-67, 1998.
- [145] Aldaeus, F., Y. Lin, J. Rooeraade, and G. Amberg, "Superpositioned dielectrophoresis for enhanced trapping efficiency", *Electrophoresis*, 26, p.4252 - 4259, 2005.
- [146] Urdaneta, M., and E. Smela, "Multiple frequency dielectrophoresis", *Electrophoresis*, 18, 2007.
- [147] Gascoyne, P., *et al.*, "Microsample preparation by dielectrophoresis: isolation of malaria", *Lab Chip*, 2 (2), p.70-75, 2002.
- [148] Cheng, J., *et al.*, "Preparation and hybridization analysis of DNA/RNA from E-

- coli on microfabricated bioelectronic chips", *Nature Biotechnology*, 16 (6), p.541-546, 1998.
- [149] Schulte, T.H., R.L. Bardell, and B.H. Weigl, "Microfluidic technologies in clinical diagnostics", *Clinica Chimica Acta*, 321 (1-2), p.1-10, 2002.
- [150] Gascoyne, P.R.C., J. Noshari, F.F. Becker, and R. Pethig, "Use of dielectrophoretic collection spectra for characterizing differences between normal and cancerous cells", *IEEE T. Ind. Appl.*, 30 (4), p.829-834, 1994.
- [151] Suehiro, J., *et al.*, "Dielectrophoretic fabrication and characterization of a ZnO nanowire-based UV photosensor", *Nanotech.*, 17, p.2567-2573, 2006.
- [152] Li, Y., *et al.*, "Continuous dielectrophoretic cell separation microfluidic device", *Lab Chip*, 7, p.239 - 248, 2007.
- [153] Arnold, W.M., "Monitoring of biological cell collection by dielectric spectroscopy", in *Conference on Electrical Insulation and Dielectric Phenomena*, p.40- 44, 2001.
- [154] Chang, D.E., S. Loire, and I. Mezie, "Separation of bioparticles using the traveling wave dielectrophoresis with multiple particles", in *Conf. on Decision and Control*, Maui, USAi, p.6448 - 6453, 2003.
- [155] Zhang, Y.T., F. Bottausci, N.C. MacDonald, and I. Mezic, "Experimental study of two-frequency dielectrophoresis effects on a linear electrode array", in *IEEE Int. Conf. Engineering in Medicine and Biology Society*, 2005.
- [156] Hunt, T.P., H. Lee, and R.M. Westervelt, "Addressable micropost array for the dielectrophoretic manipulation of particles in fluid", *Appl. Phys. Lett.*, 85 (26), p.6421-6423, 2004.
- [157] Chiou, P.Y., W. Wong, J.C. Liao, and M.C. Wu, "Cell addressing and trapping using novel optoelectronic tweezers", in *Micro Electro Mechanical Systems, 2004. 17th IEEE International Conference on*, Maastricht, The Netherlands, p.21-24, 2004.
- [158] Lorenz, H., *et al.*, "SU8: a low-cost negative resist for MEMS", *J. Micromech. Microeng.*, 7 (3), p.121-124, 1997.
- [159] Kovacs, G., *Micromachined Transducers Sourcebook*. 1998, Boston: McGraw-Hill.
- [160] Grula, M., M. Watson, and H. Pohl, "Relationship between dough-raising activity of baker's yeast and the fraction of 'vital' cells as determined by methylene blue staining or by dielectrophoresis", *J. Bio. Phys.*, 13 (1), p.29-32, 1985.

- [161] Liu, Y., *et al.*, "Fabrication of folding microstructures actuated by polypyrrole/gold bilayer", in *Transducers '03: The 12th International Conference on Solid State Sensors, Actuators and Microsystems*, Boston, MA, USA, 1, p.786-789, 2003.
- [162] Delille, R., M. Urdaneta, S. Moseley, and E. Smela, "Benchtop polymer MEMS", *J. Microelectromech. S.*, 15 (5), p.1108-1120, 2006.
- [163] Nieuwenhuis, J.H., A. Jachimowicz, P. Svasek, and M.J. Vellekoop, "High-speed integrated particle sorters based on dielectrophoresis", in *IEEE Sens. J.*, Vienna, Austria, 1, p.64-67, 2004.
- [164] Wakenman, R., and G. Butt, "An investigation of high gradient dielectrophoretic filtration", *Chem. Eng. Res. Des.*, 81 (A8), p.924-935, 2003.
- [165] Demierre, N., *et al.*, "Characterization and optimization of liquid electrodes for lateral dielectrophoresis", *Lab Chip*, 7 (3), p.355-365, 2007.
- [166] Kentsch, J., *et al.*, "Microdevices for separation, accumulation, and analysis of biological micro- and nanoparticles." *IEE Proc. Nanobiotechnol.*, 150 (2), p.82-9, 2003.
- [167] Fox, R., A. McDonald, and P. Pritchard, *Introduction to Fluid Mechanics*. 2003: Wiley. 800.
- [168] Romano, G., L. Sacconi, M. Capitanio, and F.S. Pavone, "Force and torque measurements using magnetic micro beads for single molecule biophysics", *Opt. Commun.*, 215, p.323-331, 2002.
- [169] Figliola, R.S., and D.E. Beasley, *Theory and Design for Mechanical Measurements*. 3rd ed. 2000, New York: John Wiley & Sons, Inc.
- [170] Idelchik, I.E., *Handbook of Hydraulic Resistance*. 3rd ed. 1994, Redding: Begell House Publishers.
- [171] Pethig, R., *Dielectric and electronic properties of biological materials*. 1979, Chichester: John Wiley & Sons.
- [172] Morgan, H., and N.G. Green, *AC Electrokinetic: Colloids and Nanoparticles*. 2002, Baldock: Research Studies Press, LTD.
- [173] Goater, A.D., and R. Pethig, "Electrorotation and dielectrophoresis", *Parasitology*, 117, p.S177-S189, 1998.
- [174] Pethig, R., M.S. Talary, and R.S. Lee, "Enhancing traveling-wave dielectrophoresis with signal superposition", *IEEE Eng. Med. Biol.*, 22 (6), p.43-50, 2003.

- [175] Urdaneta, M., and E. Smela, "Design of dielectrophoretic flow-through sorters using a figure of merit", *J. Micromech. Microeng.*, (submitted), 2007.
- [176] Lapizco-Encinas, B.H., B.A. Simmons, E.B. Cummings, and Y. Fintschenko, "Dielectrophoretic concentration and separation of live and dead bacteria in an array of insulators", *Anal. Chem.*, 76 (6), p.1571-1579, 2004.
- [177] Claverol-Tinture, E., J. Cabestany, and X. Rosell, "Multisite recording of extracellular potentials produced by microchannel-confined neurons in-vitro", *IEEE Transactions on Biomedical Engineering*, 54 (2), p.331-335, 2007.
- [178] Le Pioufle, B., M. Frenea, and A. Tixier, "Parallel cell biochips: cell placement using dielectrophoresis or microfluidic effects", *Comptes Rendus Physique*, 5 (5), p.589-596, 2004.
- [179] Christophersen, M., *et al.*, "Integrated cell-based sensors and "Cell Clinics" utilizing conjugated polymer actuators", in *SPIE 14th Int'l. Symp. Smart Struct. Mater., Electroactive Polymer Actuators and Devices (EAPAD)*, San Diego, USA, 6524, p.65240G, 2007.
- [180] Prakash, S.B., M. Urdaneta, E. Smela, and P. Abshire, "A CMOS capacitance sensor for cell adhesion characterization", in *IEEE International Symposium on Circuits and Systems*, Kobe, Japan, 2005.
- [181] Ji, H., M. Urdaneta, E. Smela, and P. Abshire, "CMOS contact imager for monitoring cultured cells", in *IEEE International Symposium on Circuits and Systems*, Kobe, Japan, 2005.
- [182] Prakash, S., N. Nelson, M. Urdaneta, and E. Smela, "Biolabs-on-a-chip: monitoring cells using CMOS biosensors", in *IEEE/NLM Life Science System & Applications Workshop*, Bethesda, Maryland, 2006.
- [183] Prakash, S.B., *et al.*, "A CMOS potentiostat for control of integrated MEMS actuators", in *IEEE International Symposium on Circuits and Systems (ISCAS)*, Kos, Greece, 2006.
- [184] Prakash, S., *et al.*, "In situ electrochemical control of electroactive polymers on a CMOS chip", *Sensors and Actuators A*, (submitted), 2007.
- [185] Ostrovidov, S., J. Jiang, Y. Sakai, and T. Fujii, "Membrane-based PDMS microbioreactor for perfused 3D primary rat hepatocyte cultures", *Biomed. Microdevices*, 6 (4), p.279-287, 2004.
- [186] Yang, S.Y., *et al.*, "A cell counting/sorting system incorporated with a microfabricated flow cytometer chip", *Meas. Sci. Technol.*, 17 (7), p.2001-2009, 2006.

- [187] Yang, A.S., and W.H. Hsieh, "Hydrodynamic focusing investigation in a micro-flow cytometer", *Biomedical Microdevices*, 9 (2), p.113-122, 2007.
- [188] Greenberg, M.D., *Advanced Engineering Mathematics*. 2nd. ed. 1998, Upper Saddle River: Prentice Hall.
- [189] Anderson, J.R., *et al.*, "Fabrication of topologically complex three-dimensional microfluidic systems in PDMS by rapid prototyping", *Anal. Chem.*, 72 (14), p.3158-3164, 2000.
- [190] Chang, W.J., *et al.*, "Poly(dimethylsiloxane) (PDMS) and silicon hybrid biochip for bacterial culture", *Biomed. Microdevices*, 5 (4), p.281-290, 2003.
- [191] Harmon, M.E., M. Tang, and C.W. Frank, "A microfluidic actuator based on thermoresponsive hydrogels", *Polymer*, 44 (16), p.4547-4556, 2003.
- [192] Jo, B.-H., L.M. Van Lerberghe, K.M. Motsegood, and D.J. Beebe, "Three-dimensional micro-channel fabrication in polydimethylsiloxane (PDMS) elastomer", *J. Microelectromech. S.*, 9 (1), p.76-81, 2000.
- [193] McDonald, J.C., S.J. Metallo, and G.M. Whitesides, "Fabrication of a configurable, single-use microfluidic device", *Anal. Chem.*, 73 (23), p.5645-5650, 2001.
- [194] McDonald, J.C., and G.M. Whitesides, "Poly(dimethylsiloxane) as a material for fabricating microfluidic devices", *Accounts of Chemical Research*, 35 (7), p.491-499, 2002.
- [195] Ng, J.M.K., I. Gitlin, A.D. Stroock, and G.M. Whitesides, "Components for integrated poly(dimethylsiloxane) microfluidic systems", *Electrophoresis*, 23 (20), p.3461-3473, 2002.
- [196] Heida, T., P. Vulto, W.L.C. Rutten, and E. Marani, "Viability of dielectrophoretically trapped neural cortical cells in culture", *Journal of Neuroscience Methods*, 110 (1-2), p.37-44, 2001.
- [197] Liu, Y., "Fabrication and Characterization of Polypyrrole/Gold Bilayer Microactuators for Bio-MEMS Applications", in *Department of Mechanical Engineering*. 2005, University of Maryland: College Park.
- [198] Streetman, B., and S. Banerjee, *Solid State Electronic Devices. Solid state physical electronics*, ed. N. Holonyak. 2000, Delhi: Pearson Education.
- [199] Kim, M., and A. Zydney, "Effect of electrostatic, hydrodynamic, and Brownian forces on particle trajectories and sieving in normal flow filtration", *Journal of Colloid and Interface*

Science, 269, p.425-431, 2004.

- [200] Little, V.I., "The dielectric constant of aqueous ionic solutions", Proceedings of the Physical Society of London, 68 (6), p.357 - 365, 1955.